NTNU – Trondheim
Norwegian University of
Science and Technology

Phase Transformation Study of X70 Steel by EBSD during In Situ Heating and Quenching

Kristoffer Werner Hansen

Materials Science and Engineering
Submission date: June 2012
Supervisor: Jarle Hjelen, IMTE
Co-supervisor: Morten Karlsen, Statoil

Norwegian University of Science and Technology
Department of Materials Science and Engineering

Preface

This master thesis was done at the Institute of Material Science and Engineering at the Norwegian University of Science and Technology, NTNU, during the spring of 2012. Parts of the results will be presented on the 22nd ISOPE Conference 2012, which takes place at Rhodes, Greece.

I wish to thank my supervisors Prof. Jarle Hjelen and Prof. II Morten Karlsen for general guidance in the EBSD-technique and for tips in the use of the analyzing software. Further, I would like to thank Prof. II Odd Magne Akselsen and PhD candidate Amin Azar for providing of the material and for sharing knowledge about the API X70 steel. I would also like to thank department engineer Tor Arild Nilsen for technical advising and for ensuring access to the experimental high vacuum chamber and department engineer Harald Holm for support in the field of electronics. Morten Raanes has been helpful with EPMA analysis and senior engineer Wilhelm Dall has provided vital technical guidance concerning SEM and EBSD throughout the semester. A thank you goes to Solveig Kirknes at SINTEF Materials and Chemistry for the help with thermal weld simulation.

Finally, I will thank my fellow student Truls Gruben Sætran for the close cooperation regarding the development of the quenching device, and for extensive discussions throughout this master thesis.

Trondheim, June 14th 2012

Kristoffer W. Hansen

Abstract

Arctic steels, like the API X70 steel explored in this master thesis, are developed to withstand very low temperatures, with a ductile/brittle transition temperature below $-60°C$. However, during welding, brittle phases like martensite-austenite (M-A) islands may form in the heat affected zone (HAZ). In this master thesis in situ heat treatment and quenching experiments have been combined with electron backscatter diffraction (EBSD) inside a field emission scanning electron microscope in order to simulate a second weld cycle simulation. In conjunction with this a quenching device has been designed with respect to an existing hot stage.

Inside the SEM, it was found difficult to recreate the characteristic microstructure of API X70 steel from a traditional second cycle thermal weld simulation. This was probably due to the slow heating rate and the excessive high temperature holding time. The developed quenching device was based on gas quenching and produced a steel sample cooling time from 600°C to 400°C, $\Delta t_{6/4}$, of approximately 6.5 seconds in every experiment. As a result of the gas quenching substantial amounts of oxide contamination, covered the sample surface following the experiments. This contamination layer produced artifacts, such as unreasonable amounts of austenite in the EBSD phase maps.

Despite the quenching, islands of austenite (FCC) observed at elevated temperatures transformed into a low strain BCC structure. Some austenite islands showed a memory-effect during phase transformation, while others adapted the orientation of the surrounding structure. No retained austenite was observed in the API X70 steel after the in situ gas quenching, probably due to insufficient cooling rates.

Sammendrag

Arktiske stål, som API X70-stålet undersøkt i denne oppgaven, er utviklet til å tåle lave temperaturer, med en sprø til duktil overgangstemperatur lavere enn -60°C. Problemer oppstår ved sveising hvor sprø M-A-faser dannes i den varmepåvirkede sonen (HAZ). I denne masteroppgaven kombineres in situ varmebehandling og bråkjøling med diffraksjon av tilbakespredte elektroner (EBSD) inne i et feltemisjon skanning elektronmikroskop (FESEM). På bakgrunn av dette har en bråkjølingsenhet blitt utviklet og tilpasset en eksisterende varmestage for SEM.

Det viste seg svært vanskelig å gjenskape mikrosturen til det to-sykel sveisesimulerte X70-stålet inne i elektronsmikroskopet, trolig på grunn av den lave oppvarmingshastigheten og den lange holdetiden ved høy temperatur. Den utviklede bråkjølingsenheten baserte seg på gasskjøling og oppnådde en reproduserbar avkjølingstid fra 600° til 400°, $\Delta t_{6/4}$, på circa 6,5 sekunder. Gasskjølingen resulterte i et kontaminasjonsbelegg som dekket store deler av prøveoverflaten. Kontaminasjonsbelegget forstyrret EBSD-analysen og ga urimelige store mengder austenitt i fasekartene. Den krystallografiske orienteringen ble også påvirket av kontaminasjonsbelegget.

Dannelse av austenitt (FCC) ble observert ved høy temperatur, men på tross av bråkjølingen ble austenitten transformert til en BCC-struktur med lave spenninger. Enkelte austenittøyer fikk en krystallografisk orientering lik den opprinnelige etter endt faseomvandling, og viste dermed en minneeffekt. Andre austenittøyer tilpasset seg nabokornenes struktur. På grunn av utilstrekkelig avkjølingshastighet ble det ikke oppservert restaustenitt etter in situ oppvarmings- og bråkjølingseksperimentene.

Abbreviations and Symbols

Abbreviations	Explanation
α-phase	Ferrite
γ-phase	Austenite
Ac_1	Austenite start temperature during heating
Ac_3	Austenite finish temperature during heating
AF	Acicular ferrite
API	American Petroleum Institute
BCC	Body Centered Cubic atomic structure
CCD camera	Charge-Couple Device camera
CCT diagram	Continuous Cooling Transformation diagram
CI	Confidence Index
$\Delta t_{8/5}$	Cooling time between 800 and 500°C
$\Delta t_{6/4}$	Cooling time between 600 and 400°C
EBSD	Electron BackScatter Diffraction
EPMA	Electron Probe Micro-Analyzer
FCC	Face Centered Cubic atomic structure
HAZ	Heat Affected Zone

Abbreviations	Explanation
HSLA	High Strength, Low Alloy
H/Q	Heating and Quenching
K-S	Kurdjumov-Sachs
IC CG HAZ	InterCritical Coarse Grained HAZ
IPF	Inverse Pole Figure
IQ	Image Quality
ISOPE	International Society of Offshore and Polar Engineers
MA-phase	A mixture of brittle martensite and residual austenite
M_f	Martensite finish temperature during cooling
M_s	Martensite start temperature during cooling
PC	Pattern Centre
RT	Room Temperature
SEM	Scanning Electron Microscopy
TWS	Thermal Weld Simulation
WD	Working Distance

Contents

Chapter 1

Introduction

Due to the world's increasing energy demand the oil & gas companies are expanding their area of interest into new and unexplored regions. The findings of oil and gas deposits in the arctic region have created an interest of developing production sites in these extremely weather exposed areas. United States Geological Survey (USGS) estimates that approximately 30% of the remaining gas reserves and 13% of the remaining oil reserves may be located north of the polar circle [1]. The construction design in these areas has to be robust in order to ensure a long lifetime without needing excessive maintenance during production.

The rough climate in the arctic regions sets new requirements to the materials. Arctic steels, like the API X70 steel explored in this master thesis, are developed to withstand very low temperatures, with a ductile/brittle transition temperature below -60°C. However, during welding, brittle phases like martensite-austenite (M-A) islands may form in the heat affected zone (HAZ) [2, 3, 4, 5, 6], resulting in a lower strength and toughness, especially at low temperatures. Increased knowledge of how these phases form, and their influence on the arctic steels during low temperature exposure, is of great importance.

The objective for this master thesis is to understand the changes in the steel microstructure during welding. This will be done by combining in situ heat treatment and quenching experiments inside a field emission scanning electron microscope (FESEM) with the use of electron backscattered diffraction (EBSD) in order to simulate a second weld cycle operation. By combining the EBSD measurements with the in situ experiments, characteristics of the M-A phases can be studied.

During this master thesis a quenching device has been designed with respect to an existing in situ heating stage. Problems related to temperature measurements in high vacuum and contamination due to gas quenching has been investigated. The resulting steel microstructure after an in situ heating and quenching experiment has been compared to the microstructure of a 2 cycle weld simulated steel sample by the use of light microscope and EBSD.

Finally several in situ heating and quenching experiments have been performed and analyzed with the EBSD-technique.

Chapter 2

Theory

This chapter will deal with the basic theory of High Strength Low Alloy steel (HSLA), with additional emphasis on the arctic API X70 steel, and the potential problems due to welding of the metal. Theory related to the heat transfer during sample quenching in vacuum will be included. Finally, the EBSD technique will be explained.

2.1 HSLA-steel (arctic steel)

High Strength Low Alloy (HSLA) steels were developed during the 60's and 70's in order to cope with the problems related to the welding of conventional construction steels and the accidents with brittle fractures at low temperature exppsure. [7]

HSLA-steels get their strength and toughness through carefully designed thermo-mechanical processes that gives a very fine grained microstructure. The transition temperature, the temperature at which the fracture mechanics of the steel changes from ductile to brittle, is a function of the content of silicon, nitrogen and perlite, in addition to be dependent on the ferrite grain size. The relationship is described by equation 2.1 bellow. A small grain size L promotes a low transition temperature. [8]

$$T_0(^\circ C) = -19 + 44(wt\%Si) + 700\sqrt{(\%N_f)} + 2.2(perlite) - 11.5\frac{1}{\sqrt{L}} \tag{2.1}$$

In order to get recrystallization and a finer austenite grain structure, the steel is hot rolled multiple times at different temperatures in the austenite area of the phase diagram (figure 2.1). Ferrite then nucleates on the austenite grain boarders, resulting in an even finer grain structure. If the steel is rolled in the area just above the A_3 temperature, deformation bands form inside the austenite grains, and the ferrite gets even more available nucleation sites. The result is a very fine grained microstructure, often referred to as acicular ferrite (AF), providing very good mechanical properties at low temperatures. [8, 9, 10]

The phase diagram for Fe-C in figure 2.1 gives the temperatures where the different phase transformations occur in equilibrium, at given carbon contents. The equilibrium

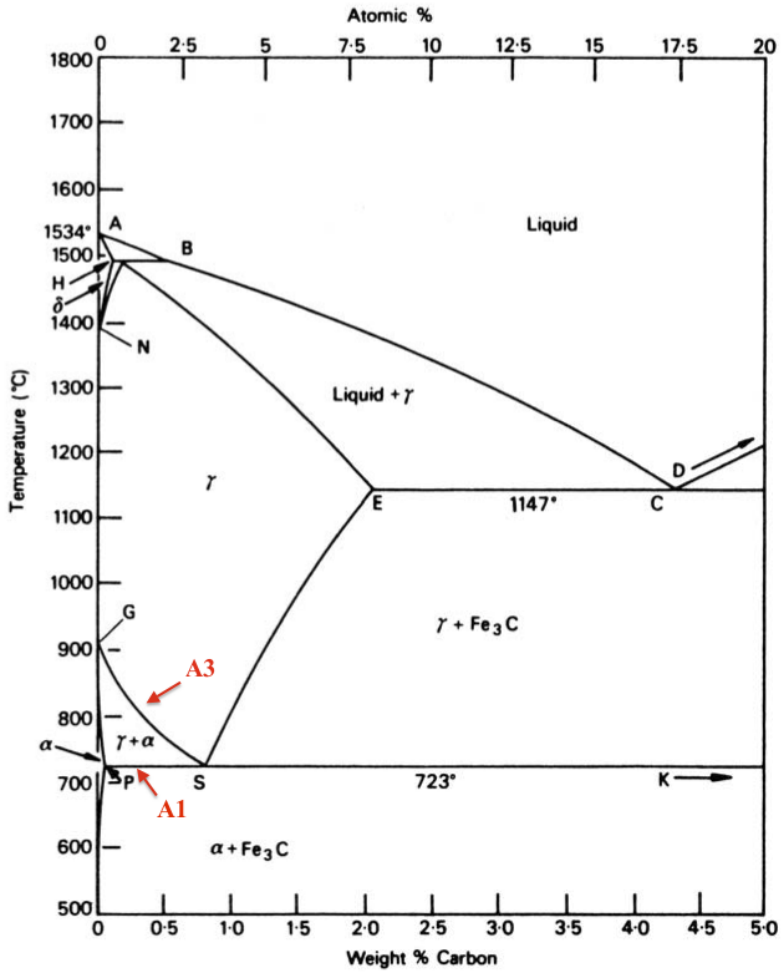

Figure 2.1: The Fe-C phase diagram. [11]

transformations between α and γ phase occur at the A_1 and A_3 temperatures. Due to kinetics the phase transformation temperatures differ during heating of the steel. The transformation temperatures are now called Ac_1 and Ac_3 and can be found experimentally from a dilatometer curve. A dilatometer is an instrument that can measure the volumetric expansion during a thermal process and is therefore often combined with thermal weld simulation tests. The steel has a fairly constant expansion coefficient and will change its volume with a constant rate during a constant heating. However, a change in the slope will imply the beginning of the phase transformation from ferrite (BCC, α) to austenite (FCC, γ), referred to as the Ac_1-temperature. A new change in the slope will occur when the steel reaches the Ac_3-temperature and the transformation from α to γ has completed.

Ac_1 and Ac_3 can also be calculated theoretically from equation 2.2 and 2.3, respectively. [12]

$$\begin{aligned} Ac_1 = 723 \quad & -10.7(wt\%Mn) - 16.9(wt\%Ni) + 29.1(wt\%Si) \\ & +16.9(wt\%Cr) + 290(wt\%As) + 6.38(wt\%W) \end{aligned} \tag{2.2}$$

$$\begin{aligned} Ac_3 = 910 \quad & -203(wt\%C)^{1/2} - 15.2(wt\%Ni) + 44.7(wt\%Si) \\ & +104(wt\%V) + 31.5(wt\%Mo) + 13.1(wt\%W) \end{aligned} \tag{2.3}$$

However, the transformation temperatures, especially the Ac_3, are highly dependent on the temperature gradients during heating. A high heating rate will result in a higher transformation temperature compared to that of a slower heating. The Ac_1 is somewhat less affected by the heating rate [12].

2.1.1 Microstructure of API X70 steel

According to J. Wang and A. Atrens [13] the the base microstructure of API X70 was found to consist mainly of ferrite but with "some perlite and some small precipitates inside the ferrite grains". Grain boundary carbides occurred on ferrite-ferrite grain boundaries and at triple points.

2.2 Welding and weld simulation

During welding, the steel is heated locally to temperatures above the melting point in order to metallurgically join two parts together. The weld pool will have a resulting microstructure dependent on the weld metal composition, often a combination of intragranular nucleated acicular ferrite, bainite and Widmanstatten ferrite. However, the final mechanical properties of the welded part are also dependent on the changes in the microstructure of the base metal due to the heating. The microstructure of HSLA-steels is, as mentioned earlier, a result of a carefully designed thermo-mechanical process in order to achieve the fine-grained structure. The reheating of the metal during welding results in a undesirable change in the microstructure, introducing coarse grains and brittle phases. A cross section of the heat affected zone (HAZ) is shown in figure 2.2a and indicates the most common classifications, including Coarse Grain, Fine Grain, Intercritical (partially transformed) and Subcritical HAZ. The different zones are a result of varying peak temperatures with increasing distance from the weld centre. [5]

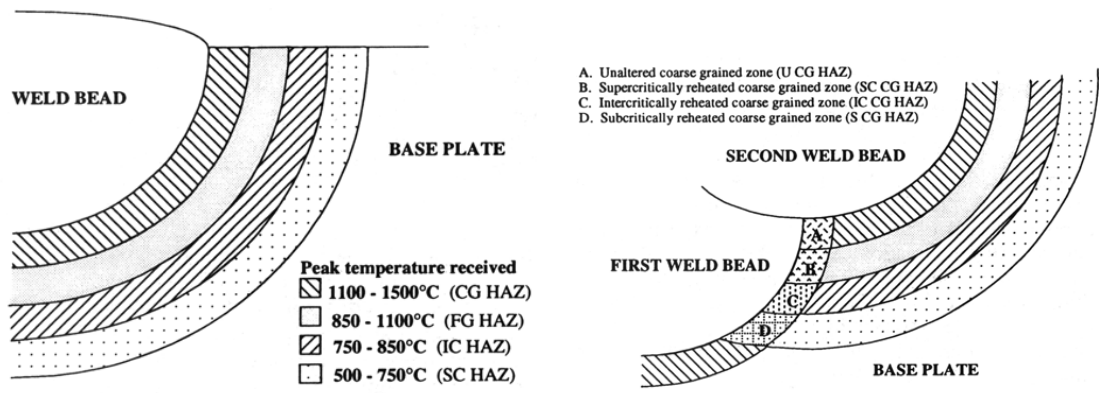

(a) Single-pass weld HAZ

(b) Multipass weld HAZ

Figure 2.2: Schematic drawing of (a) a single-pass weld HAZ, and (b) a multipass weld HAZ. [5]

In multipass welding the same metal is reheated several times. The original coarse grained zone is divided into sub-zones where, according to C. L. Davis and J. E. King [5], the intercritically reheated coarse grained zone (IC CG HAZ) is the one with the lowest toughness (figure 2.2b).

This toughness reduction is a result of the MA-phase, the martensite/austenite-phase, which often forms during reheating and subsequent cooling of the HAZ [2, 3, 4, 5, 6]. When the coarse grained microstructure is reheated to the two-phase region of the phase diagram, islands of austenite are formed at grain boundaries and near previous austenite boundaries. The formed austenite has a high alloy content, which reduces both the martensite start (M_s) and finish (M_f) temperature, and the ability to form perlite and ferrite at high cooling rates. Because of the low M_s and M_f temperatures, the austenite islands will form into a mixture of brittle martensite and retained austenite. The decreasing effect of the alloy elements on the M_s temperature can be seen from equation 2.4 [11].

$$M_s = 539 \quad -423(wt\%C) - 30.4(wt\%Mn) + 17.7(wt\%Ni) \\ +12.1(wt\%Cr) + 7.8(wt\%Mo) \tag{2.4}$$

Thermal weld simulation (TWS) is a way of reconstructing the changes in microstructure during welding. It is preformed by heating a piece of metal to a temperature that refers to a specific part of the HAZ. The cooling speed can also be designed so that it simulates the true heat flow during welding. Together, these two parameters make it possible to recreate every part of the heat affected zone during real time welding. Multipass welding can be simulated in a similar way by heating the metal sample several times to different temperatures.

2.2.1 Microstructure of API X70 steel after one cycle TWS

After undergoing a one-cycle thermal weld simulation test with a peak temperature of 1360°C and a cooling time $t_{8/5}$ of 30 seconds, Y. Wang et al. [14] observed a microstructure change from fine grain ferrite into coarse granular bainite.

Figure 2.3 shows the CCT diagram for a X70 steel, and indicates the resulting microstructure with different cooling rates.

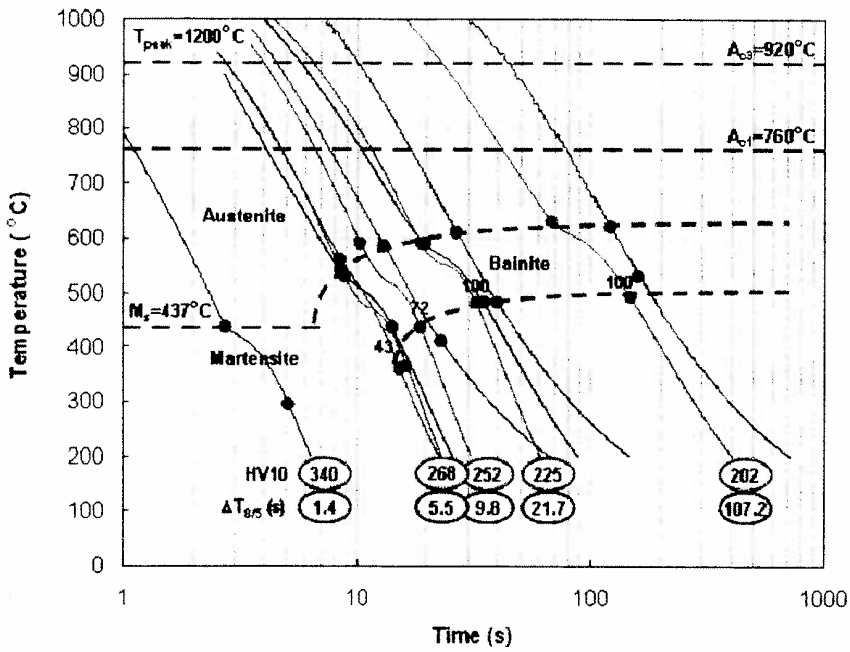

Figure 2.3: The continuous cooling transformation (CCT) diagram for API X70 steel [15].

2.3 Orientation relationship between FCC and BCC

The orientation relationship in the FCC–BCC transformation can be expressed in terms of close-packed planes and directions of the two phases. The Kurdjumov-Sachs (K–S) relationship describes the four close-packed $\{111\}_\gamma$-planes and the six BCC-variants that can form from each austenite plane, giving 24 preferred orientations of martensite from the parent austenite grain. The 24 theoretical BCC-variants can be plotted in a standard {100} pole projection figure, shown in figure 2.4. Each orientation is labeled with a combination of Roman (I–IV) and Arabic (1–6) numbering, referring to the four close-packed austenite planes and the six associated variants, respectively. The martensite orientations observed in an EBSD-scan can be directly compared to the theoretical variants in figure 2.4 and thus either prove or disprove the orientation relationship between FCC and BCC in the specific experiment.

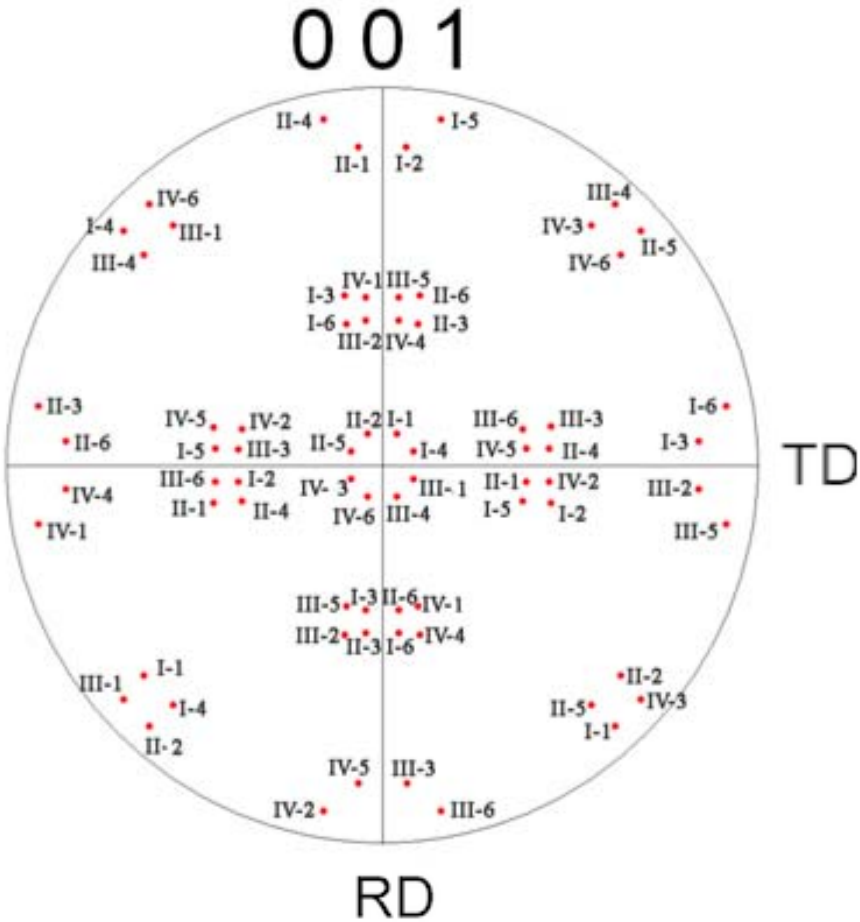

Figure 2.4: Standard {100} pole projection of the 24 possible K-S martensite variants originating from a single (001)[100] austenite orinetation. [16]

2.4 Sample preparation

Sample surface preparation is important in order to obtain good quality EBSD-patterns. The reason for this is that the EBSD-technique is dependent on analytical signals from the top 20 nanometers of the specimen [17]. Any surface deformation or surface contamination affects the signal quality, and hence the ability of obtaining reliable results during material analysis.

Chemical-mechanical polishing is proven to be a good way of getting a deformation free surface, which is required in order to get good diffraction patterns during EBSD [18]. By reacting with the active oxide suspension, the sample surface forms a brittle reaction layer that is easily removed by the sub-micron abrasives. This process is repeated continuously and results in a high metal removal. [18] In his depth study, the author [19] achieved great results using Struers OP-S to remove the deformation layer from API X70 steel samples, both before and after one cycle thermal weld simulation.

2.5 EBSD

2.5.1 Introduction

Electron Backscatter Diffraction (EBSD) is a method for characterizing the crystallographic orientation of polycrystalline materials in a scanning electron microscope (SEM). This technique can provide information about local grain orientation, grain boundaries and texture, in addition to phase identification and phase distribution on a crystalline surface. [17]

The recording of an EBSD-pattern is done by sending high-energy electrons on to a tilted crystalline sample facing a phosphor screen, as shown in figure 2.5. The phosphor screen should be placed with an optimal distance to the sample in order to detect a large amount of backscattered electrons. This is also the reason why the sample normal needs to be tilted relative to the electron beam. By increasing the tilt angle, more electrons are backscattered due to a more shallow electron penetration (sketched in figure 2.6). An angle of approximately 70° is typical during recording of EBSD-patterns. A lower tilt angle results in a lower signal to noise ratio, while a higher angle cause difficulties of obtaining high-quality patterns across the entire phosphor screen due to the high intensity gradients. [21]

The diffracted electrons are generated in the top 20 nm of the specimen surface by interaction between the backscattered electrons and the atomic planes. Diffraction of the backscattered electrons occurs according to Bragg's law:

$$2d_{hkl} \sin \theta_B = n\lambda \tag{2.5}$$

where d_{hkl} is the interplanar spacing, θ_B is the Bragg angle and λ is the wavelength of the incoming electrons. n is the order of reflection and is equal to 1 in EBSD. The interplanar

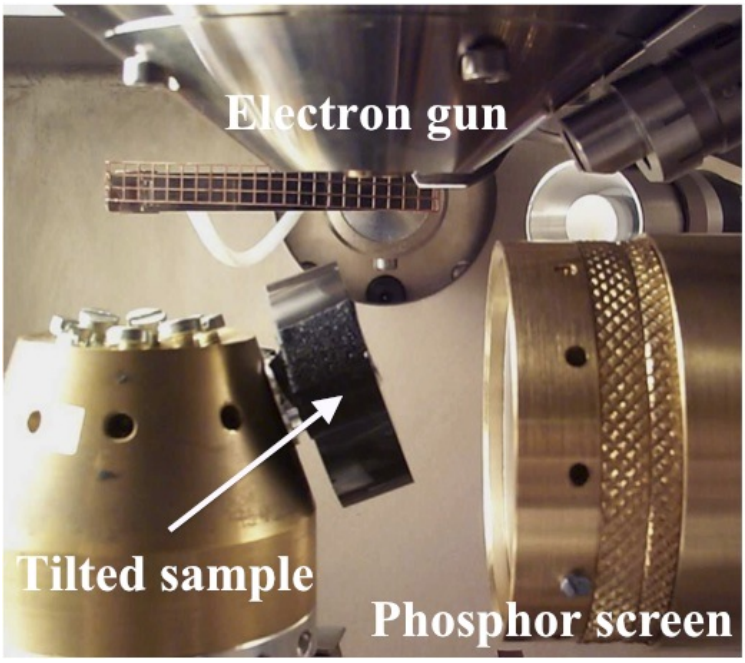

Figure 2.5: The relative positioning of the electron gun, the tilted specimen and the phosphor screen. [20]

spacing for cubic crystals can be found by equation 2.6:

$$d_{hkl} = \frac{a_0}{\sqrt{h^2 + k^2 + l^2}} \tag{2.6}$$

where a_0 is the lattice parameter while h, k and l are the Miller indices to the given atomic plane.

The result is the characteristic electron backscatter diffraction pattern, also known as Kikuchi pattern, presented in figure 2.7a [17]. The EBSD-pattern consists of what appears to be a number of bright bands on a flat surface (Kikuchi bands). In reality a band consists of two dark intensity minima lines with increased intensity in between. The increased intensity is a result of the increased probability of backscattering of electrons with reflecting angles between $[-\theta_B, \theta_B]$, referred to as the channeling effect. What appears to be two dark lines are really diffracting cones, sketched and exaggerated in figure 2.7b. For each diffracted plane a pair of high angular cones with the angle $180° - 2\theta_B$ are formed. In EBSD the θ_B is small, which makes the cone radius too big to notice, and they appear as straight lines.

Therefore, the centreline of each Kikuchi-band represents an atomic plane. Because the backscattered electrons interfere with more than one atomic plane, the diffraction pattern will consist of several bands. The intersection point between two Kikuchi-bands represents a crystal orientation in the material.

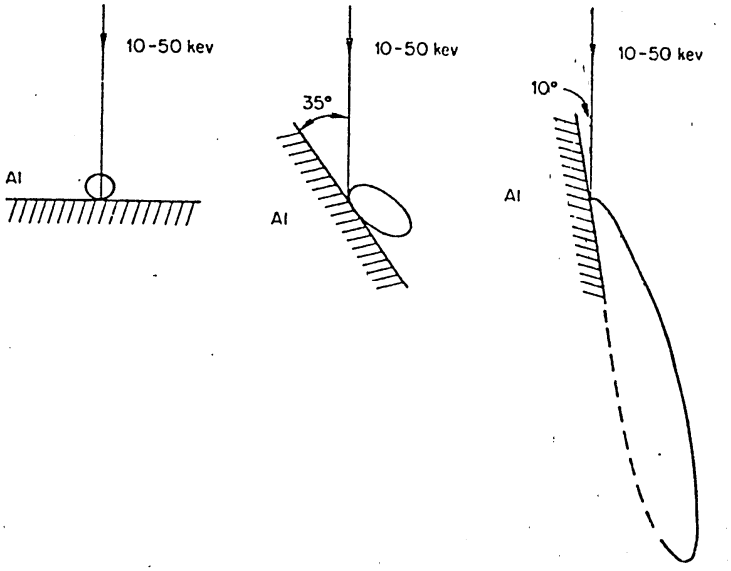

Figure 2.6: The sketch shows the influence of tilt angle on the amount of backscattered electrons. [22]

2.5.2 Operational Parameters

To be able to efficiently record EBSD-patters for a large scanned area, the SEM and the EBSD-camera need to be put into a control system. Figure 2.8 shows the information flow of a typical EBSD-system. While the electrons from the electron beam is backscattered into the phosphor screen, a CCD-camera records the Kikuchi-pattern and transfers the bitmap image to a computer. When the EBSD-software has received the pattern, a signal is sent to the SEM and the beam is moved one step length according to the predefined settings, and a new pattern is recorded. This action is repeated until the scan is complete.

The patterns can either be indexed on-line or off-line. On-line indexing is the conventional EBSD-system where each pattern is indexed before the electron beam is moved to a new position. In the very youth of the EBSD-technology the acquisition of the pattern was the limiting factor, while today the indexing is much more time consuming. The use of off-line systems, where the patterns are saved on a hard-disc for later to be indexed, is believed to become the future trend. [23] The off-line technique is supreme when it comes to speed, which is of special importance during in-situ experiments, but also vital due to enhanced economical aspects by allowing more users to access the microscope. The off-line EBSD-system is used in this project.

In order to get good and clear Kikuchi-patterns it is necessary to have a high signal/noise ratio during the aquistition. This can be achieved by using a long exposure time or a high beam current. A long exposure time will result in a long acquisition time, which is not favorable during in-situ experiments. The negative consequences of an increased beam current are restricted to a decrease in the spatial resolution. However, by using a field emission SEM (FESEM) the resolution degradation is somewhat limited. [20]

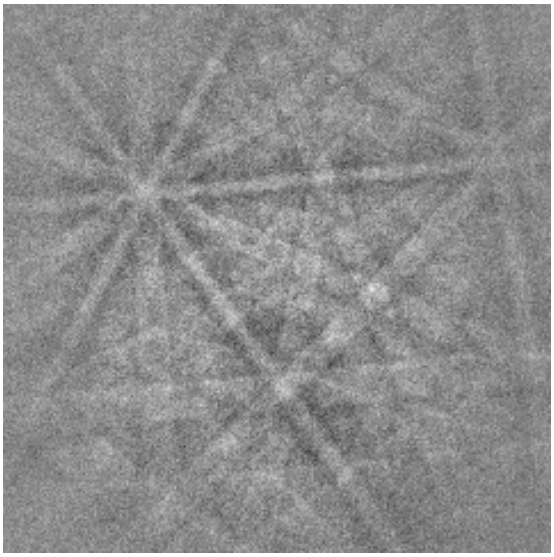

(a) Kikuchi pattern

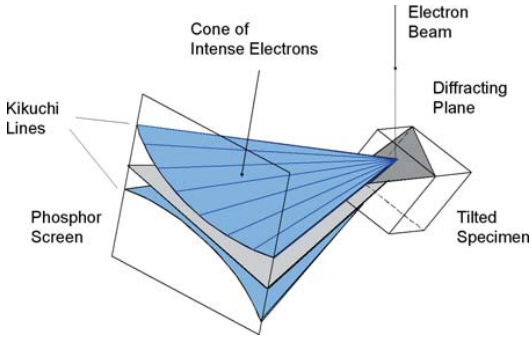

(b) Diffraction cones

Figure 2.7: (a) Example of an EBSD-pattern (Kikuchi pattern) from an API X70 arctic steel sample. (b) A schematic sketch of the diffraction cones, showing the electron beam, the atom plane and the phosphor screen. [17]

The acceleration voltage is an important parameter controlling the wavelength of the incident electron beam, and therefore indirectly the width of the Kikuchi-bands, according to Bragg's law in equation 2.5. A high accelerating voltage gives narrow bands, which makes it easier to locate the correct centre line. A negative consequence of increased beam voltage is the decreased spatial resolution due to a larger excitation volume. However, by reducing the beam voltage, both the sensitivity of the phosphor screen and the pattern intensity are likewise reduced. [17]

The step size affects the amount of indexed points. A large step size will give a coarse scan and therefore a high grain boundary fraction. If the step size is too small the noise close to the grain boundaries increase. According to Chen et al. the optimum step size is dependent on the magnification, shown in figure 2.9. [23]

The working distance (WD), together with the tilting angle, controls the position of the backscattered electron intensity on the phosphor screen. For the EBSD/SEM-system used in this project the optimal WD is between 20 and 22 mm with a tilting angle of 70°.

2.5.3 Indexing

To collect information about phase distributions and crystallographic orientations a software is needed to index each diffraction pattern in the scan. The TSL OIM Data Collection is used in this master thesis. One good calibration pattern must be recorded in each corner of the scan in order to calibrate the dynamic pattern center (PC). The PC is a point on the phosphor screen where the phosphor screen normal vector penetrates the point on the sample surface where the electron beam is focused. The PC is expressed with xyz-coordinates, where x and y gives the position on the phosphor screen while

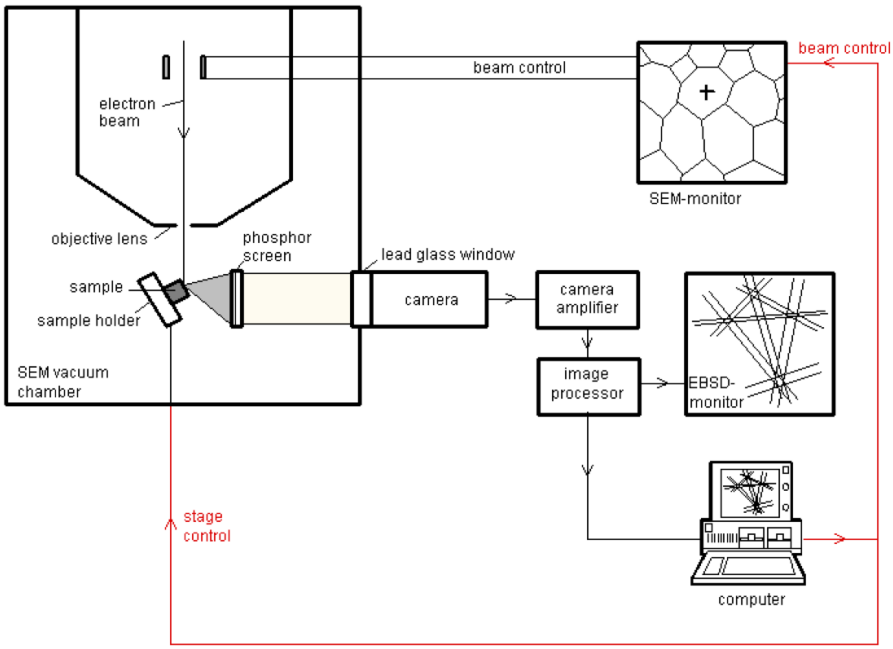

Figure 2.8: Scheme of a typical EBSD set-up. [20]

the z-value is the distance to the sample surface. The position of the PC is determined semi-automatically by finding the coordinates that gives the best correspondence between the recorded pattern and a reference pattern, as shown in figure 2.10. The software can help the user in finding the accurate position by tuning the coordinates based on various pattern quality parameters.

The Hough-transformation is based on the idea of transforming lines into points, in order to make it possible for the computer to detect the Kikuchi-bands. Figure 2.11 shows the different steps of the Hough-transform. A pixel in the xy-space is transformed into a sinusoidal curve by equation 2.7 below [24]:

$$\rho = x \cos\theta + y \sin\theta \tag{2.7}$$

Several points on a line in the xy-space will appear as a sinusoidal intersection point in the Hough-space. A dark line on the phosphor screen will therefore appear as a dark spot in the hough-space. Since the Kikuchi-band consists of one bright band between two dark lines, the Kikuchi-band will appear as one bright spot between two dark spots, referred to as the butterfly-effect. [24]

To be able to evaluate the quality of the EBSD-scan, TSL OIM Data Collection uses the three quality parameters CI (Confidence Index), Fit and IQ (Image Quality).

CI is the most important quality-parameter in the TSL software. A patented voting system is used where all possible band triplets are listed and compared to the different indexing solutions. In that way the software can calculate the probability of the best

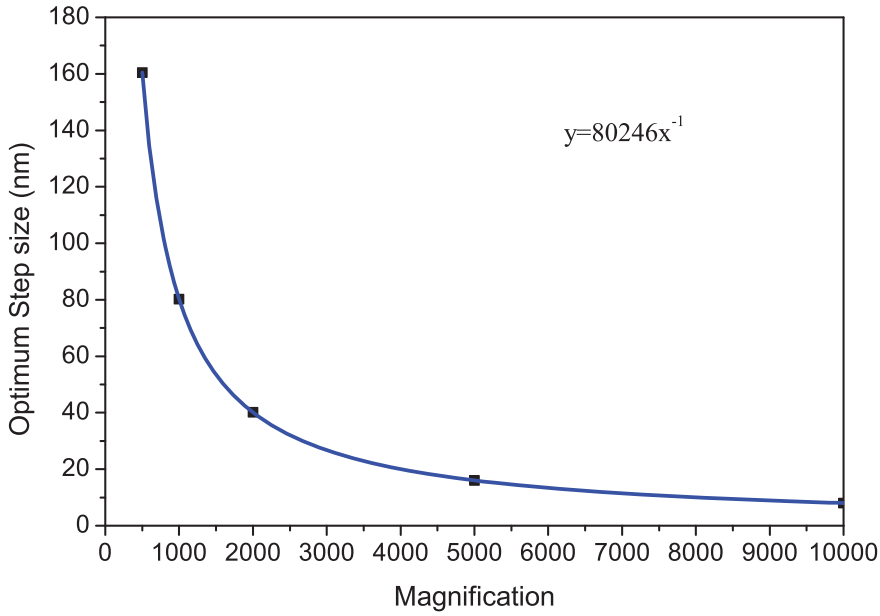

Figure 2.9: The optimum step size as a function of magnification. [23]

pattern-solution to be correct compared to the second best solution, according to equation 2.8 [25]:

$$CI = \frac{V_1 - V_2}{V_{IDEAL}} \tag{2.8}$$

where V_1 and V_2 are the number of votes for the best and second best solution, respectively, and V_{IDEAL} is the total number of possible votes from the band triplets. The reliability of the CI value was investigated by David P. Field [26], who came to the conclusion that 95% of the solutions were correct for a CI-value of 0.1 or greater.

The Fit-value is the angle deviation between the calculated band and the detected band. A low value represents a low deviation and the chosen orientation strengthens its chance of being correct. The Fit-value is used as the main parameter during fine-tuning iteration in TSL OIM Data Collection. [25]

IQ describes the average height of the peaks in the Hough-transform. The value is dependent on the strain in the diffraction area, the presence of impurities and the phase of the material, among others. An IQ-map can be established where the greyscale reflects the IQ-value of each pixel. A bright area refers to high IQ-values, whereas areas with low pattern quality will appear dark. [25]

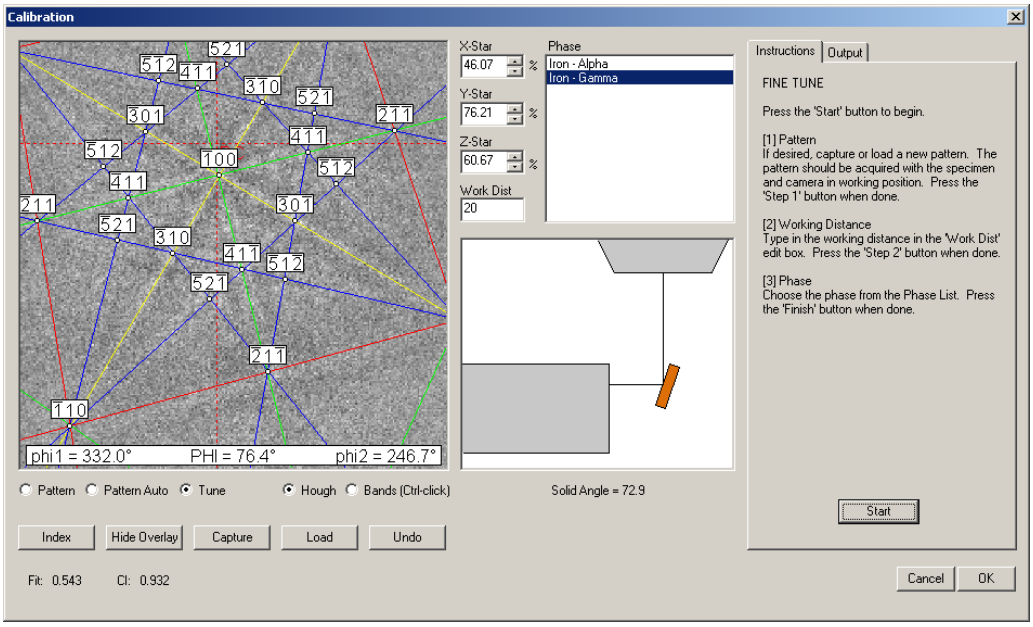

Figure 2.10: The calibration window in the software TSL OIM Data Collection 5.32. PC is determined by changing the coordinates in order to get good pattern quality values (Fit and CI).

2.5.4 Analysis

In order to process and analyze the indexed scan, another software from EDAX TSL can be used. TSL OIM Analysis 6.1 can provide information in the form of inverse pole figure (IPF) maps, phase maps and IQ-maps, among others. The IPF-map shows the crystallographic orientation to each point in the map by giving it an unique colour. The colours can be compared to the Inverse Pole Figure that shows the crystallographic orientation relative to the normal direction (ND) of the sample. [27] The phase map gives different colours to different phases in the material. The IQ-map is, as earlier mentioned, a way of showing the pattern quality in each indexed point throughout the scan. The IQ-map can provide information about grain boundaries, adhesive preparation stripes, particles and areas with higher dislocation density since these often gives a lower pattern quality. Figure 2.12 shows the IPF-map (a) with the associated inverse pole figure (b), the phase-map (c) and the IQ-map (d) for a duplex stainless steel.

The software can also give additional information about the scan quality. By running a two-step process the fraction of wrong indexed points can be measured. This is done by first running a clean-up using *Grain CI Standardization*. This method changes the CI-value of all points within a grain to the highest CI-value found inside that grain. The effect is shown in figure 2.13 where (a) and (b) represents before and after Grain CI Standardization, respectively. In this way the indexed points with the same orientation as the neighboring points is assumed to be correct, despite the low CI-value. Points with a low CI-value, but with an orientation different from that of the neighboring points, do not change.

Step two is to remove the remaining points with low CI-value, typically below 0.05. The

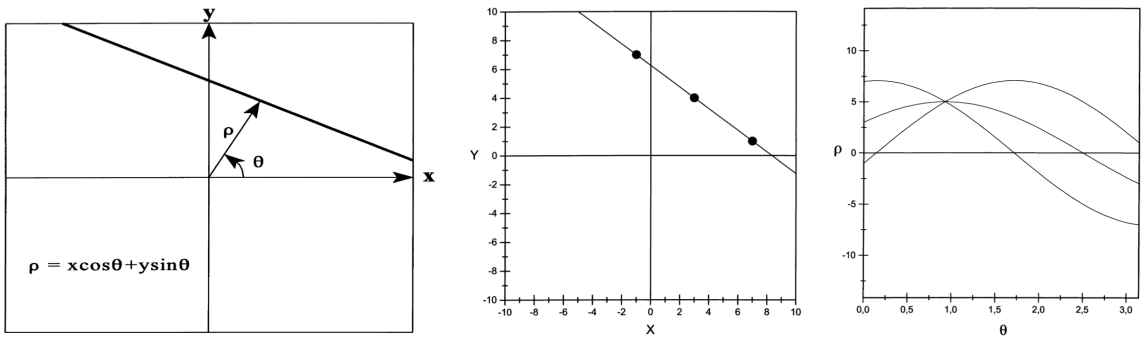

(a) (b) (c)

Figure 2.11: The Hough-transformation. (a) The illustration explains how a pixel in the xy-space is transformed into a sinusoid curve in the Hough-space. (b) through (c) shows three points on a line in the xy-space intersect and form a point in the Hough-space. [24]

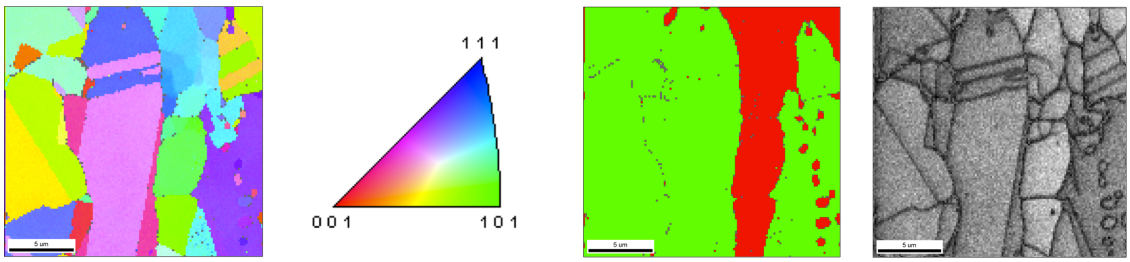

(a) IPF-map (b) Inverse pole figure (c) Phase-map (d) IQ-map

Figure 2.12: (a) The IPF-map with (b) the associated inverse pole figure, (c) the phase-map and (d) the IQ-map of a duplex stainless steel (DSS).

measured fraction of unindexed points gives an additional indication of the scan quality. [27]

2.6 In Situ EBSD

The EBSD-technique is often limited to analysis of the microstructural changes of a material before and after an applied thermal or mechanical load. In situ experiments enable a direct observation of the changes in a given area as they appear. The method can be used on several materials to better understand the structural changes and phase transformations due to mechanical deformation or heating. Both tensile testing and heat treatment experiments have been combined with in situ EBSD characterization by various authors [16][28][29].

High scan speed is essential during in situ experiments. It shortens the time of measurements and thus alleviates the difficulties with long-term stability of the SEM during in situ experiments [17]. The ultra-fast off-line indexing EBSD-system, described in section 2.5.2, is a suitable replacement to the traditional on-line system.

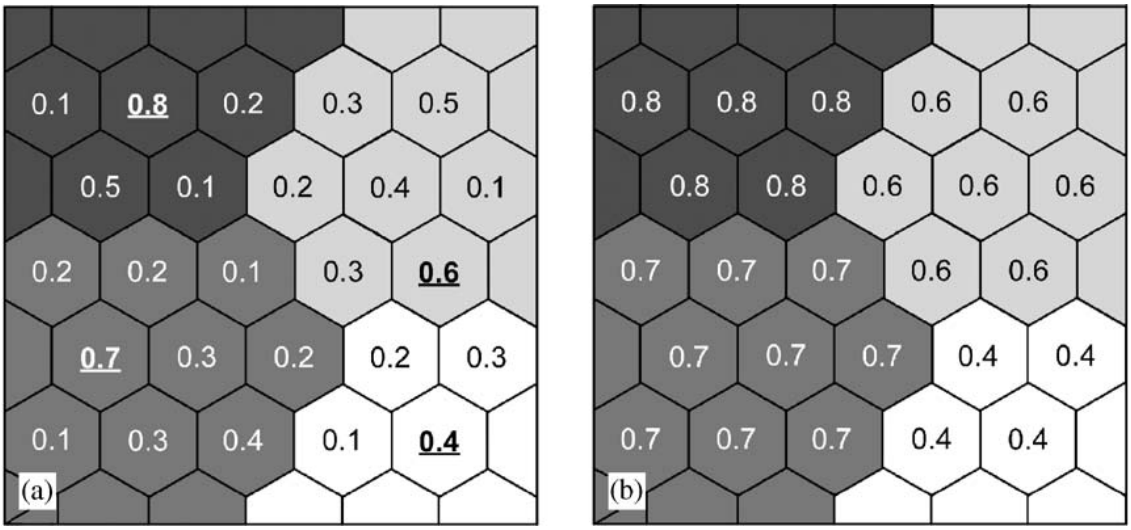

Figure 2.13: The principle of Grain CI Standardization Clean-up. [21]

2.7 In Situ Heating

A method for observing phase transformations and changes in crystal orientation during a welding procedure is needed to be able to fully understand the formation of the hazardous MA-islands in low alloy steel. Earlier attempts of combining the electron backscatter diffraction (EBSD)-technique with in situ heating have been performed.

A.-J. Enstad [28] achieved to heat a HSLA-steel sample into the two-phase ferrite (α) and austenite (γ) region of the Fe-C phase diagram inside a scanning electron microscope (SEM). By reheating a one-cycle thermal simulated steel sample while running multiple EBSD-scans throughout the holding time, it was possible to observe the formation of austenite on the grain boundary. However, due to low cooling rate in vacuum, no MA-phases was observed in the final material. The development of a rapid cooling device was suggested as further work.

2.8 In Situ Quenching

In earlier studies performed by the author [19] and fellow student T. G. Sætran [30] different cooling medias were tested in vacuum conditions. By putting a cold medium (-140°C) in contact with a hot steel sample (400°C) inside a vacuum chamber, the idea of contact cooling was tested. The result of 2°C/sec showed that heat transfer was extremely difficult to achieve in vacuum conditions. A revolutionary idea of venting the vacuum chamber through a nozzle pointing directly onto a hot steel sample was established. Promising results were observed by using cold argon gas as the quenching medium. Gas quenching has the advantage of directly cooling the specimen top surface where the EBSD-characterization takes place. The convective heat transfer can be expressed by equation 2.9

$$q' = a(T_s - T_g) \tag{2.9}$$

where T_s and T_g are the temperatures of the steel sample and the gas, respectively, and a is the heat transfer coefficient:

$$a = \frac{C \cdot v^{0.7} \cdot \rho^{0.7} \cdot c_p^{0.31} \cdot \lambda^{0.69}}{d^{0.3} \cdot \eta^{0.39}} \tag{2.10}$$

C is a constant, v is the gas speed, ρ is the pressure, c_p is the heat capacity of the gas, λ is the heat conductivity, η is the dynamic viscosity of the gas while d represents a geometric factor. [31]

It was suggested by Hansen and Sætran that by replacing the argon gas by a noble gas with a higher heat capacity, e.g. helium, the cooling rate could increase. Table 2.1 shows the thermal properties for argon and helium.

Table 2.1: Thermal properties for argon (Ar) and helium (He) [32]

	Heat capacity (c_p) [$JK^{-1}g^{-1}$]	*Thermal conductivity (λ)* [$Js^{-1}m^{-1}K^{-1}$]
Argon (Ar)	0.52	0.018
Helium (He)	5.19	0.15

Chapter 3

Experimental

3.1 Material

API X70, the material studied in the presented work, is a commercially low alloy pipeline steel known for its high strength and toughness, even at very low temperatures. The chemical composition is shown in table 3.1 below:

Table 3.1: Chemical composition of the experimental steel (API X70)

C	*Si*	*Mn*	*P*	*S*	*Al*	*Cu*	*Cr*	*Ni*	*Mo*	*V*	*Nb*	*Ti*	*N*	*Ca*
0.047	0.1	1.74	0.09	0.0006	0.035	0.21	0.055	0.235	0.045	0.0008	0.027	0.01	0.0026	0.001

3.2 Dilatometric Analysis

A dilatometer is an instrument that measures the expansion during a physical or chemical reaction. A steel rod (5mm x 5mm x 25mm) was carefully heated to a peak temperature of 950°C with a heating rate of 5°C/sec. The volume change during heating was measured with a Netzsch DIL 402 C instrument, shown in figure 3.1 . Disregarding the phase transformation the thermal expansion coefficient in steel is constant. A change in the $temperature - volume\ change$-slope will therefore imply the occurrence of a phase transformation. These measurements can provide information about the Ac_1- and Ac_3-temperature for the chosen steel during slow heating.

3.3 Weld Simulation

Prior to the experiments the steel was subjected to a one cycle thermal weld simulation with a heating rate of 100°C/sec and a peak temperature of 1350°C, followed by a cooling time between 800°C and 500°C, $\Delta t_{8/5}$, of 5 seconds. The thermal weld simulation was performed on steel rods with the dimensions 11mm x 11mm x 70mm by a Smithweld TCS model 1405. In order to get accurate temperature measurements a thermocouple was spot

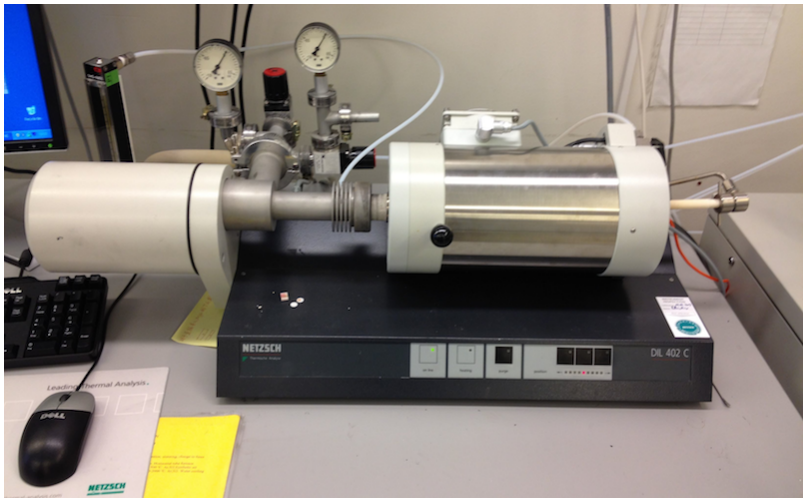

Figure 3.1: The dilatometric analysis equipment Netzsch DIL 402 C.

welded to the surface of each steel rod. Figure 3.2 shows the temperature during a weld simulation test.

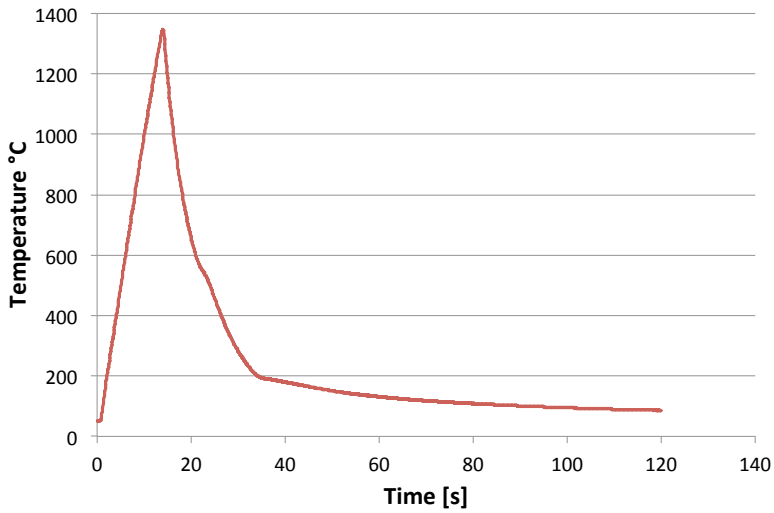

Figure 3.2: The heating/cooling curve during a thermal weld simulation test.

A dilatometric analysis of the steel is also possible during the thermal weld simulation. To be able to measure the volumetric change heating the dilatometer was fixed on two sides of the steel rod. By doing these measurements both the Ac_1 and Ac_3 for rapid heating of the steel can be found experimentally.

3.4 Sample Geometry

The weld simulation rods were machined out from a hot rolled steel plate, as shown in figure 3.3. After the thermal weld simulation each rod were spark eroded into the final

sample geometry (11mm x 12 mm x 3mm). A hole was drilled at the end of each sample (red spot) as a site for the thermocouple. The hole measured 0.52 mm and 0.60 mm in the first and second batch of machined samples, respectively.

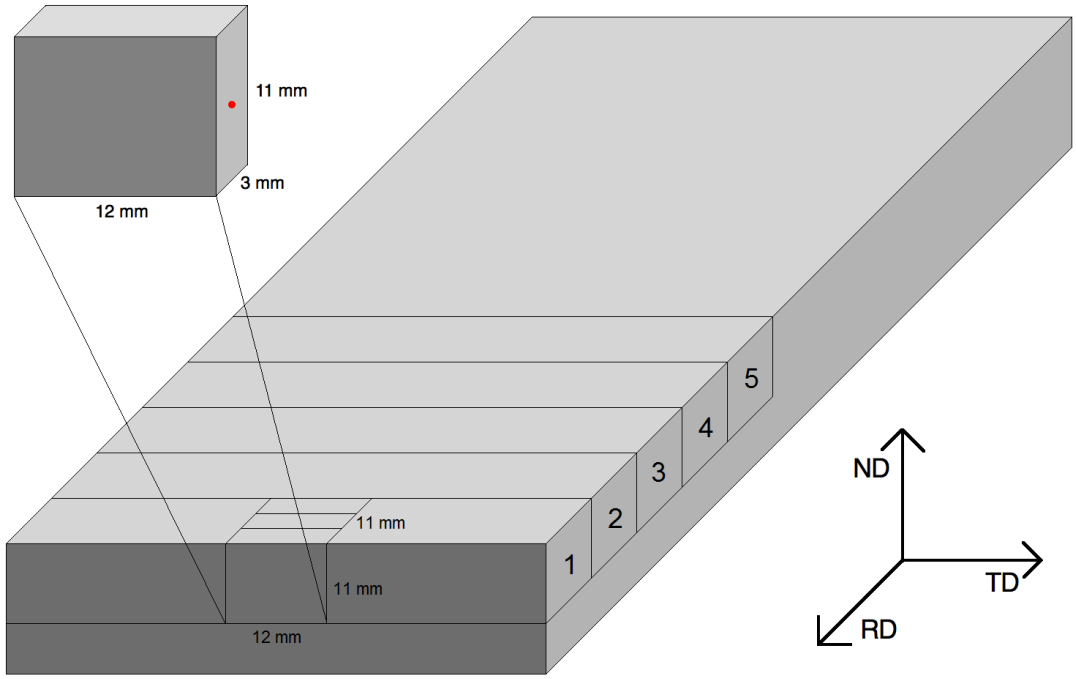

Figure 3.3: The sketch shows how the samples are machined out from the hot rolled steel plate.

3.5 Sample Preparation

Sample preparation is important to remove any surface deformation and thus to obtain high quality EBSD-patterns. In his depth study the author tested several specimen preparation techniques where the use of chemical-mechanical polishing showed good and reproducible results [19]. The same preparation technique is used in the current master thesis.

The X70 specimens was wet grinded using a "Struers TegraPol" for 5 minutes at each of the following steps: 80, 320, 500, 800, 1200, 2400. The samples were cleaned with water and ethanol between each grinding step. The final preparation steps, including chemical-mechanical polishing with Struers OP-S, were performed according to table 3.2.

In order to remove any residuals of resin or other chemical components, the samples were submerged in an ultrasonic bath containing acetone for 30 minutes. The samples were then cleaned in ethanol for 5 minutes to remove the acetone, before being purified in Fishione 1020 Plasma Cleaner for 5 minutes. "Plasma cleaning both removes existing carbonaceous debris from the specimen and also prevents contamination from occurring during imaging and analysis" inside the SEM [33].

Table 3.2: Preparation steps using chemical-mechanical polishing.

Step	*Dispersion*	*Grain size*	*Time*	*Force*
1	Diapro Allegro	9 μm	5 min	35 N
2	Diapro Dac	3 μm	5 min	50 N
3	Diapro Nap-B	1 μm	10 min	25 N
4	OP-S	0,04 μm	10 min	15 N

3.6 EBSD

The scanning electron microscope used in this project is a Zeiss Gemini Ultra 55 Limited Edition, shown in figure 3.4. This microscope is a high vakuum SEM with a field emission (FE)-emitter, which enables a high beam current while maintaining a high resolution.

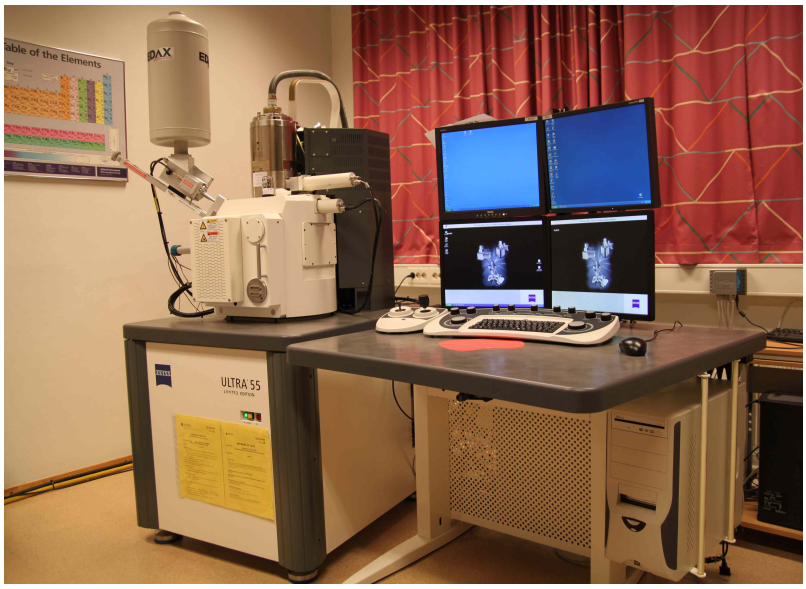

Figure 3.4: Zeiss Gemini Ultra 55 Limited Edition SEM.

The EBSD-detector NORDIF UF-1000 was used together with the software NORDIF 1.4.0 in order to acquire and save the EBSD-patterns on the computer hard drive. TSL OIM Data Collection 5.32, a NORDIF-compatible edition of TSL OIM Data Collection 5.31, and TSL OIM Analysis 6.1, both from EDAX Inc., were used for indexing and analyzing, respectively.

The SEM-settings used for the characterization of the materials are shown table 3.3 bellow:

3.6.1 Acquisition of Patterns

A representative area of the specimen surface was first found in the SEM using the secondary electron detector. The surface area was then scanned into the NORDIF software as shown in figure 3.5.

Table 3.3: SEM-settings during characterization

Settings	*Values*
Accelerating voltage	20 kV
Beam current	50 - 100 nA (High current mode)
Aperture	300μm
Magnification	500 X
Tilt angle	70°
Working distance	19 - 21 mm
Dynamic focus	2 - 3%

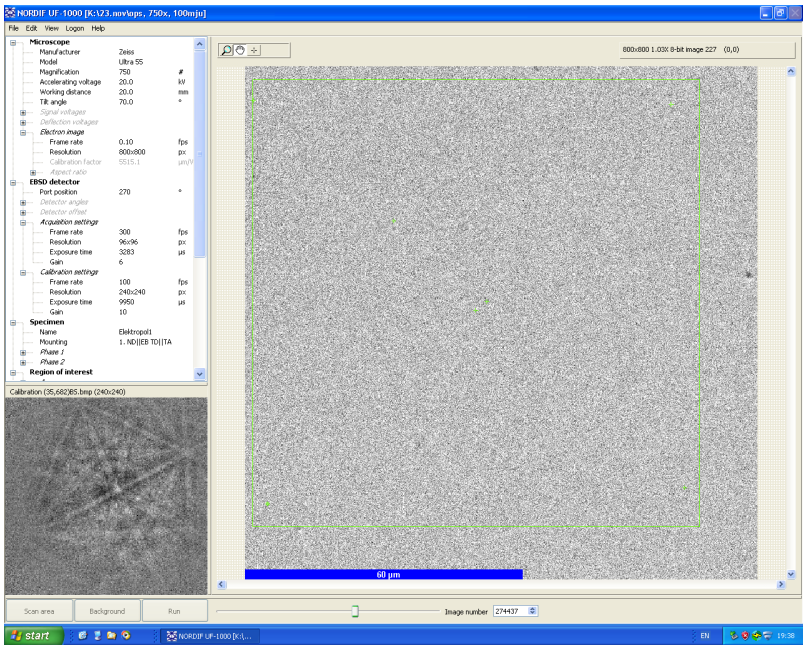

Figure 3.5: Screen shot of NORDIF 1.4.0.

Before the EBSD-scanning, parameters from the SEM including magnification, accelerating voltage, working distance (WD) and tilt angle were typed into the text box to the left in figure 3.5. Then the settings for both calibration and acquisition were change to optimize both pattern quality and acquisition speed. Due to the thermal expansion of the steel sample and the furnace the electron image was drifting during high temperature exposure. Therefore a high acquisition speed is more important for the scans acquired at elevated temperature than the scans performed before heating or after quenching. The chosen settings are shown in table 3.4.

The resolution of the pattern image was chosen to be 96 x 96 pixels. This corresponds to a 5 x 5 binning, meaning that the CCD-camera becomes 25 times more sensitive to light while the pattern image size is reduced by a factor of 25. In this way the exposure time can be reduced and hence the scan speed will increase. The intensity can also be increased electronically by increasing the *Gain*. This will, however, give some noise in the picture, but not more than the Hough-transform can handle.

Table 3.4: NORDIF-settings during characterization

	Before heating	**At 800 °C**	**After cooling**
Acquisition settings			
Frame rate	300 fps	700 fps	300 fps
Resolution	96 x 96	96 x 96	96 x 96
Gain	1	2	1
Calibration settings			
Frame rate	100 fps	100 fps	100 fps
Resolution	240 x 240	240 x 240	240 x 240
Gain	0	0	0
Region of interest			
Width	100 μm	40 μm	100 μm
Height	100 μm	40 μm	100 μm
Step size	0.2 μm	0.2 μm	0.2 μm

While acquisition settings are based on the compromise between speed and quality, the calibration settings are chosen only on the basis of of good pattern quality.

Four calibration patterns and one acquisition pattern were recorded before EBSD-scanning started. The calibration patterns are recorded in each corner of the scanning area in order calibrate the dynamic pattern centre during indexing (as explained in section 2.5.3). One acquisition pattern is typically recorded in the centre of the scanning area in case of a bad quality scan and thus the need for a pattern comparison.

3.6.2 Indexing

TSL OIM Data Collection 5.32 was used to index the NORDIF pattern files. In order for the program to distinguish between the expected phases in the steel, both ferrite and austenite had to be loaded into the software before the calibration. The indexing parameters are shown in table 3.5.

3.6.3 Analyzing

TSL OIM Analysis 6.1 was used to compare the steel microstructure within the same area before heating, at elevated temperature and after quenching. The scans done before heating and after quenching were cropped to only include the surface area scanned at elevated temperature. Inverse Pole Figure (IPF)-, Phase- and Image Quality (IQ)-maps were made. The colors of the IPF-maps refers to the crystallographic orientation compared to a Inverse Pole Figure. Every IPF-map in this master thesis is referred the Inverse Pole Figure shown in figure 2.12.

Table 3.5: Settings for TSL OIM Data Collection

Hough-transform	
Hough Type	Classic
Hough Resolution	Low
Binned Pattern Size	96
Theta Step Size	1°
Rho Fraction	90%
Max/Min Peak Count	8/3
Convolution Mask	Medium (9x9)
Min Peak Magnitude	5
Min Peak Distance	15
Peak Symmetry	0.50
Vertical Bias	0%
Hough Time	0.0080

3.7 The Heating Device

The heating was done with existing heating equipment designed by Rémi Chiron at the CNRF research center, and further developed by Anne-Jorunn Enstad at NTNU [28]. The heating system consists of a furnace placed inside a specially developed hot stage and a computer to detect the sample and furnace temperature and thus control the power supply, all imaged in figure 3.6. The furnace has a maximum temperature of 800°C, just above the two-phase (α+γ) region of low alloy steel.

3.8 Development of Quenching Device

The cooling unit used in this experiment was designed and developed with respect to the existing furnace/hot stage. Due to the limited power of the furnace, and the importance of reaching the two-phase (α+γ) region, it was of vital importance that the cooling device did not generate any heat loss during heating. As mentioned in section 2.8, gas quenching was considered to be a promising method for achieving rapid cooling. This method produces no heat loss during operation of the furnace.

An experimental vacuum chamber (figure 3.7a) developed by Tor A. Nilsen was used in the initial stages of gas quenching testing. Figure 3.7b shows the set-up inside the vacuum chamber. The idea was to vent the vacuum chamber through the nozzle directly on the hot specimen surface, using a noble gas as the cooling medium. In this way, the gas quenching would not inflict more damage to the vacuum chamber than during a normal ventilation. Vital and expensive components like the turbo-molecular pump would not be risked.

After a series of tests inside the experimental vacuum chamber the development of a cooling system inside the SEM was initialized. The cooling system consisted of a rig that was mounted to the stage inside the SEM, a tube that was aimed towards the sample surface and a vacuum-tight gas connection for the SEM. These can be seen in figure

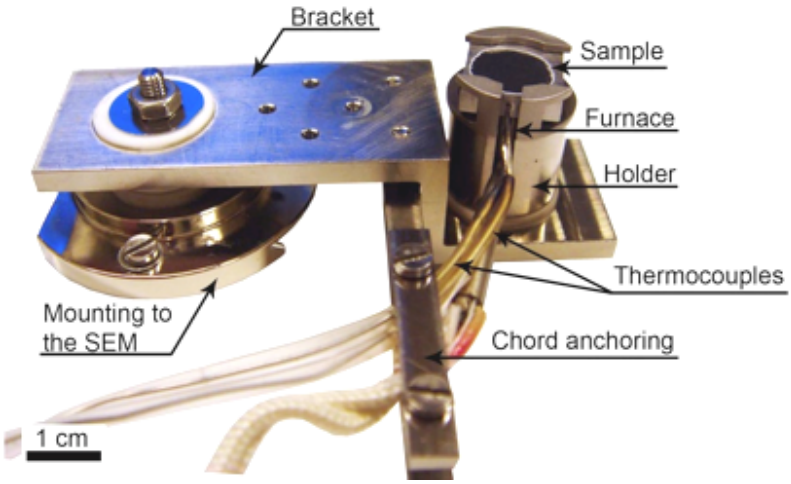

(a) The hot stage and the furnace [28]

(b) The computer and the power supply

Figure 3.6: The heating system, showing (a) the hot stage including furnace and thermocouples, and (b) the computer and power supply.

3.8. For detailed information regarding the rig itself, please see the assembly manual in appendix B. All components were made from stainless steel. A Teflon® tube was used inside the SEM to connect the gas connection with the stainless steel tube on the rig.

It was important not to risk any damage on the turbo-molecular pump during ventilation. In addition to modifying the SEM for alternative venting by the cooling gas through the gas nozzle, a regulator was installed between the pressurized tank and the valve, allowing a maximum overpressure of 0.3 bar. 0.3 bar is specified as the maximum inlet pressure during ventilation of Zeiss Gemini Ultra 55 Limited Edition FESEM.

(a) Experimental vacuum chamber

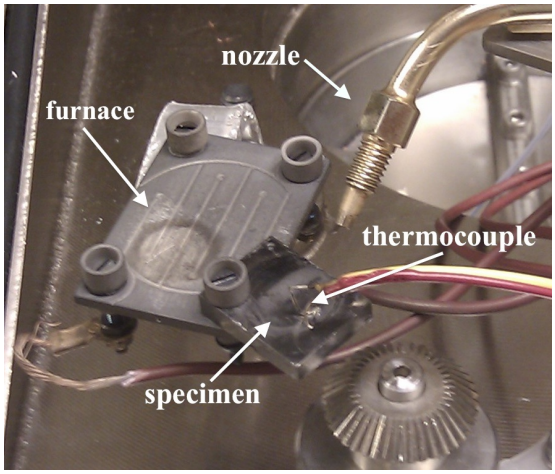

(b) Initial gas quenching set-up

Figure 3.7: The experimental vacuum chamber used to design and test the potential of gas quenching, (a) outside and (b) inside, showing the initial set-up, including the furnace, the steel sample, the thermocouple and the gas nozzle.

3.9 In Situ Heating and Quenching

During the in situ experiments it was of vital importance to know the correct temperature of the steel sample. As mentioned in section 2.8 earlier work performed by the author reviled difficulties regarding thermal transition in vacuum conditions. Poor heat transfer between the thermocouples and the sample and furnace was therefore believed to be a problem during the experiments, and thus allowing incorrect temperature measurements.

It was considered to spot weld a thermocouple to each steel specimen, but due to the danger of overheating the sample, and thus affecting the microstructure, the idea was rejected.

Instead a K-type thermocouple was spot welded to a reference steel sample before it was mounted to the heating stage, as shown in figure 3.9. The steel sample was then heated to approximately 800°C and the deviation between the different thermocouples were measured.

In order to improve the thermal conductivity during heating a thin layer of platinum paint was applied between the furnace and the steel sample. The platinum paint was applied

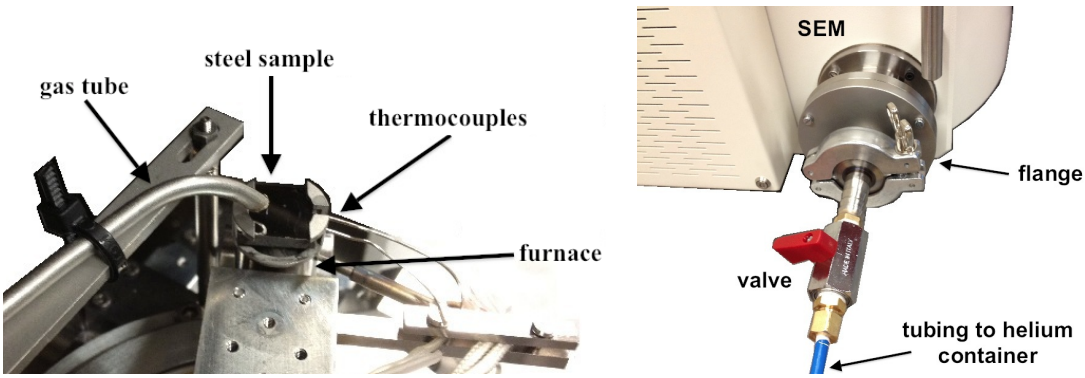

(a) Hot stage and cooling rig (b) Gas connection

Figure 3.8: The specially designed cooling system, including (a) the hot stage with the cooling rig and (b) the vacuum-tight gas connection to the SEM.

between the furnace and a new sample and dried in an incubator for two hours at 75°C, before each in situ experiment.

During the in situ experiments carefully prepared one cycle thermal weld simulated samples were mounted to the heating stage before an 100μm x 100μm EBSD-scan was done. The samples were heated with a heating rate of 1°C/sec to a temperature of approximately 800°C. Each sample was held at the peak temperature for approximately 10 minutes in order to stabilize the thermal expansion and hence avoid drift in the EBSD-scan. To limit the high temperature holding time a smaller 40μm x 40μm scan was recorded inside the selected area of the first EBSD-scan. When the scan was finished the EBSD-detector was immediately pulled out before the sample holder was rotated in order to aim the gas nozzle towards the steel sample surface. The SEM was then ventilated by helium gas throughout the nozzle. After rapid quenching a new 100μm x 100μm EBSD-scan was recorded.

To avoid overheating of the SEM fine mechanics an additional thermocouple was attached to the hot stage near the mounting point (figure 3.6a) to carefully monitor the temperature. The critical upper temperature limit was set to 47°C.

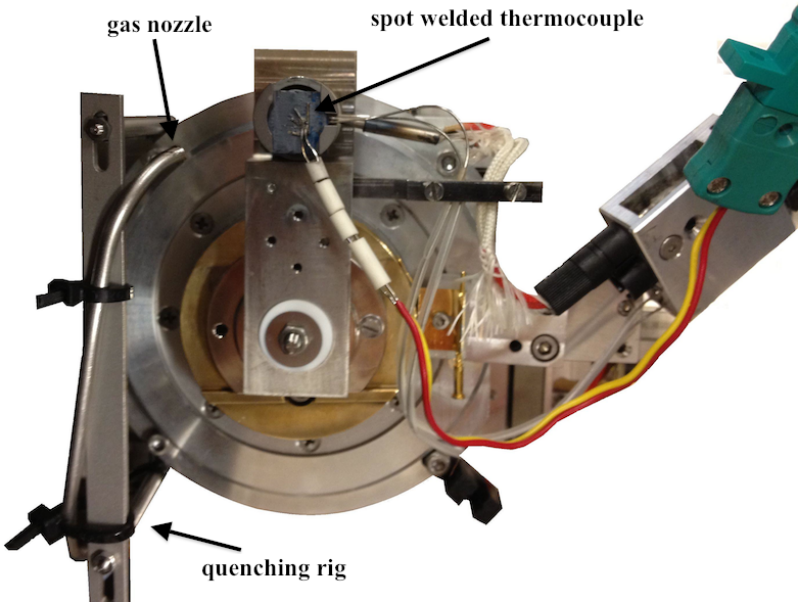

Figure 3.9: The heating and cooling system seen from above. A thermocouple is spot welded to the sample surface to measure the real sample temperature during heating. The quenching rig with the gas nozzle can be seen to the left in the picture

Chapter 4

Results

4.1 Dilatometric analysis

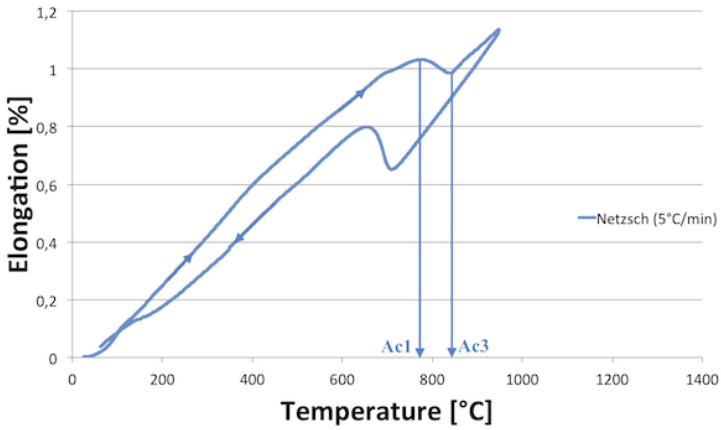

Figure 4.1: The dilatometric analysis curve recorded with Netzsch DIL 402 C.

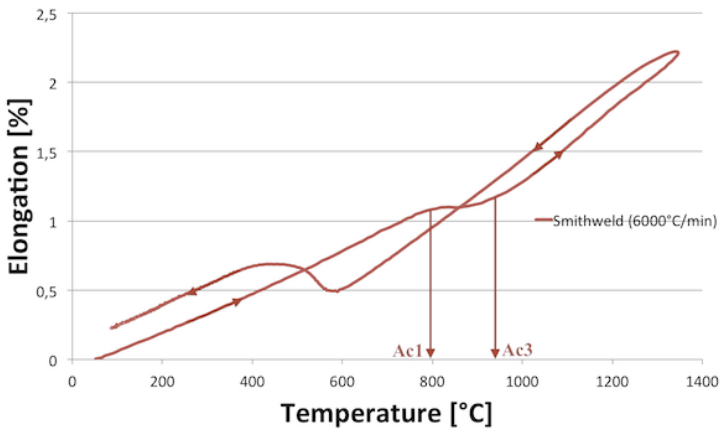

Figure 4.2: The dilatometric analysis curve recorded with Smithweld TCS model 1405.

The dilatometric curves in figure 4.1 and 4.2 show the phase transformation temperatures for the API X70 steel at low (5°C/min) and high (6000°C/min) heating rate, respectively. The Ac_1 and Ac_3 found for the two heating rates are, together with the theoretical calculated temperatures, shown in table 4.1. The theoretical values are calculated from equation 2.2 and 2.3 in section 2.1.

Table 4.1: Comparison between experimental and theoretical values of Ac_1 and Ac_3 for API X70 steel.

	Theory	*Dilatometry (5° C/min)*	*Dilatometry (6000° C/min)*
Ac_1	704°C	770°C	790°C
Ac_3	868°C	830°C	950°C

4.2 Development of Quenching Device

4.2.1 Cooling Curves

Figure 4.3a shows the cooling curves recorded inside the experimental vacuum chamber. The contact cooling curve recorded in earlier experiments performed by the author is included for comparison [19]. Effort was made to cool the argon gas before it quenched the steel sample. A higher cooling rate was not achieved, either because it took too long before the cold gas reached the nozzle and the sample surface or due to ice blocking of the gas tube.

Figure 4.3b shows a typical cooling curve from the newly developed in situ quenching device and a typical cooling curve recorded during a traditional thermal weld simulation with the Smithweld TCS model 1405 using a cooling rate $t_{6/4}$=5.4 sec.

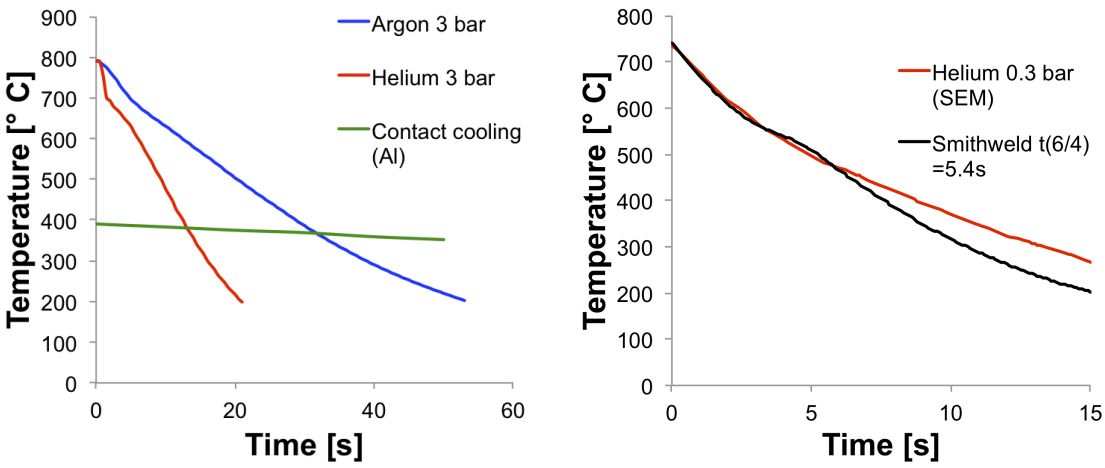

(a) Experimental vacuum chamber

(b) SEM

Figure 4.3: The cooling curves recorded inside the experimental vacuum chamber and inside the SEM. (a) Different cooling media are compared inside the experimental vacuum chamber. (b) Cooling curves from a rapid gas quenching test inside the SEM and from a traditional thermal weld simulation are shown.

4.2.2 Calibration of Temperature Measurements

Figure 4.4 shows the temperatures measured with three different thermocouples during two heating tests. The sample used for the first test had a drilled thermocouple hole of 0.52mm while the second sample had a hole measuring 0.60mm. These samples and their holes were representative to the first and second batch of machined samples. The furnace thermocouple and the sample thermocouple (both with a diameter of 0.52mm) are the thermocouples used during a normal in situ heating and quenching experiment. In order to ensure proper contact and thus getting a more correct measurement of the sample temperature the external thermocouple was spot welded to the sample surface. More results from the first sample batch is presented in appendix C.

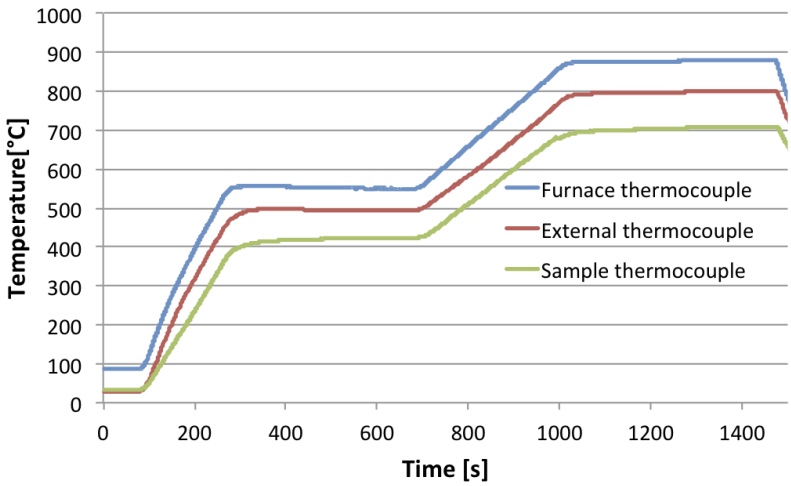

(a) First sample batch

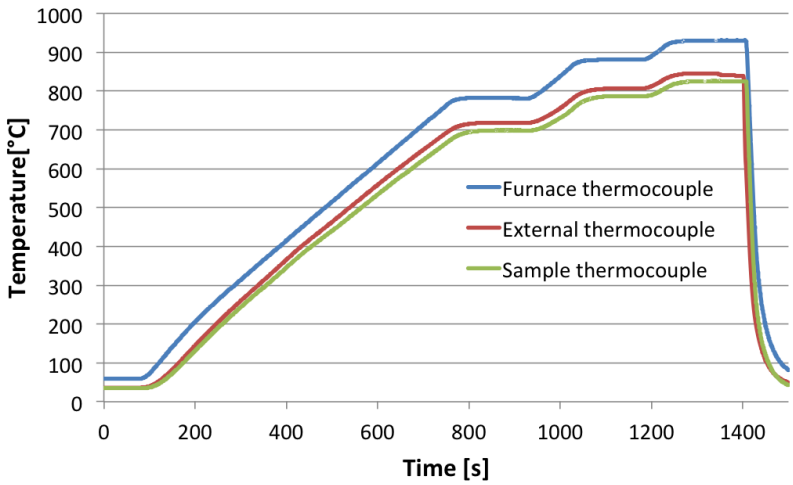

(b) Second sample batch

Figure 4.4: The temperature calibration tests performed on a sample with a machined thermocouple hole measuring (a) 0.52mm and (b) 0.60mm.

4.2.3 Comparison of Microstructures

The following section compares the resulting microstructure after a second cycle in situ heating and quenching (H/Q) experiment with the microstructure obtained after traditional thermal weld simulation (TWS). The different heating and quenching parameters of each sample are shown in table 4.2. ΔT_H, T_{p1} and T_{p2} refers to the heating rate and the peak temperature during first and second heating cycle, respectively. $\Delta t_{8/5}$ and $\Delta t_{6/4}$ indicates the cooling time from 800°C to 500°C and from 600°C to 400°C, respectively. Sample 10 – in situ H/Q had a high temperature holding time of 15 minutes. The 20°C added are a result of the measuring error found in section 4.2.2.

Light microscope images, inverse pole figure (IPF) maps, phase maps and IQ-maps are presented in figure 4.5 through 4.9. The arrows point out examples of former austenite grain boundaries. The IPF and phase maps from the EBSD scans have been cleaned according to the technique described in section 2.5.4. Pixels with a CI-value lower than 0.05 are assumed to be incorrect indexed and are therefore removed from the maps (appear black). Red and green color in the phase maps represents BCC- and FCC-structure, respectively. Table 4.3 shows the fraction of removed pixels as well as the fraction of austenite in each scan.

Table 4.2: Heating and cooling parameters for traditional TWS vs. in situ H/Q.

Sample	*First weld cycle*			*Second weld cycle*		
	ΔT_H	T_{p1}	$\Delta t_{8/5}$	ΔT_H	T_{p2}	$\Delta t_{6/4}$
9 – 1 cycle TWS	100°C/s	1354°C	4.8 s			
10 – in situ H/Q	100°C/s	1347°C	4.9 s	1°C/s	813+20°C	6.4 s
17 – 2 cycle TWS	100°C/s	1351°C	5.0 s	100°C/s	798°C	3.6 s
18 – 2 cycle TWS	100°C/s	1357°C	14.8 s	100°C/s	786°C	19.0 s
21 – 2 cycle TWS	100°C/s	1357°C	14.7 s	100°C/s	813°C	18.0 s

Table 4.3: The fraction of points removed due to a CI-value below 0.05 and the fraction of remaining austenite.

Sample	*Fraction CI<0.05*	*Fraction austenite*
9 – 1 cycle TWS	0.020	0.005
10 – in situ H/Q	0.023	0.003
17 – 2 cycle TWS	0.023	0.006
18 – 2 cycle TWS	0.024	0.006
21 – 2 cycle TWS	0.058	0.004

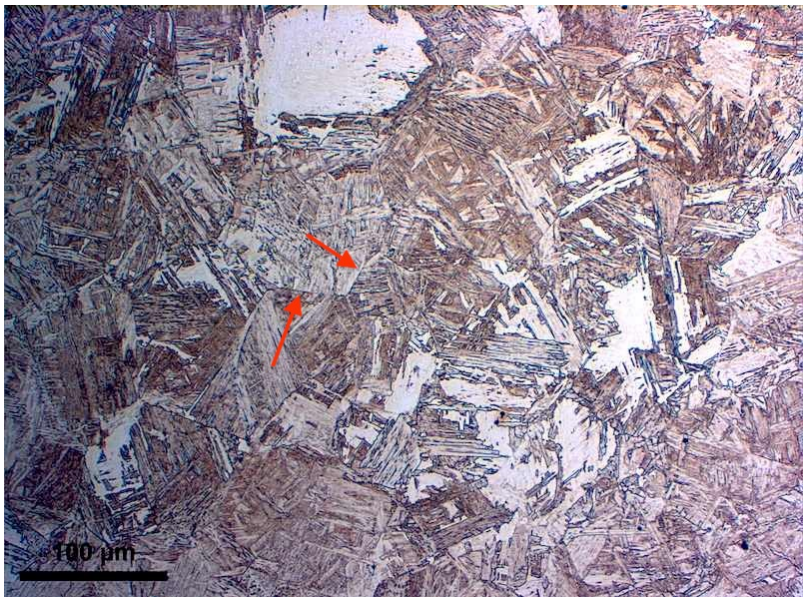

(a) 9 - 1 cycle TWS. The arrows show former austenite grain boundaries.

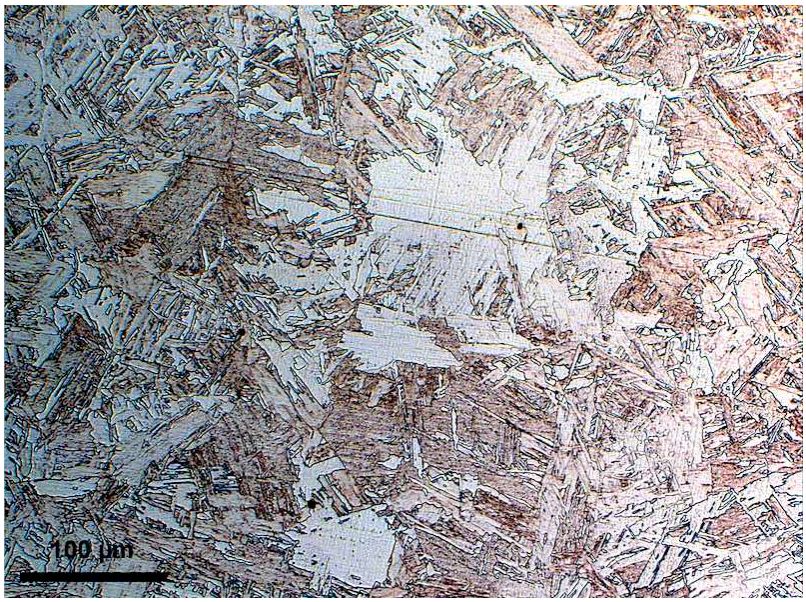

(b) 10 - In situ H/Q: $\Delta t_{6/4}$=6.4s, T_{p2}=813°C

Figure 4.5: Light microscope images of the differently heat treated steel samples.

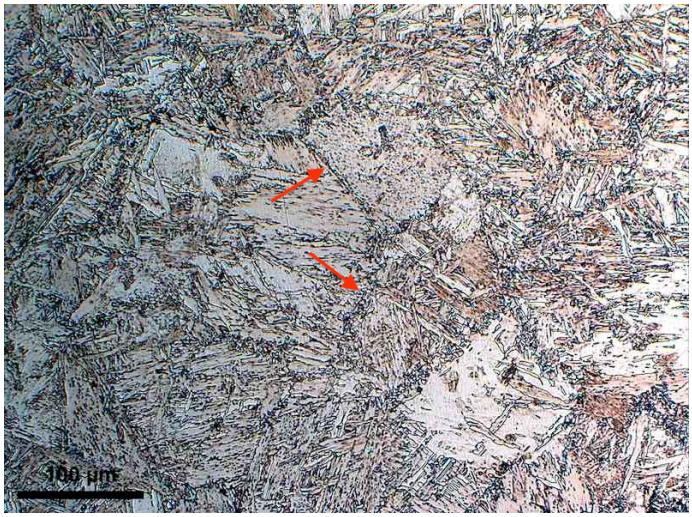

(a) 17 - 2 cycle TWS: $\Delta t_{6/4}$=3.6s, T_{p2}=798°C

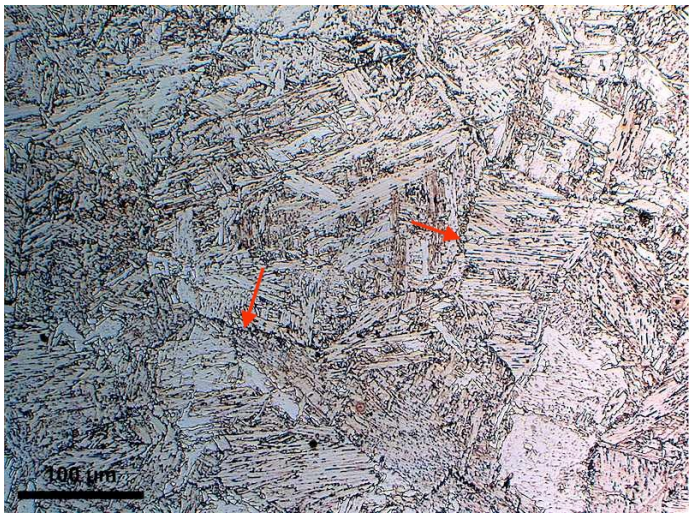

(b) 18 - 2 cycle TWS: $\Delta t_{6/4}$=19s, T_{p2}=786°C

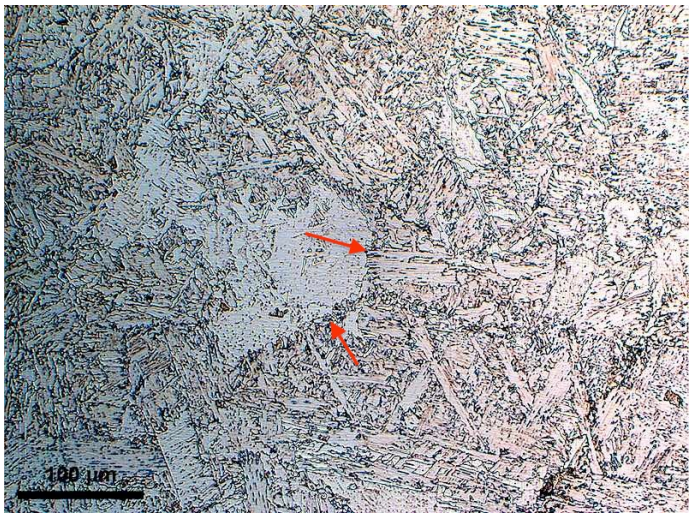

(c) 21 - 2 cycle TWS: $\Delta t_{6/4}$=18s, T_{p2}=813°C

Figure 4.6: Light microscope images of the differently heat treated steel samples. The arrows show former austenite boundaries.

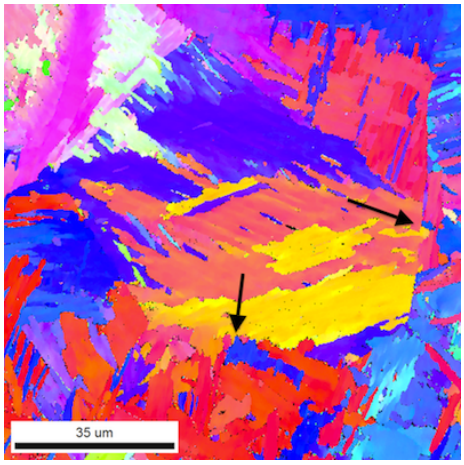

(a) 9 - 1 cycle TWS

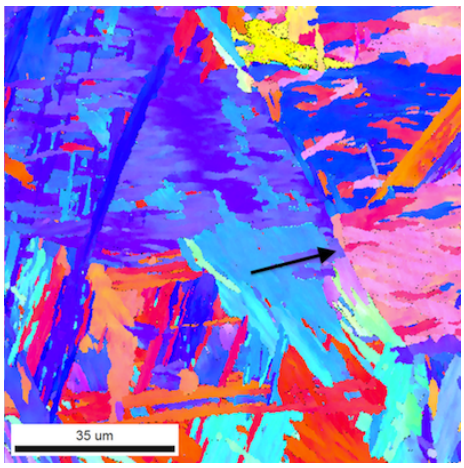

(b) 10 - In situ H/Q: $\Delta t_{6/4}$=6.4s, T_{p2}=813°C

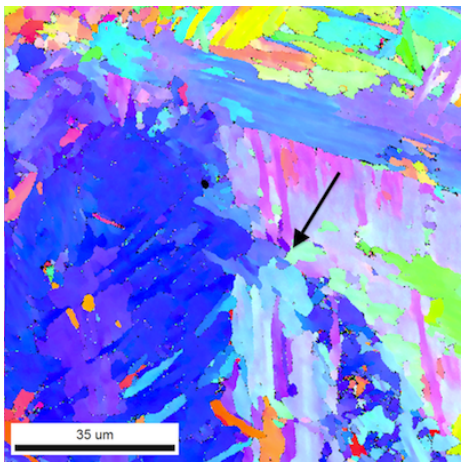

(c) 17 - 2 cycle TWS: $\Delta t_{6/4}$=3.6s, T_{p2}=798°C

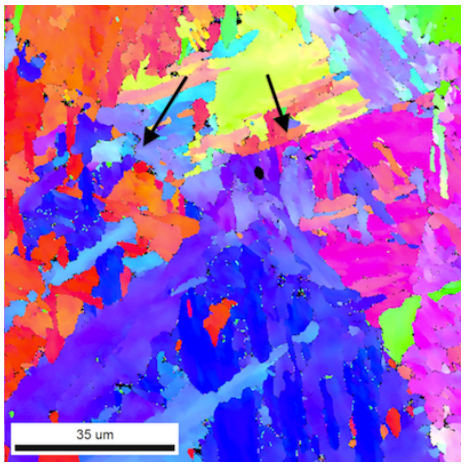

(d) 18 - 2 cycle TWS: $\Delta t_{6/4}$=19s, T_{p2}=786°C

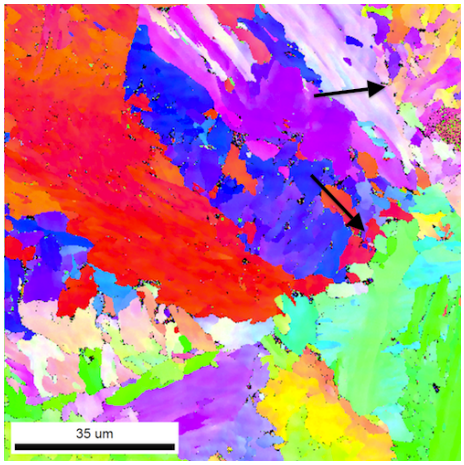

(e) 21 - 2 cycle TWS: $\Delta t_{6/4}$=18s, T_{p2}=813°C

Figure 4.7: IPF-maps of the differently heat treated steel samples. The arrows show what appears to be former austenite grain boundaries.

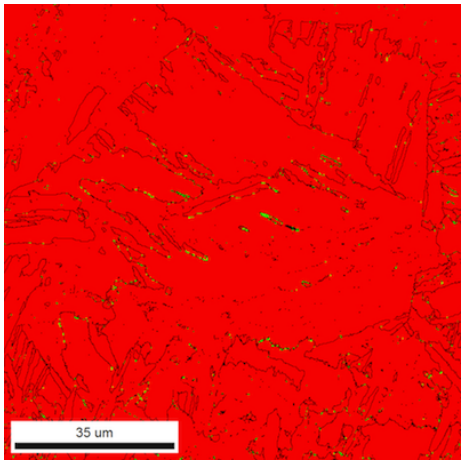

(a) 9 - 1 cycle TWS

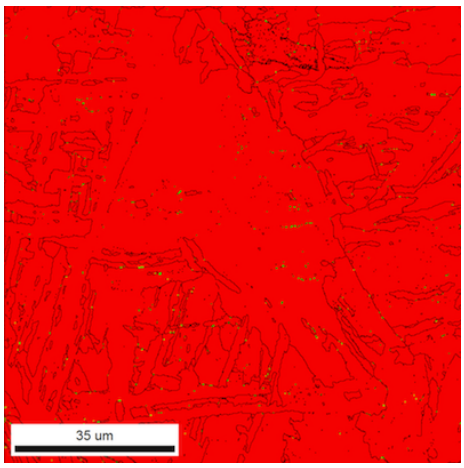

(b) 10 - In situ H/Q: $\Delta t_{6/4}$=6.4s, T_{p2}=813°C

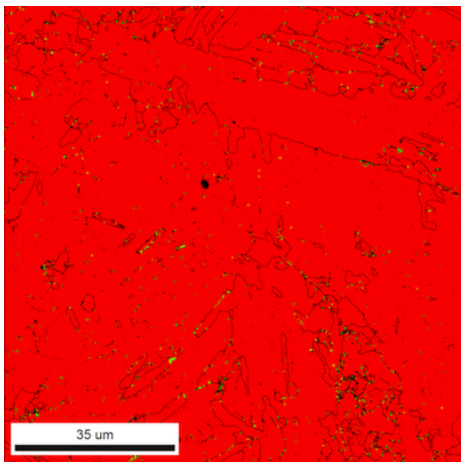

(c) 17 - 2 cycle TWS: $\Delta t_{6/4}$=3.6s, T_{p2}=798°C

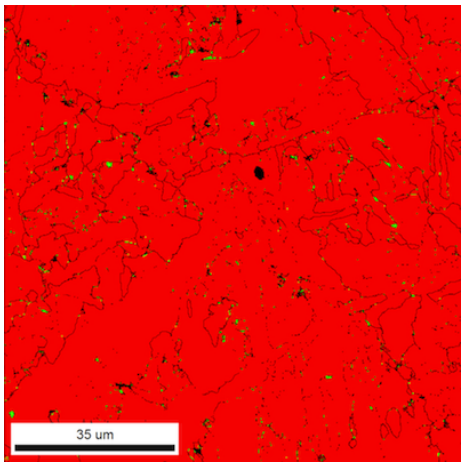

(d) 18 - 2 cycle TWS: $\Delta t_{6/4}$=19s, T_{p2}=786°C

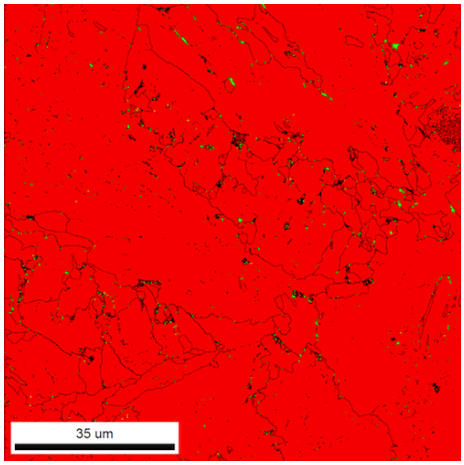

(e) 21 - 2 cycle TWS: $\Delta t_{6/4}$=18s, T_{p2}=813°C

Figure 4.8: Phase maps of the differently heat treated steel samples.

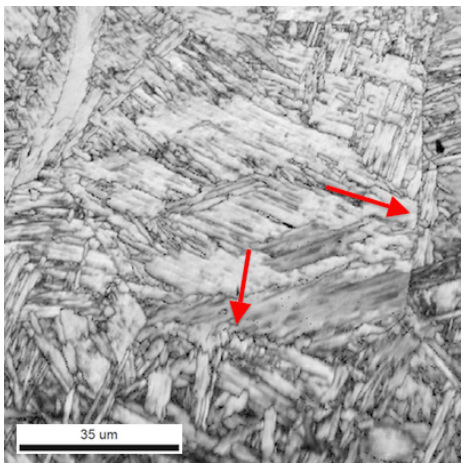

(a) 9 - 1 cycle TWS

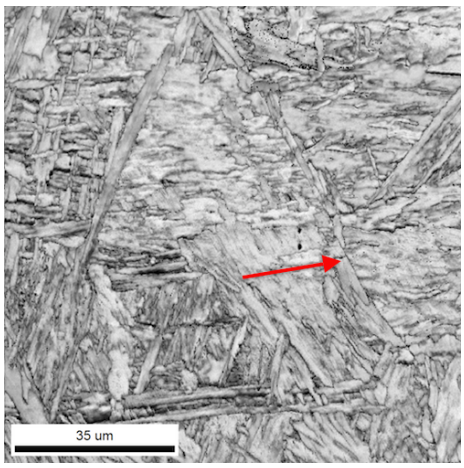

(b) 10 - In situ H/Q: $\Delta t_{6/4}$=6.4s, T_{p2}=813°C

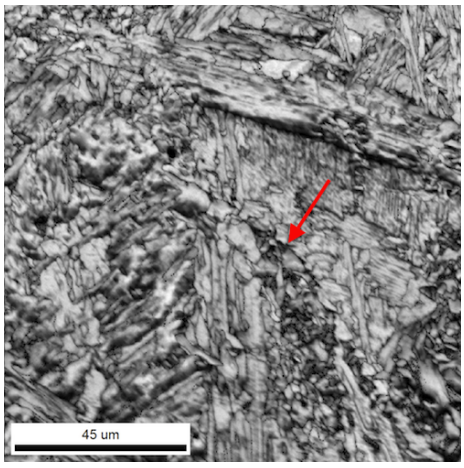

(c) 17 - 2 cycle TWS: $\Delta t_{6/4}$=3.6s, T_{p2}=798°C

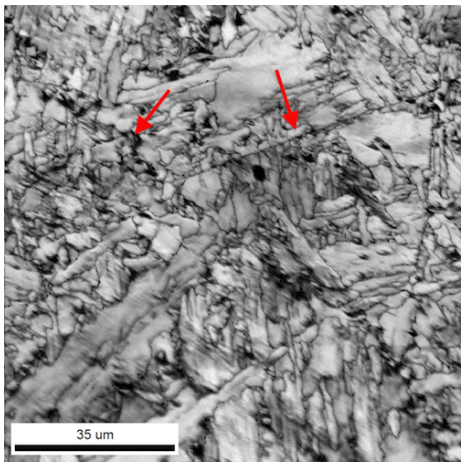

(d) 18 - 2 cycle TWS: $\Delta t_{6/4}$=19s, T_{p2}=786°C

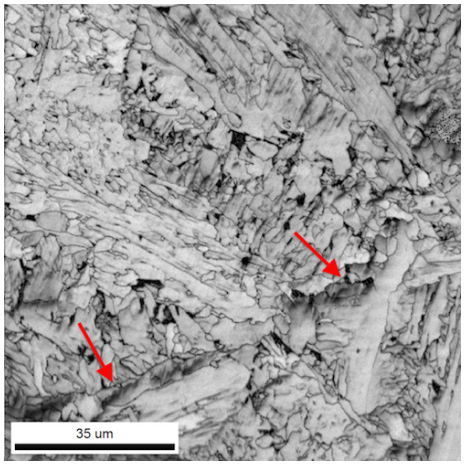

(e) 21 - 2 cycle TWS: $\Delta t_{6/4}$=18s, T_{p2}=813°C

Figure 4.9: IQ-maps of the differently heat treated steel samples. The arrows show what appears to be former austenite grain boundaries.

4.3 Contamination

The gas quenching led in some in situ H/Q experiments to a permanent contamination layer on the steel sample surface. The contamination was worst directly below the gas nozzle but could in some cases cover most of the sample surface. Figure 4.10 shows the extent of contamination on two different samples. Figure 4.10a shows a slightly affected sample, whereas the sample in figure 4.10b is heavily contaminated.

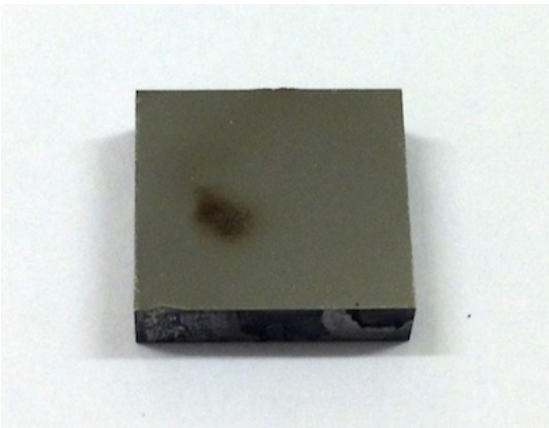

(a) Slightly contaminated sample

(b) Heavily contaminated sample

Figure 4.10: The contamination of the steel sample surface varies from (a) almost non-present to (b) extremely domainant.

4.3.1 EBSD characterization of contaminated area

Table 4.4: EBSD quality parameters of the scans in figure 4.11 and the fraction of remaining austenite.

Scan	*Average CI-value before clean-up*	*Average CI-value after clean-up*	*Fraction CI<0.05*	*Fraction austenite*
Before heating	0.53	0.57	0.057	0.006
After quenching	0.13	0.87	0.392	0.793

During some in situ experiments the contaminated spots appeared too close to or on the selected scan area. This influenced the diffraction patterns and later the indexing. The indexing problems are visualized in figure 4.11. The figure shows two phase maps and two inverse pole figure (IPF)-maps, obtained from an EBSD-scan done before heating (a)(b) and an EBSD-scan done after gas quenching (c)(d), respectively. The scans have been cleaned according to section 2.5.4 and points with a CI-value lower than 0.05 is removed and appear black. Red and green color in the phase maps represents BCC- and FCC-structure, respectively. Quality parameters are given in table 4.4 in addition to the fraction of indexed austenite.

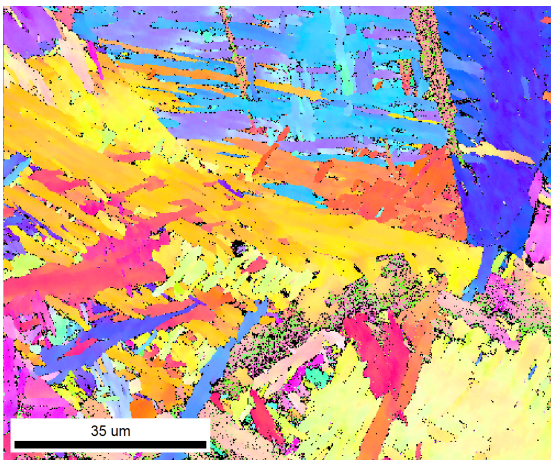

(a) IPF-map before heating

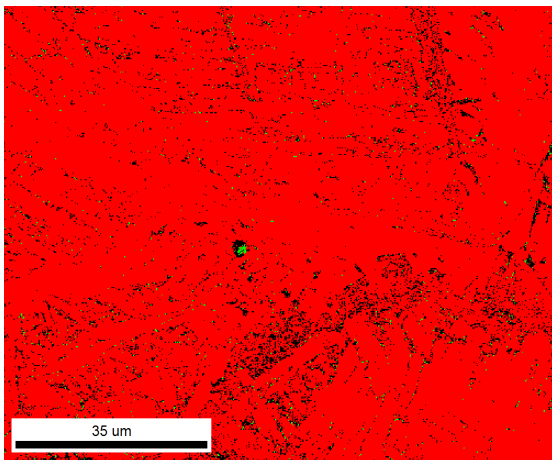

(b) Phase-map before heating

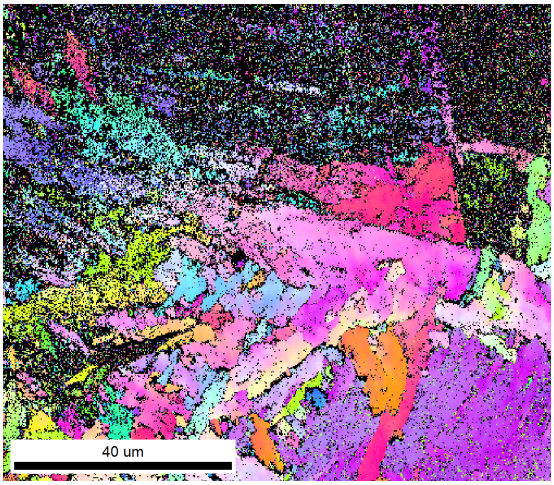

(c) IPF-map after gas quenching

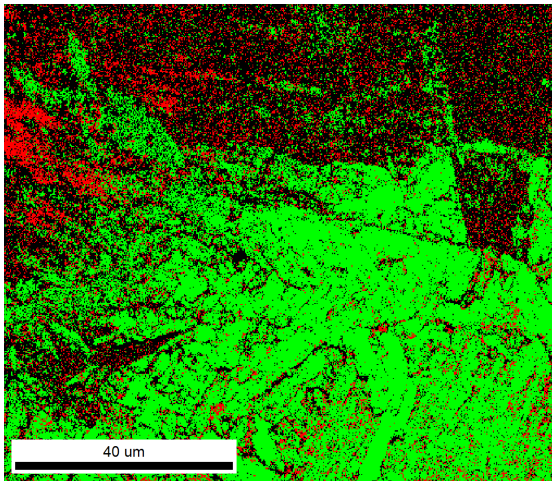

(d) Phase-map after gas quenching

Figure 4.11: An EBSD-scan of the same sample surface area done before heating and after gas quenching. The IPF-maps are presented in (a) and (c), while (b) and (d) show the phase-maps.

4.3.2 Effect of pre-flushing

The gas system was then pre-flushed with helium for 30 seconds during vacuum pumping of the SEM in order to reduce the extent of contamination on the sample surface. Figure 4.12 shows two different samples, one without (a) and one with (b) the use of pre-flushing before heating and quenching.

4.3.3 EPMA-analysis of contaminated surface

Finally the contamination layer was analyzed using an Electron Probe Micro-Analyzer (EPMA). Six quantitative chemical spot analysis were done on a contaminated area while

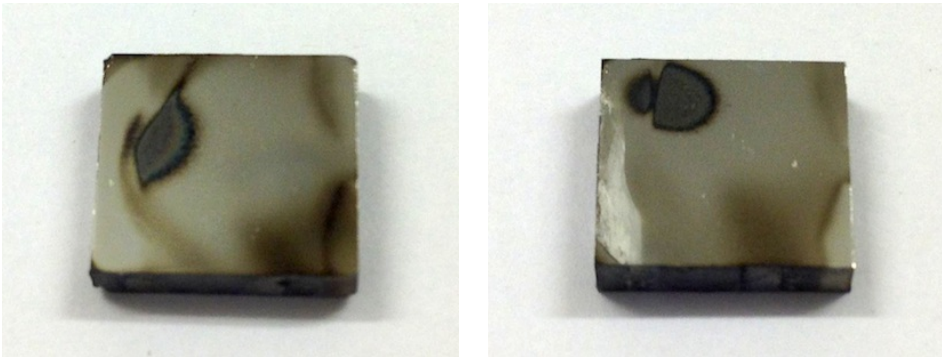

(a) Without pre-flushing (b) With preflushing

Figure 4.12: The contamination of two steel samples with the same parameters (a) without and (b) with pre-flushing of the system.

six more were done at an area without contamination. Both areas are from the same sample surface. The average chemical composition of these measurements are presented in table 4.5 together with the standard deviation within each area. Figure 4.13 compares the oxygen-map of an area without contamination with that of a heavily contaminated one. The intensity scale bar is included.

Table 4.5: The average element content of a surface area without and with contamination layer expressed in weight per cent.

Surface area	*Si*		*O*		*C*		*Cr*		*Ni*		*Mn*		*Cu*	
	$\bar{x}$	σ	$\bar{x}$	σ	$\bar{x}$	σ	$\bar{x}$	σ	$\bar{x}$	σ	$\bar{x}$	σ	$\bar{x}$	σ
Contaminated	0.08	0.02	6.33	2.87	0.13	0.02	0.06	0.02	0.20	0.04	0.24	0.02	0.12	0.04
Not Contaminated	0.08	0.01	0.43	0.05	0.11	0.00	0.05	0.02	0.19	0.05	0.27	0.03	0.12	0.06

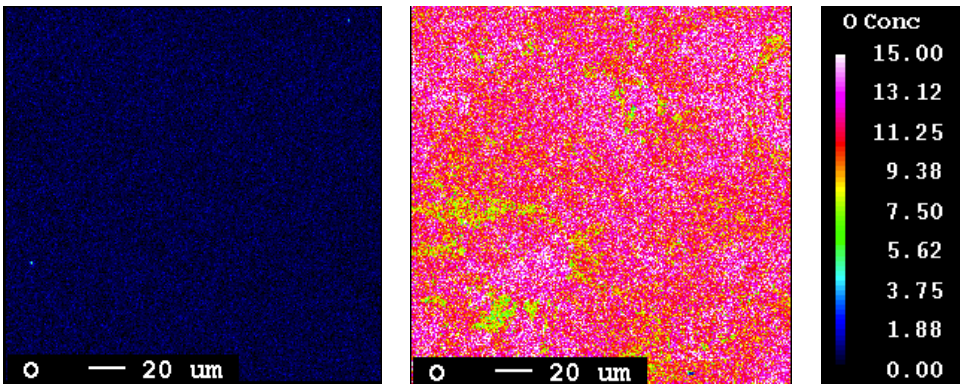

(a) Not contaminated (b) Contaminated (c) Scale bar

Figure 4.13: Oxygen EPMA maps of two areas on the same sample surface (a) without and (b) with contamination. The two maps share the same intensity scale.

4.4 Pressure Development

During heating of the steel sample the pressure increased in the SEM vacuum chamber. The pressure plot throughout a typical in situ H/Q experiment is given in figure 4.14. The first peak is due to the sample heating, while the second peak corresponds to the sample being quenched.

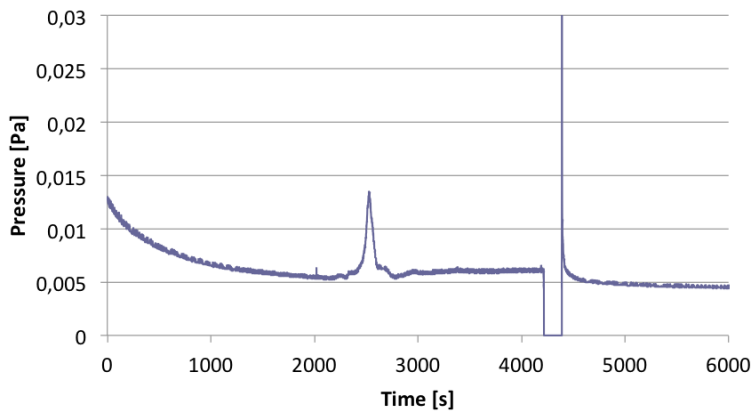

Figure 4.14: The pressure development inside the SEM during a in situ H/Q experiment.

4.5 Stage Temperature

In order not to damage the SEM stage components the temperature between the heating stage and the SEM stage was carefully monitored during all in situ H/Q experiments. Figure 4.15 shows a plot of the stage temperature during a typical in situ H/Q experiment.

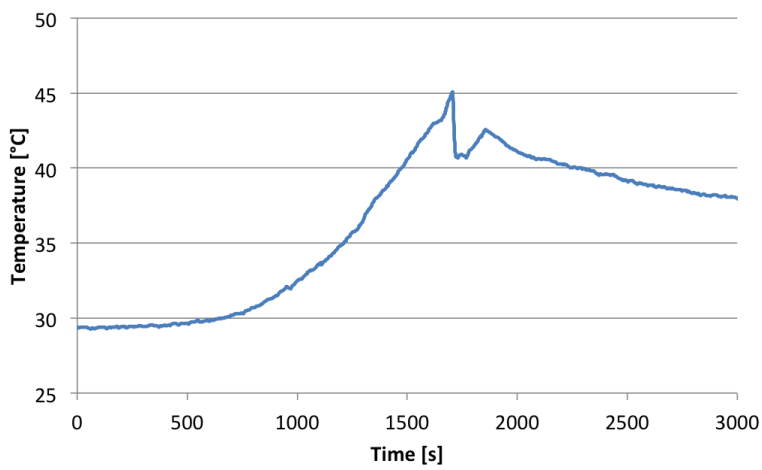

Figure 4.15: The stage temperature at the connection to the SEM during an in situ H/Q experiment.

4.6 In Situ H/Q Experiments

The following section presents in situ H/Q experiments performed on the API X70 steel. Thermal parameters for each sample are given in table 4.6. The high temperature holding time in each experiment were between 10 and 15 minutes for all samples. In situ sample 1 was from the first batch of machined samples. Hence the measured temperature had a deviation from the true sample temperature between 50°C and 100°C, giving true sample temperature somewhere between 790°C and 840°C. In situ sample 2 and 3 had a deviation of about 20°C, giving a true sample temperature of approximately 835°C and 880°C, respectively.

The IPF and phase maps from the EBSD scans have been cleaned according to the technique described in section 2.5.4. Pixels with a CI-value lower than 0.05 are assumed to be incorrectly indexed and are therefore removed from the maps (appear black). Red and green color in the phase maps represent BCC- and FCC-structure, respectively. More EBSD scans from other in situ H/Q experiments are presented in Appendix D.

Table 4.6: Temperature measurements and cooling rates in each of the in situ experiments presented.

Sample	$T_{furnace}$	T_{sample}	$\Delta t_{6/4}$
In situ sample 1	850°C	744°C	6.3 s
In situ sample 2	935°C	813°C	6.4 s
In situ sample 3	880°C	860°C	6.4 s

4.6.1 In situ sample 1

Figure 4.16 shows the EBSD scans from an in situ H/Q experiment, including IPF-maps, phase maps and IQ-maps. The fraction of pixels with a CI value lower than 0.05 is given in table 4.7 in addition to the amount of austenite detected in each scan.

Figure 4.17a shows the 24 theoretical BCC-variants of a cube oriented austenite crystal plotted in a standard {100} pole projection figure. In figure 4.17b the scan of the heated sample is rotated to the same cube orientation to be able to directly compare the BCC-variants observed.

Two crops were made, indicated in figure 4.16e, and shown in figure 4.18 and 4.20. All the phase maps in the two crops include grain boundaries indicated with the color turquoise, blue and black, representing a missorientation of $0° - 15°$, $15° - 50°$ and $50° - 180°$, respectively.

Selected diffraction patterns in crop 1 were exported from the off-line pattern file made by the NORDIF Software, using an algorithm developed by Martin B. Mathisen. Figure 4.19 gives the position from where the diffraction patterns were acquired and compares the patterns across a grain boundary at three different locations. The comparison was done in order to clarify the nature of the dark spots emerging at the grain boundaries in the IQ-map during heating.

Table 4.7: Fraction of points assumed to be incorrect indexed (CI<0.05) and fraction austenite in the scans presented in figure 4.16.

Sample	*Fraction CI<0.05*	*Fraction austenite*
Before heating	0.065	0.005
Heated sample	0.029	0.033
After quenching	0.028	0.004

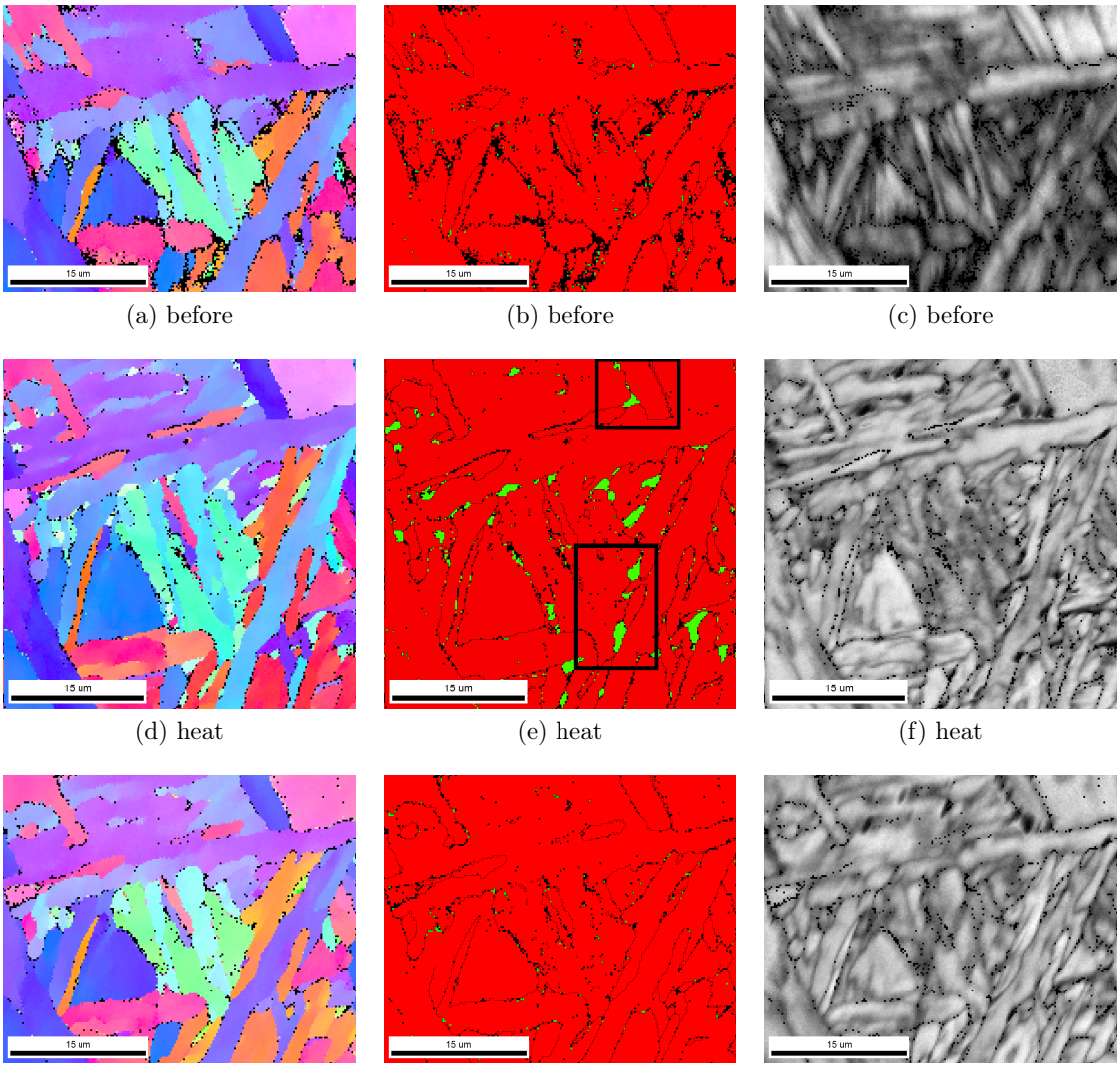

(a) before (b) before (c) before

(d) heat (e) heat (f) heat

(g) after (h) after (i) after

Figure 4.16: In situ sample 1: EBSD scans showing ipf-maps in (a), (d) and (g), phase maps in (b), (e) and (h) and IQ-maps in (c), (f) and (i).

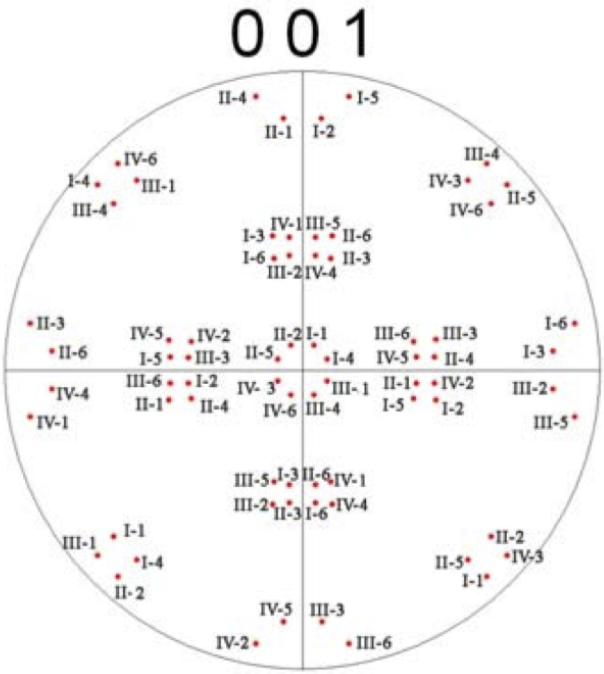

(a) Theoretical K-S relationship

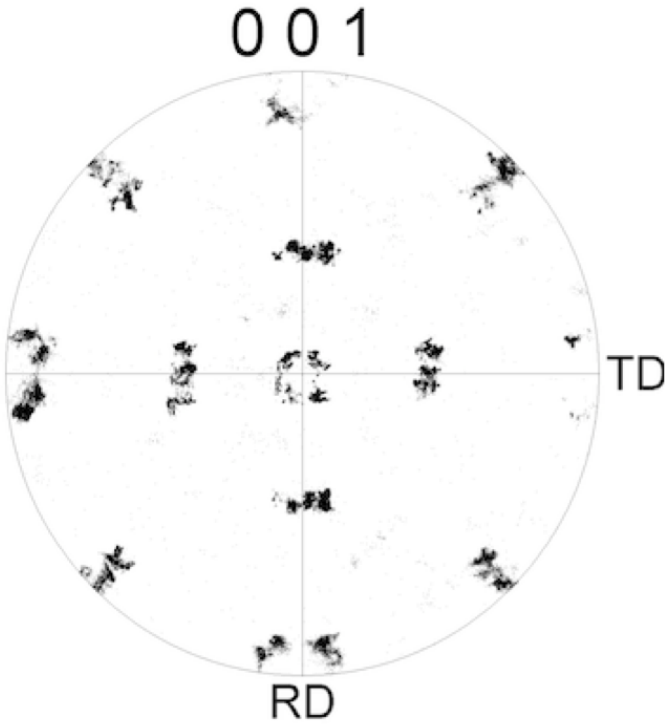

(b) Observed orientation relationship

Figure 4.17: In situ sample 1: Standard {100} pole projections of (a) the 24 possible K-S martensite variants originating from a single (001)[100] austenite orientation [16] and (b) a rotated data set of variants observed in the heated in situ sample 1.

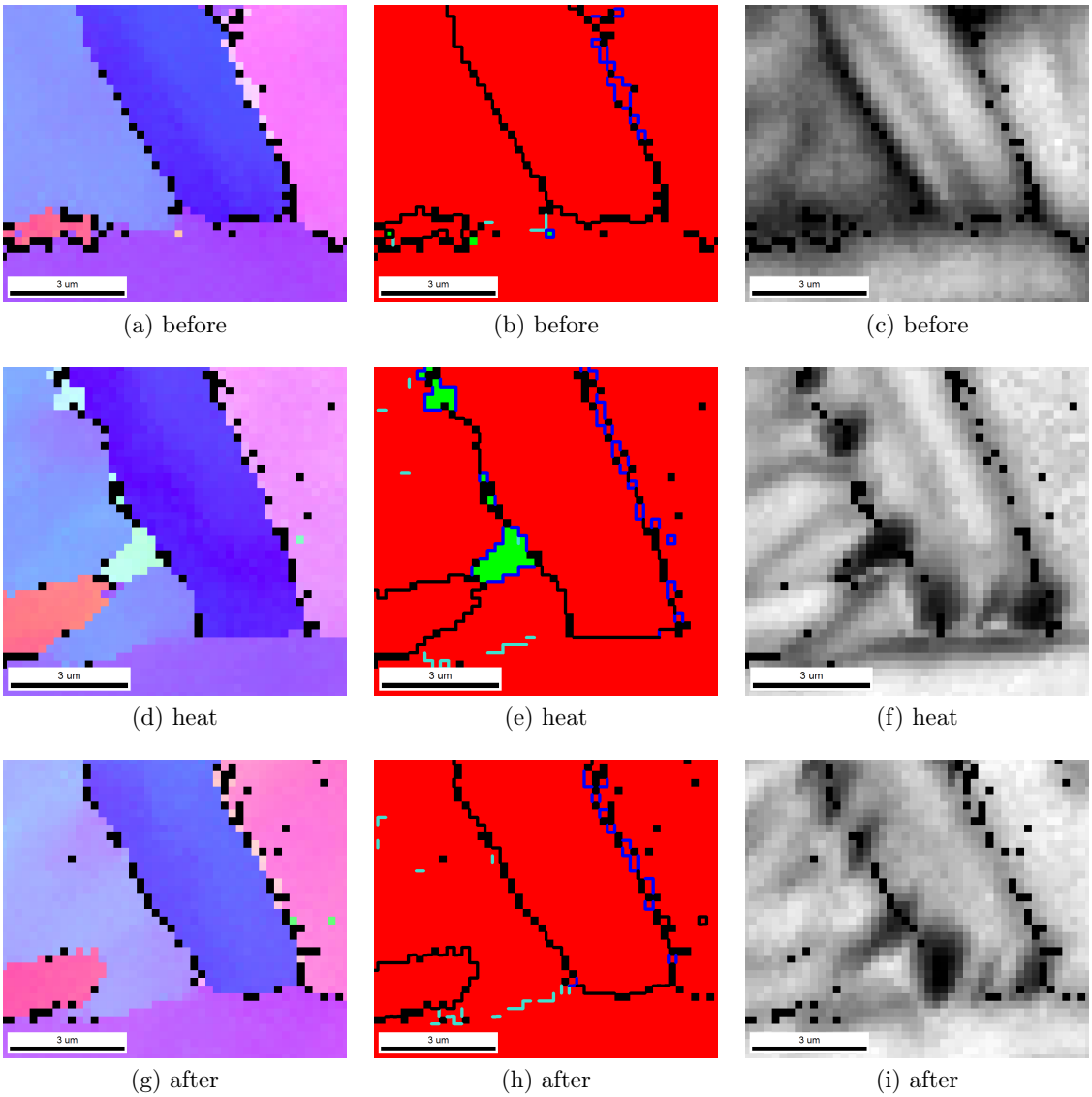

(a) before (b) before (c) before

(d) heat (e) heat (f) heat

(g) after (h) after (i) after

Figure 4.18: In situ sample 1: Crop 1.

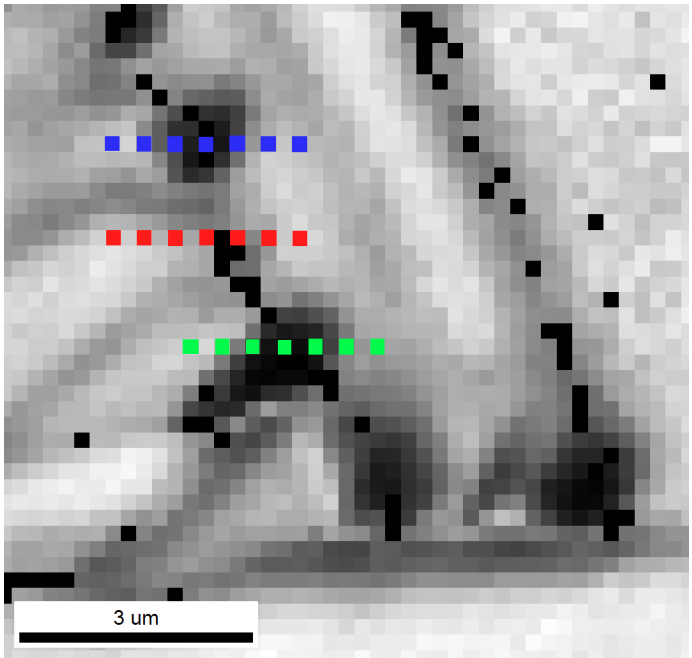

(a) The IQ-map crop from figure 4.18e

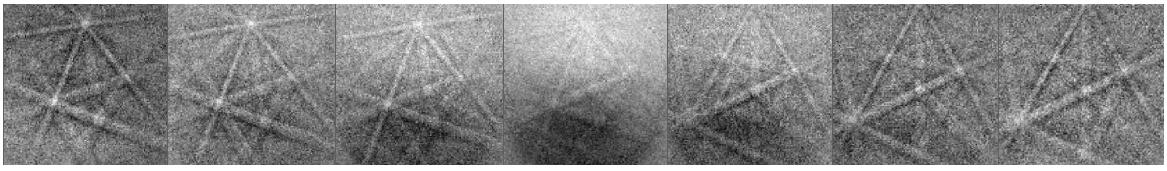

(b) (c) (d) (e) (f) (g) (h)

(i) (j) (k) (l) (m) (n) (o)

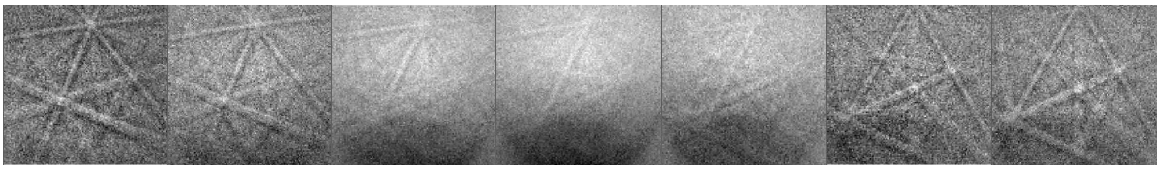

(p) (q) (r) (s) (t) (u) (v)

Figure 4.19: In situ sample 1: The cropped IQ-map from figure 4.18f including blue, red and green dotted lines crossing the grain boundary at different locations. The diffraction patterns recorded along the blue, red and green line are shown in (b) through (h), (c) through (o) and (p) through (v), respectively.

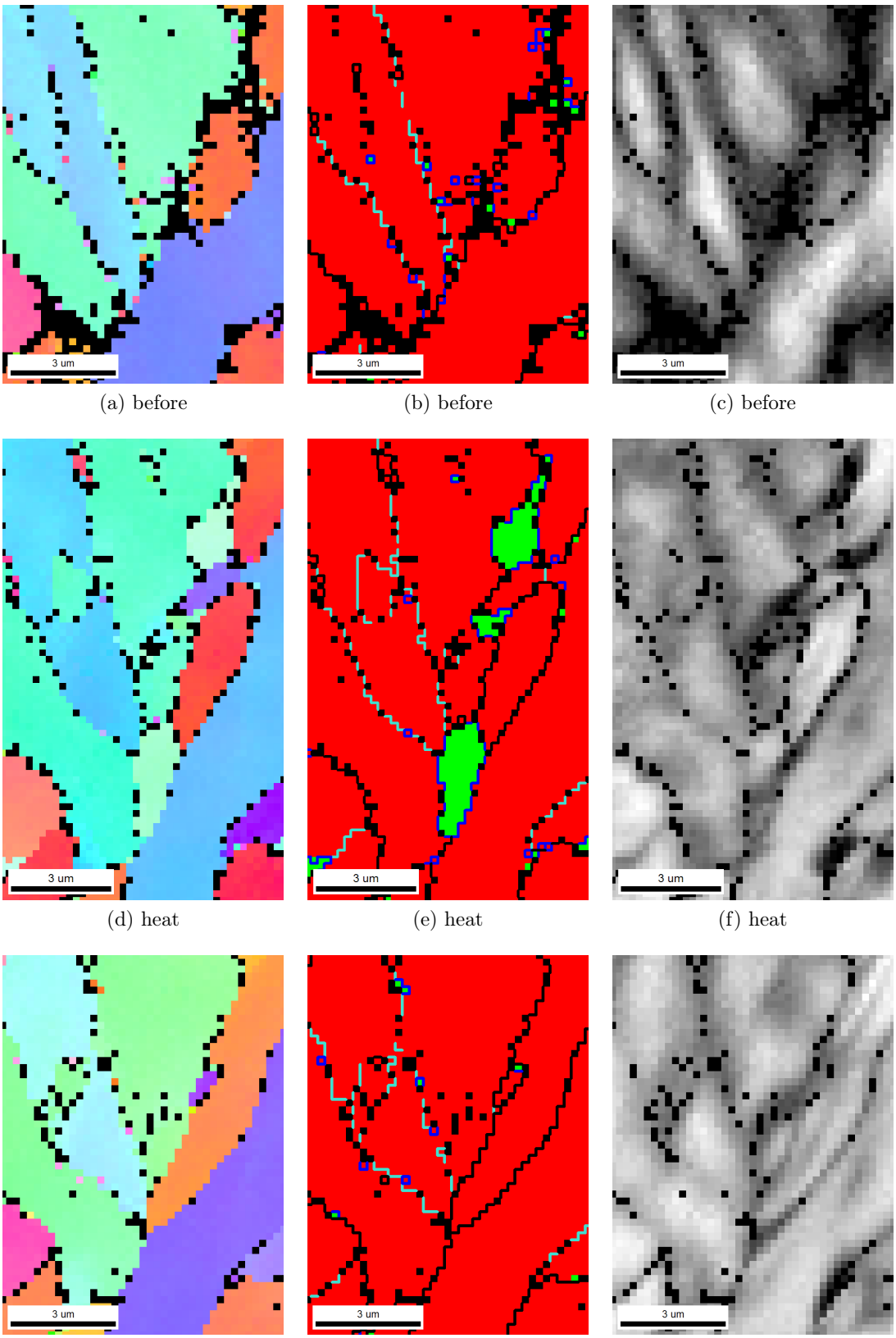

(a) before (b) before (c) before

(d) heat (e) heat (f) heat

(g) after (h) after (i) after

Figure 4.20: In situ sample 1: Crop 2.

4.6.2 Appearance of Diffraction Patterns

Figure 4.21 shows representative diffraction patterns of the same area before heating, at elevated temperature and after cooling. The patterns are all recorded from in situ sample 1 with 160x160 pixels (3x3 binning) and a exposure time of 6617μs. The background is subtracted for each pattern.

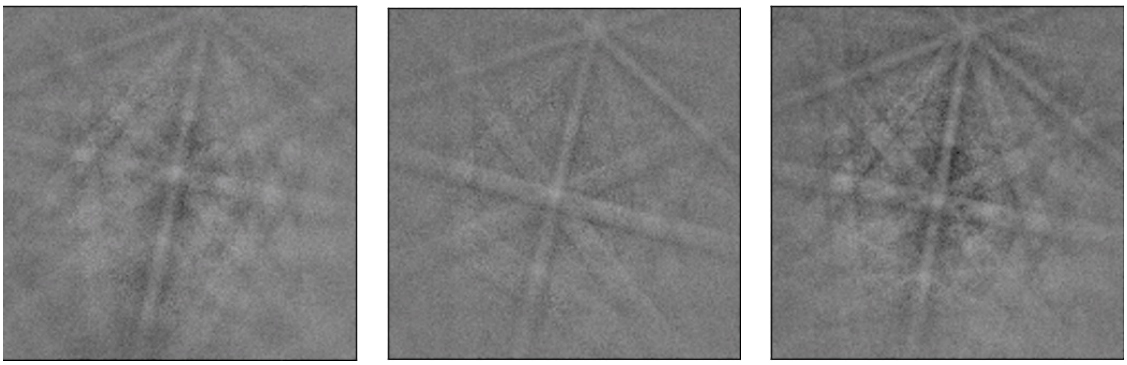

(a) Before heating (b) At 800 °C (c) After cooling

Figure 4.21: The diffraction patterns for the same surface area (a) before heating, (b) at 800°C and (c) after cooling.

4.6.3 In situ sample 2

Figure 4.22 shows an inverse pole figure (IPF) map of the API X70 steel as received after first weld cycle simulation. The selected area includes what appears to be a former austenite grain boundary and was in situ EBSD characterized during a H/Q experiment, shown in figure 4.23. The scans are done before heating, at elevated temperature and after quenching. The fraction of pixels with a CI value lower than 0.05 is given in table 4.8 in addition to the amount of austenite detected in each scan. Formation of austenite was detected in two areas of the scan done at elevated temperature. These are cropped and shown in figure 4.24 and 4.26. All the phase maps in the two crops include grain boundaries indicated with the color turquoise, blue and black, representing a missorientation of $0° - 15°$, $15° - 50°$ and $50° - 180°$, respectively.

For the first crop the orientation relationship between the austenite (FCC) and the surrounding BCC-structure is compared with the K-S relationship explained in section 2.3. The scan is rotated to the same cube orientation as the pole figure showing the 24 theoretical BCC-variants in figure 2.4. This makes it possible to directly compare the BCC-variants observed.

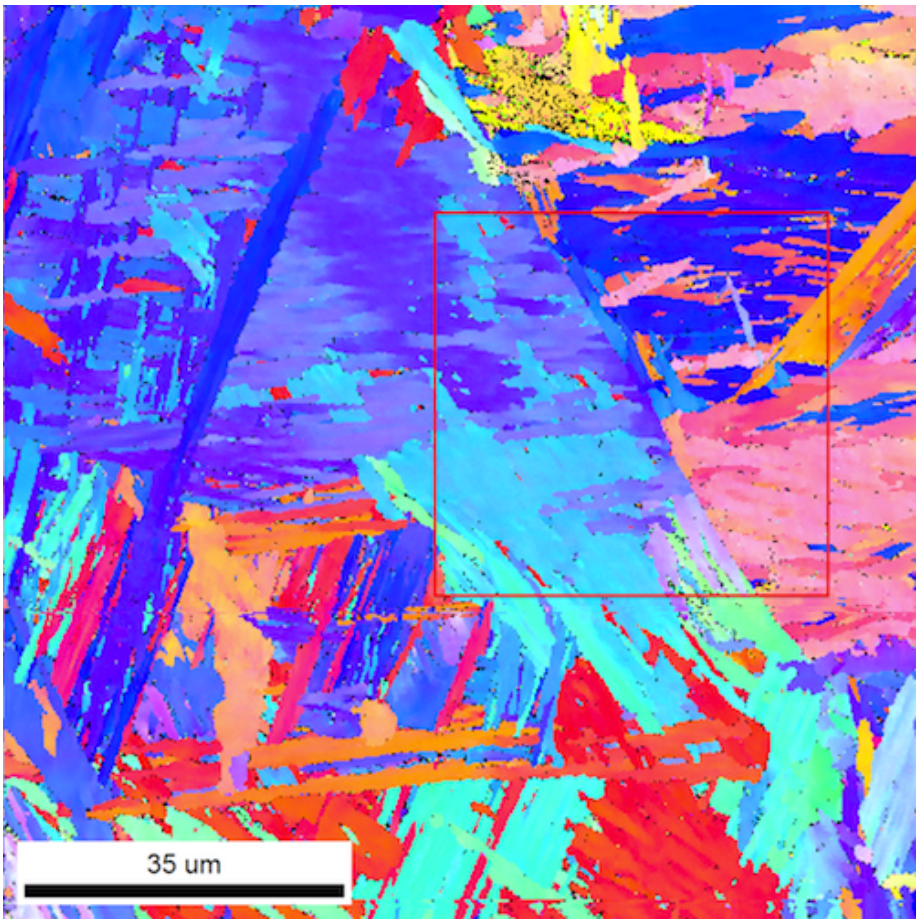

Figure 4.22: IPF map of the X70 steel before second cycle heating. The selected area are cropped and is shown in figure 4.23.

Table 4.8: Fraction of points assumed to be incorrect indexed (CI<0.05) and fraction austenite in the scans presented in figure 4.23.

EBSD-scan	*Fraction CI<0.05*	*Fraction austenite*
Before heating	0.014	0.002
Heated sample	0.019	0.015
After quenching	0.008	0.003

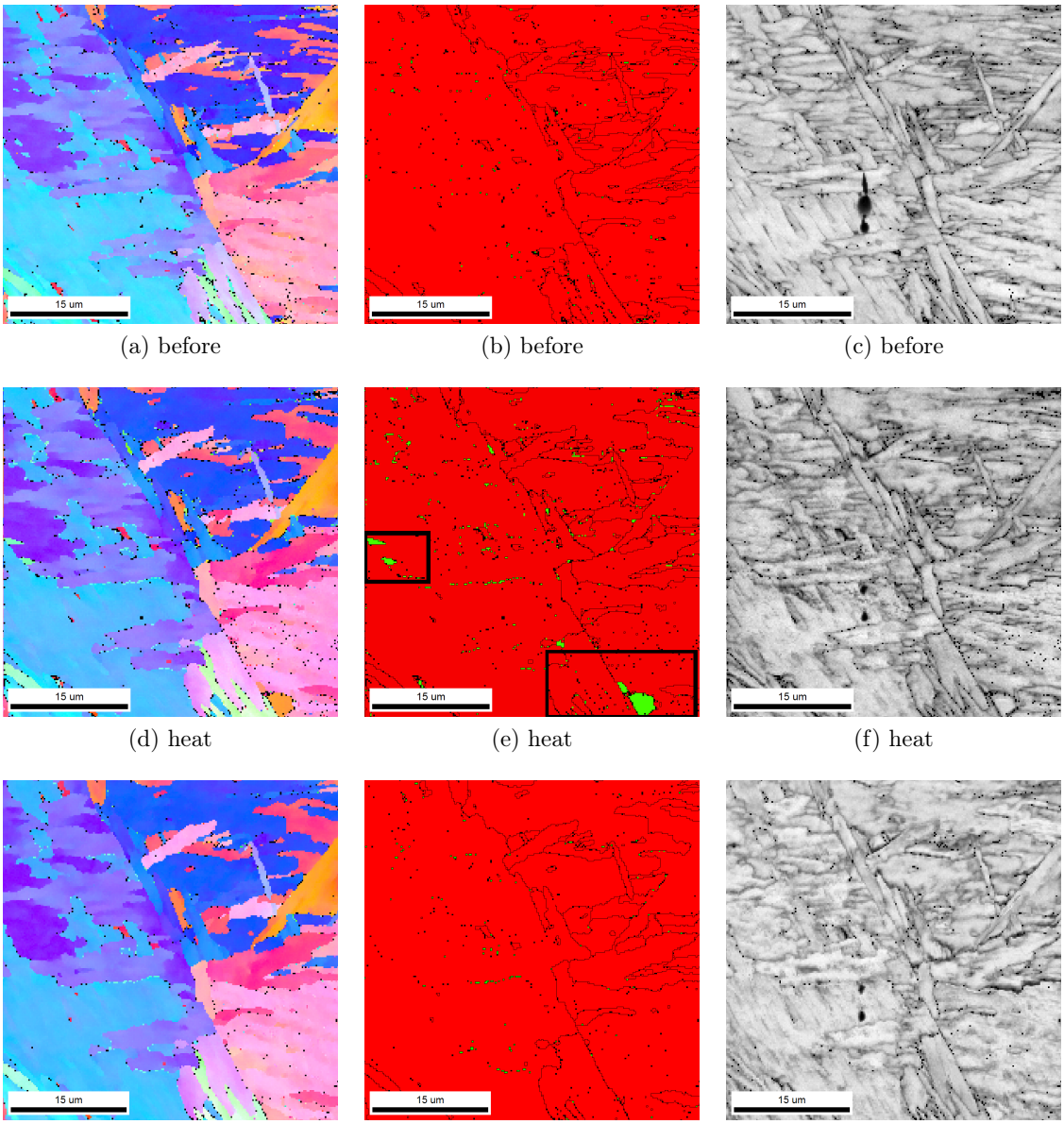

(a) before (b) before (c) before

(d) heat (e) heat (f) heat

(g) after (h) after (i) after

Figure 4.23: In situ sample 2: EBSD scans showing ipf-maps in (a), (d) and (g), phase maps in (b), (e) and (h) and IQ-maps in (c), (f) and (i).

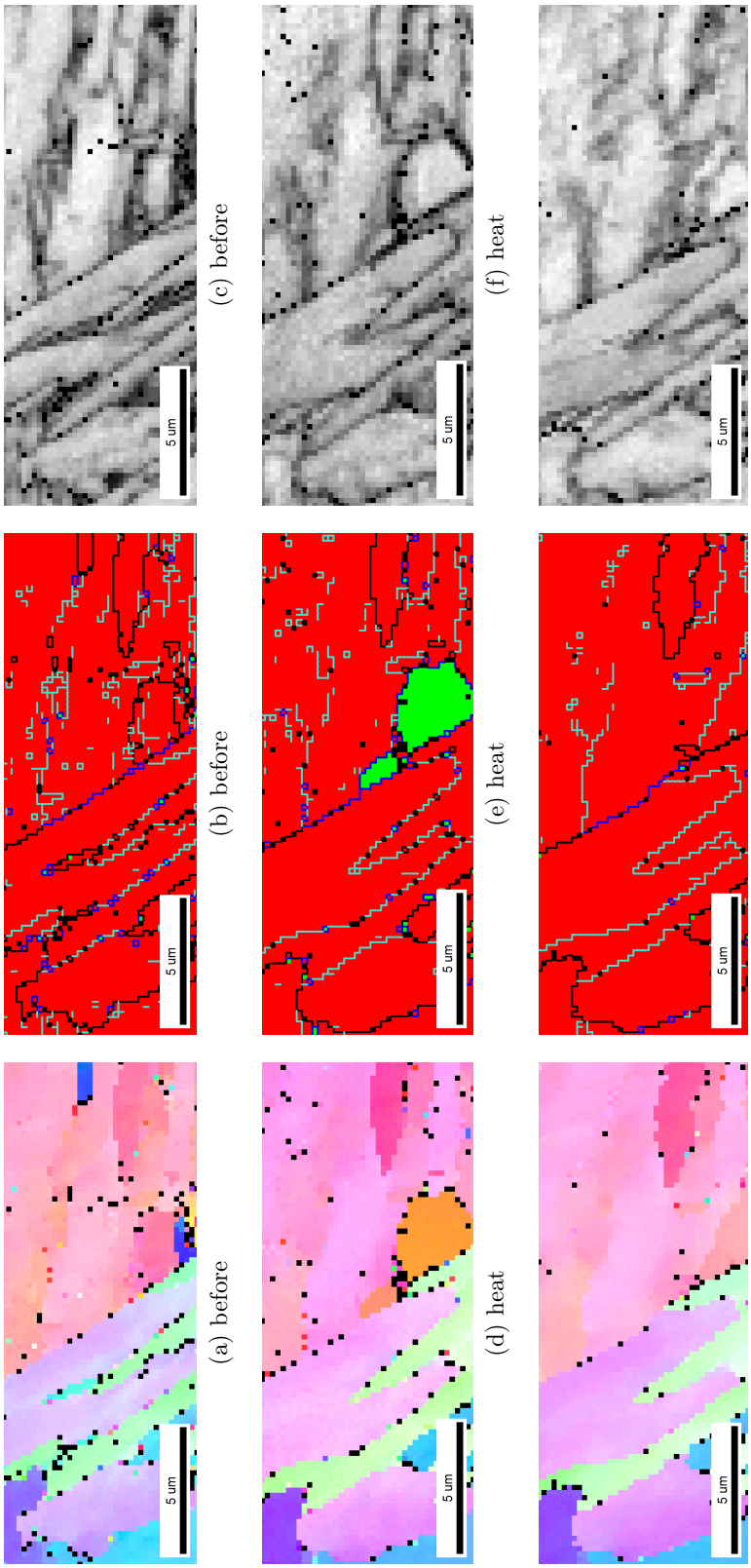

(a) before (b) before (c) before

(d) heat (e) heat (f) heat

(g) after (h) after (i) after

Figure 4.24: In situ sample 2: Crop 1.

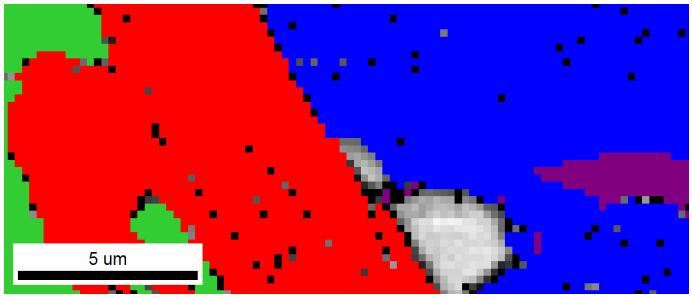

(a) The cropped IQ-map in figure 4.24f colored according to the pole figures below

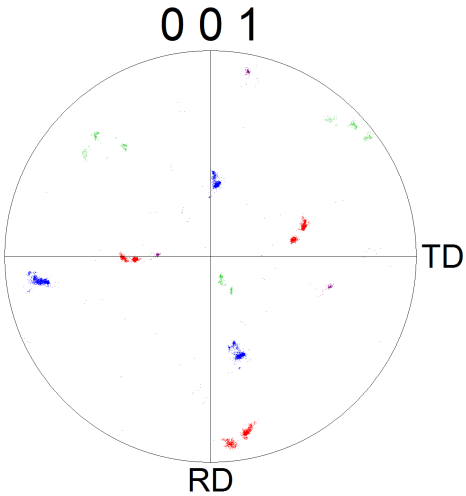

(b) The orientation relationship between FCC and the surrounding BCC expressed in a pole figure

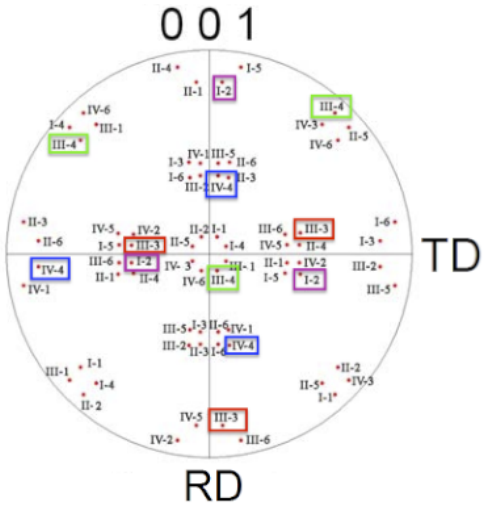

(c) The theoretical K-S relationship with highlighting of the orientations found in (b)

Figure 4.25: Orientation relationship between FCC and BCC in the heated scan of in situ sample 2, crop 1.

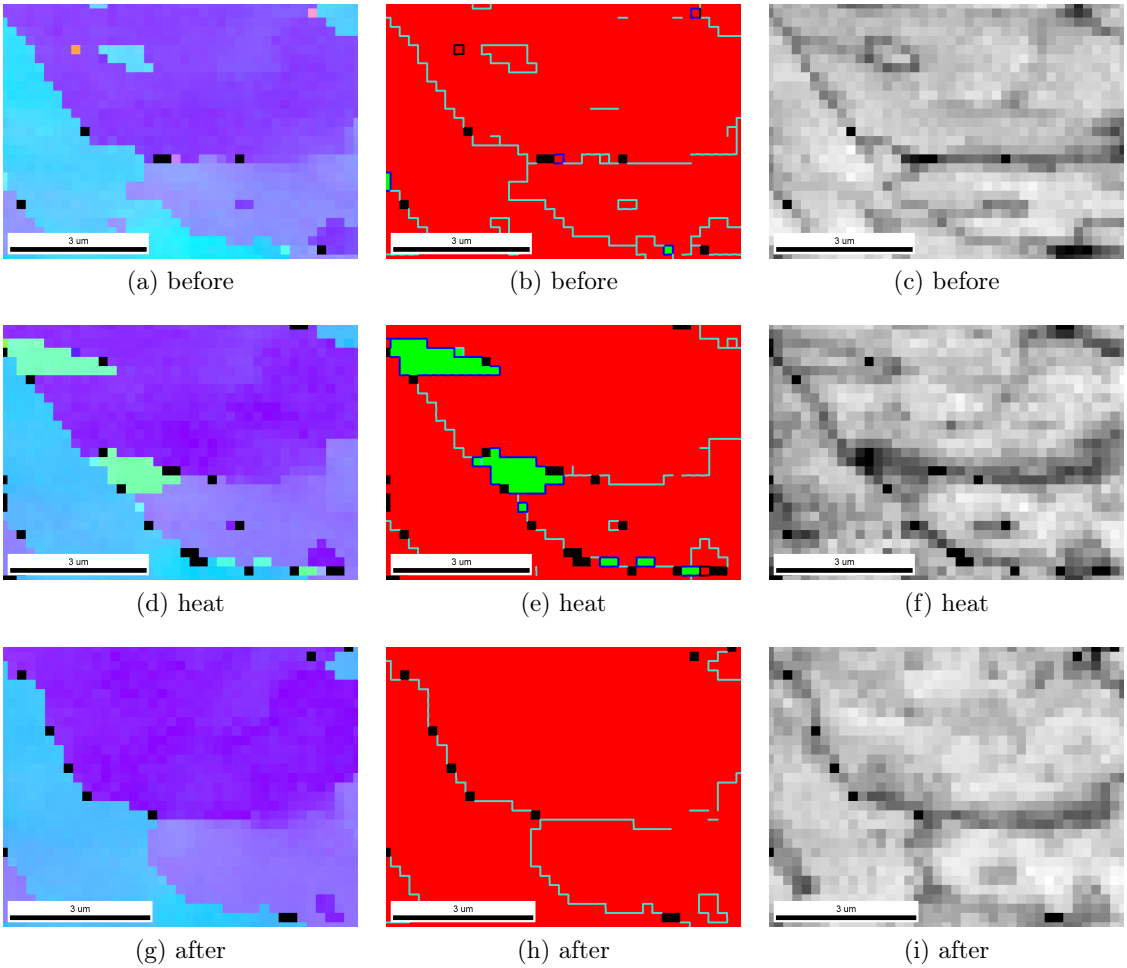

(a) before (b) before (c) before

(d) heat (e) heat (f) heat

(g) after (h) after (i) after

Figure 4.26: In situ sample 2: Crop 2.

4.6.4 In situ sample 3

Figure 4.27 shows the EBSD scans from an in situ H/Q experiment, including IPF-maps, phase maps and IQ-maps. The fraction of pixels with a CI value lower than 0.05 is given in table 4.9 in addition to the amount of austenite detected in each scan. The selected area in figure 4.27h is cropped and given as an IQ-map in figure 4.28 together with the compared inverse pole figures of the observed BCC-FCC orientation relationship and the theoretical K-S relationship.

Table 4.9: Fraction of points assumed to be incorrect indexed (CI<0.05) and fraction austenite in the scans presented in figure 4.27

Sample	*Fraction CI<0.05*	*Fraction austenite*
Before heating	0.026	0.003
Heated sample	0.047	0.372
After quenching	0.290	0.188

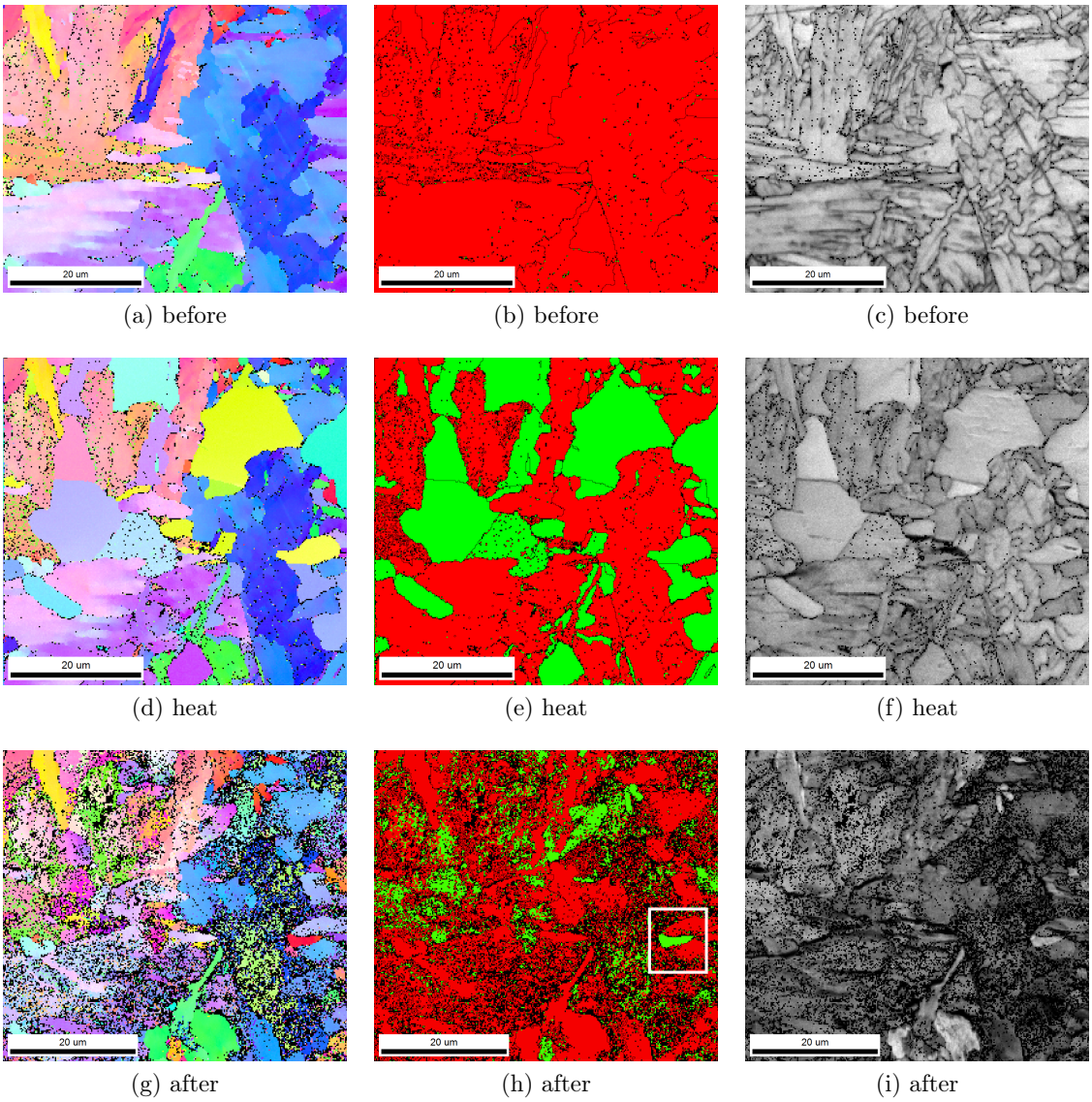

(a) before (b) before (c) before

(d) heat (e) heat (f) heat

(g) after (h) after (i) after

Figure 4.27: In situ sample 3: EBSD scans showing ipf-maps in (a), (d) and (g), phase maps in (b), (e) and (h) and IQ-maps in (c), (f) and (i).

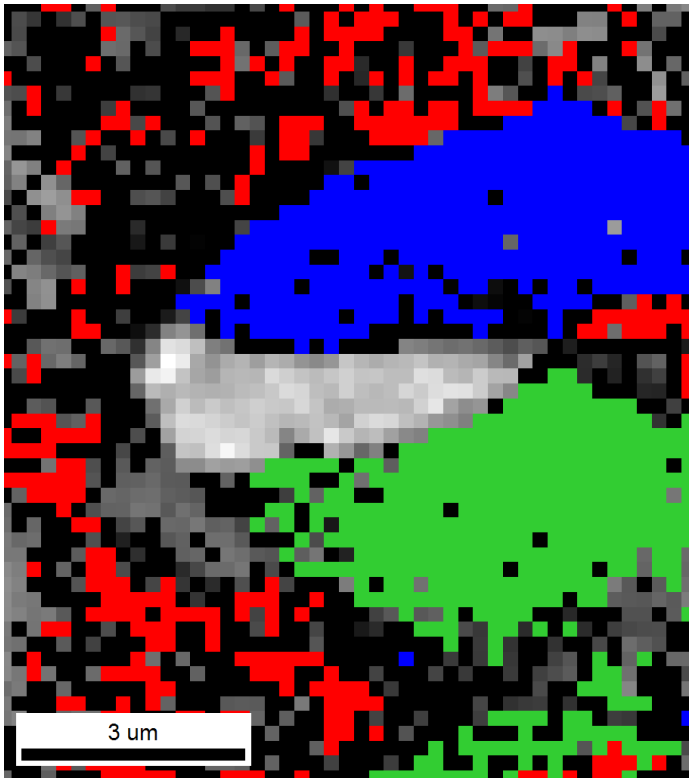

(a) The cropped IQ-map from figure 4.27i colored according to the pole figures below

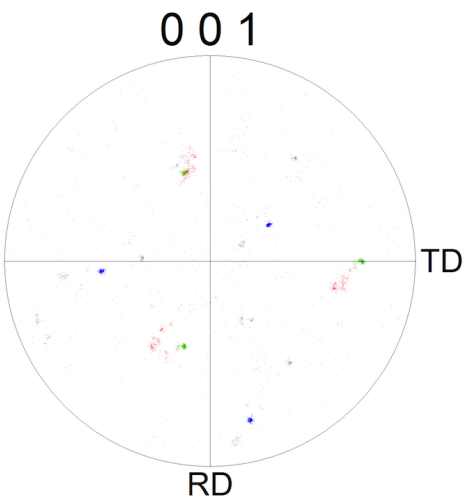

(b) The orientation relationship between FCC and the surrounding BCC expressed in a pole figure

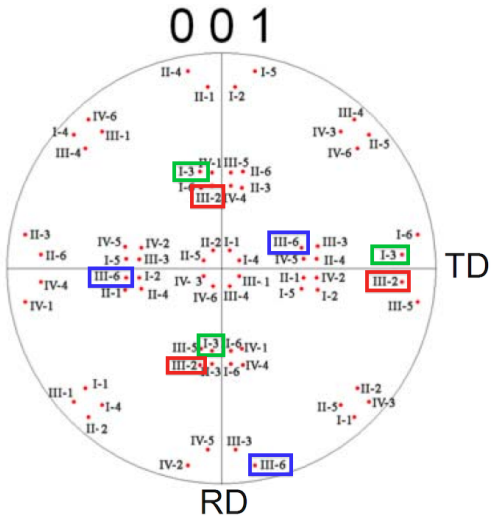

(c) The theoretical K-S relationship with highlighting of the orientations found in (b)

Figure 4.28: Orientation relationship between FCC and BCC in the heated scan of in situ sample 3 (cropped).

Chapter 5

Discussion

5.1 The in situ H/Q-device

A main goal throughout this master thesis has been to develop a system for heating and quenching (H/Q) of a steel sample combined with EBSD-characterization in situ a scanning electron microscope (SEM). As a result this technique the undesirable phases that are formed in the heat affected zone (HAZ) during welding, such as the MA-phases, and their formation, can be better understood.

5.1.1 The cooling rates

The preliminary tests performed in the experimental vacuum chamber were important in order to see the potential of the different cooling methods. Gas as a cooling media gave the most promising results, and further investigation showed a great difference in the cooling ability of argon and helium (figure 4.3a). Table 2.1 shows that helium has a 10 times higher heat capacity and an 8 times higher heat conductivity compared to argon, both properties important in the convective heat transfer equation (equation 2.9).

The SEM was modified to allow high purity helium gas throughout a nozzle directly onto the steel sample surface during ventilation. Figure 4.3b shows comparable cooling curves between a traditional thermal weld simulation test with a cooling time between 800°C and 500°C ($\Delta t_{8/5}$) of 5 seconds, and of a gas quenched steel sample inside the SEM. The curves in figure 4.3b proves that gas quenching is a suitable technique for obtaining small scale rapid cooling experiments inside a SEM.

5.1.2 Temperature Control

During the in situ H/Q experiments performed in this master thesis it was essential to measure the correct steel sample temperature in order to simulate the inter critical coarse grain part of the heat affected zone (ICCGHAZ). As mentioned in section 2.2 the second weld cycle must reach a peak temperature within the Ac_1-Ac_3-interval (two-phase (α+γ)).

Section 2.1 mentions that the Ac_3 temperature is highly dependent on the heating rate and thus the Ac_1-Ac_3-interval gets very narrow during a slow heating. This relationship can be seen in figure 4.1 and 4.2 where the Ac_1-Ac_3-interval decreases from 160°C to 60°C with a heating rate reduction from 6000°C/min to 5°C/min, respectively. During the in situ H/Q experiments a heating rate of 60°C/min was used, which narrowed down the temperature interval and made it more difficult to reach within the two-phase (α+γ) region.

Thermal transition in high vacuum represented an important challenge in the in situ H/Q experiments. From earlier experiments [19] it was obvious that a high cooling rate could not be achieved by putting a cold finger into contact with the hot steel sample. The same issues arose within the area of temperature measurements. During an in situ H/Q experiment two thin thermocouples are fitted into small holes in the furnace and in the steel sample, respectively. The furnace thermocouple controls the power supply while the sample thermocouple gives a more correct indication of the steel temperature.

In the first batch of machined steel samples the thermocouple holes were spark eroded to a size of 0.52 mm, equal to that of the thermocouple, resulting in a tight but shallow penetration. The temperature curves in figure 4.4a show that the true steel sample temperature is halfway between the measured furnace temperature ($T_{furnace}$) and the measured sample temperature (T_{sample}). The additional temperature measurements presented in appendix C shows a similar relationship, however the measured error is not equal in every test. The measured difference between $T_{furnace}$ and T_{sample} varies from 70°C to 170°C. This implies that the deviation between $T_{furnace}$ and T_{sample} is a result of several different parameters, most of them difficult to control.

The deviation between $T_{furnace}$ and the true steel sample temperature is due to environmental heat loss and poor heat transfer between the thermocouple an the furnace and the furnace and sample. The latter is dependent on the amount of platinum paint used. The deviation between T_{sample} and the true sample temperature is on the other hand totally dependent on poor heat transition between the thermocouple and the sample.

By increasing the size of the thermocouple hole in the the second batch of machined samples to 0.60 mm the thermocouple could penetrate deeper into the sample and thus measure a more correct temperature. From figure 4.4b it is obvious that a smaller thermal barrier has been achieved as a result of the new samples. The measurement error of the sample was reduced to 20°C in the second batch. No repeatability tests of this result were performed.

5.1.3 Resulting Mirostructure

In order to verify the in situ H/Q system the resulting microstructure of a second cycle in situ H/Q experiment was compared with the microstructure from a traditional two-cycle thermal weld simulation (TWS). Sample 17 and 18 were second cycle weld simulated with a target peak temperature of 780°C.

The light microscope images in figure 4.6 show that the second cycle TWS has covered the former austenite grain boundaries with finely dispersed dark grains. Similar small

grains are observed in the IPF-maps in figure 4.7. The description match the expected MA-phases explained in section 2.2. The phase maps in figure 4.8 show that none of the new grains are indexed as residual austenite. However, in the IQ-maps they appear darker than the surrounding structure. This indicates a lower band contrast, which may be a result of high stress in the lattice structure. It is therefore likely that most of the austenite formed during second cycle TWS have transformed into brittle martensite with high dislocation density.

According to the dilatometer plot in figure 4.2 the Ac_1-temperature was found to be higher than 780°C. In order to increase the amount of MA-phases in the steel an additional TWS was done with a target peak temperature of 815°C. No obvious variations were observed in the light microscope, or from the EBSD-scans. The MA-phases did not become more extensive and they still appeared dark in the IQ-map. It is important to point out that the IQ-maps are based on qualitative values, and that the greyscale only can be compared within the same map.

These characteristic MA-phases are not found in the in situ H/Q samples. The structure is much more interconnected than the other samples, which makes it difficult to observe any form of former austenite grain boundaries in the light microscope. No residual austenite is found in phase map, and unlike the TWS samples does the in situ H/Q sample not show any dark spots on the grain boundaries in the IQ-map.

The appearance of the MA-phases in the TWS samples can be explained by the rapid heating of the steel. When the sample reaches the two-phase (α+γ) region the high heating rate leads to a high nucleation frequency and thus the formation of finely dispersed austenite grains on and near the former austenite grain boundaries. The immediate quenching provokes a phase transformation from austenite into martensite. The in situ H/Q samples, on the other hand, has a one hundred times lower heating rate and therefore also a lower austenite nucleation frequency. The slow heating rate may allow a few nucleated austenite grains to grow bigger rather than allowing nucleation of new austenite grains. At maximum power the in situ heating system managed to heat the sample from 70°C to 770°C with an average heating rate of 5.5°C/s. The heating curve is plotted in figure 5.1 and compared with the heating curves of a normal in situ experiment and a traditional TWS. This heating rate may be enough to increase the nucleation frequency and therefore also obtain a microstructure more similar to the TWS sample. On the other hand, with a higher heating rate it may take longer to stabilize the thermal expansion and the holding time may have to be increased.

The effect of the holding time during in situ H/Q experiments is unknown, but it seems to lead to heavy tempering of the martensite. The microstructure in general has become more coarse compared to the microstructure after one cycle TWS. This may be the reason why the former austenite grain boundaries are so difficult to spot during investigation in the light microscope. A consequence of the coarsening is that the structure expands, crosses the former austenite grain boundaries and hence erases them. Tempered martensite is also observed in TWS samples, but here it does not result in erased grain boundaries. This may be due to the absence of holding time. It may also be a result of the partly continuous austenite grains on the former austenite grain boundaries, creating a barrier against the expanding martensite. This coarsening effect is, however, not observed in situ in any of the in situ H/Q experiments.

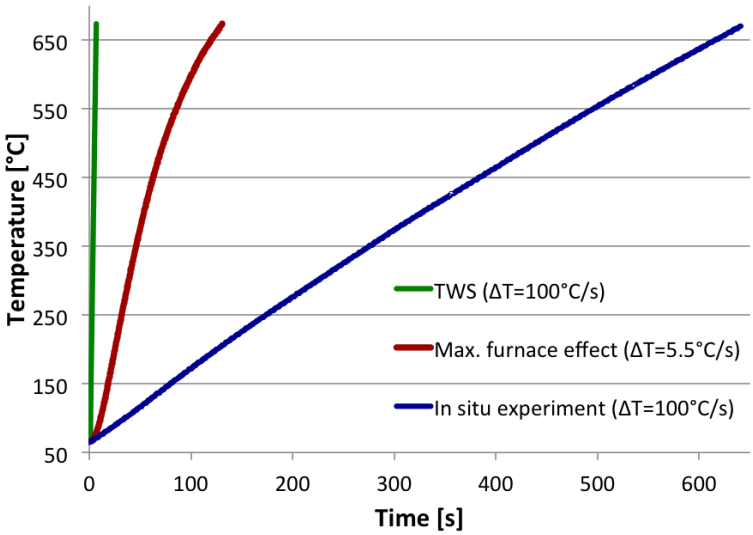

Figure 5.1: The heating curves recorded during a traditional TWS and during a normal in situ experiments compared with the maximum possible heating rate of the in situ heating system.

5.1.4 Contamination

During the first in situ H/Q experiments there were no problems regarding contamination of the sample surface after quenching. Gradually the contamination layer evolved from being slightly noticed to becoming essential for the success of the experiment. At its worst the contamination layer covered the whole sample. The contamination layer resulted in several artifacts in the EBSD-scans. The scans in figure 4.11 show the same surface area before heating and after quenching and suggest a resulting grain orientation completely different from the initial microstructure. The microstructure is, however, the same in the two scans. The diffraction patterns recorded during the last scan indicates an FCC structure covering 80 percent of the steel sample surface, with a surprisingly high average CI-value after removing of unindexed points.

In order to reduce the amount of contamination on the steel samples tests were performed with and without pre-flushing of the quenching system. The tubes, regulators and the valve were flushed for 30 seconds immediately before pumping of the vacuum chamber. No obvious reduction in the amount of contamination were observed due to the pre-flushing.

The EPMA-analysis show a higher concentration of oxygen on the contaminated surface compared to the contamination free surface. None of the other elements show a noticeable deviation in concentration. Due to the detection of oxygen on the sample surface the source is suspected to be either the gas itself or the tube system. The high purity gas used in the experiment has a total impurity amount of less than 1 ppm, and is not believed to be the source. The effect of replacing all the Teflon and plastic tubes with metal tubes should be tested in further work.

It seems like the contamination layer is an oxide with a structure close to that of FCC. It also seems like the oxide microstructure is strongly dependent on the steel surface

microstructure. A given crystallographic orientation on the steel surface gives a specific orientation to the overlaying contamination layer. As a result the microstructure on the sample surface after quenching is very recognizable.

5.1.5 Risks related to the in situ H/Q system

During this master thesis the Zeiss Gemini Ultra 55 Limited Edition SEM was modified in order to be used in the in situ H/Q experiments. These modifications led to a higher risk of damaging sensitive equipment during operation.

The installation of a heating stage represents a risk of overheating the fine mechanics that controls the SEM stage. To reduce this risk the stage temperature was carefully monitored and not allowed to exceed 47°C. The stage temperature plot in figure 4.15 shows that the stage temperature is kept within the safety limit during an in situ H/Q experiment.

Another risk based on the heating of the sample can be observed in the pressure development during an in situ H/Q experiment. The first peak in the pressure plot in figure 4.14 is a direct consequence of the heating of the steel sample. The vacuum loss is believed to be due to evaporation of the residual solvent in the platinum paint. The vacuum loss occurred despite that every sample dried for two hours inside an incubator at a temperature of 75°C. A longer time inside the incubator did not lead to a lower vacuum drop during in situ H/Q experiments.

The quenching itself involved a high risk of damaging the molecular vacuum pump inside the SEM. In addition the EDS detector has a fragile thin protective window which is sensible to rapid pressure changes. By adjusting the gas inlet equal to the maximum designed inlet pressure the risk was minimized.

The backscatter detector and the EDS-detector are located close to the heating stage and the quenching rig during experiments and were thus removed to rule out the risk of impact damages and also the risk of overheating and uncontrolled gas flow.

5.2 In Situ Experiments

As previously discussed in section 5.1.2 the in situ H/Q experiments presented in this master thesis were done without exact temperature measurements. Therefore a peak temperature within the two-phase ($\alpha+\gamma$) region was achieved through trial and error. Scan D.5 and D.6 are both examples of in situ H/Q experiments where the austenite formation during heating was either extremely small or not present. This was probably due to a too low peak temperature or local variations in the microstructure. All the samples presented in the results chapter formed austenite during heating, and thus reached a temperature within the two-phase region. If temperature measurements in table 4.6 are adjusted to the measurement errors found for batch 1 and batch 2 there is a tendency of increased amount of detected austenite at increased peak temperatures. This is also expected from the phase diagram in figure 2.1.

In in situ sample 1, all the austenite islands share the same crystallographic orientation, which indicates that the EBSD characterized area is inside the same former austenite grain. The match between the observed FCC-BCC orientation relationship and the K-S relationship in figure 4.17 proves that the austenite is correctly indexed. More or less all the 24 possible Kurdjumov-Sachs BCC variants originating from the one austenite orientation is found in the EBSD-scan.

According to the IPF-maps the austenite formed during heating in in situ scan 2 and 3 have two or more different crystallographic orientations within the scanned area. The two austenite islands in in situ sample 2 do not share the same crystallographic orientation, and is probably located inside their respective former austenite grain. This is supported by what appears to be a former austenite grain boundary cutting through the scan diagonal and separating the two austenite islands. One of these islands has nucleated on the former austenite grain boundary. It was therefore of interest to examine the orientation relationship between this austenite island and the surrounding BCC-structure. Figure 4.25 shows a K-S relationship between the austenite and the surrounding BCC on both sides of the former austenite grain boundary. The fact that the austenite phase can be related to both the former austenite grains may indicate a twin grain boundary. One can also question the existence of the former austenite grain boundary. The high amount of austenite that forms in in situ sample 3 have no less than 10 different crystallographic orientations. Some of these austenite grains even have their own grain boundaries within the grains. No obvious correlation between the new and the former austenite grain boundaries is observed. The explanation for this has not been found and remains unknown to the author.

Both the cropped scans of in situ sample 1 shows that the austenite nucleates on high angle grain boundaries or at triple points. This is also observed in the first crop of in situ sample 2. However, the austenite formed inside the former austenite grain in crop 2 nucleated from low angle grain boundaries with a missorientation angle lower than 15°. The nucleation of this austenite may be due to the presence of other nucleation cites such as particles etc. It may also be a result of the slow heating rate discussed in section 5.1.3.

According to the Fe-C phase diagram presented in figure 2.1 should a heat treatment of HSLA-steel into the lower parts of the two-phase (α-γ) region result in small amounts of carbon rich austenite. Due to locally high carbon content a rapid quenching should lead to retained austenite or high strain martensite. Usually retained austenite is easy to observe in the phase maps, whereas dislocation dense martensite should be possible to distinguish in the IQ-maps in the form of local darker areas. Despite the high cooling rate, neither residual austenite nor martensite are observed in in situ sample 1 or 2 after quenching. One explanation may be surface evaporation of carbon during the high temperature holding time, as discovered by A.-J. Enstad [28]. However, the holding time after scanning is insignificant compared to the holding time prior to the EBSD-scan. Therefore there should be no significant reduction in the austenite amount between the scan and the quenching. Another explanation may be insufficient cooling rate during gas quenching, despite the achieved cooling time between 600°C and 400°C, $\Delta t_{6/4}$, of 6.5 seconds.

The retained austenite observed in in situ sample 3 is believed to be an artifact as a result of contamination on the sample surface during quenching. This assumption is supported

by comparing the orientation of the retained austenite with the austenite formed during heating. The resulting crystallographic orientation of the FCC differs from the FCC orientation observed in the heated sample. However, most of the retained austenite is located in the same areas as the austenite that formed during heating, making it more difficult to reject than the retained austenite in figure D.2 and D.6 of appendix D. The retained austenite also shows a K-S relationship with the surrounding BCC-structure. This may be a consequence of the cystallographic correlation between the steel sample surface and the oxide discussed in section 5.1.4.

Some dark spots are observed along the grain boundaries in the IQ-maps, indicating a lower diffraction pattern quality and therefore the possibility of a dislocation dense structure. These dark spots, however, emerge upon heating and cannot be considered as high strain martensite from the rapid cooling. In figure 4.19 the diffraction patterns across one of these dark spots have been loaded from the NORDIF pattern file. The possibility to export a desired pattern from an EBSD-scan is considered to be an important advantage of the off-line EBSD system. The patterns from the blue dotted line show a pattern change when crossing the grain boundary, with overlapping patterns in (e) and (f). The red dotted line shows the same pattern change, but with pattern overlapping only in (m). The green dotted line shows overlapping patterns in (r) through (t). Pattern overlapping in general makes it difficult for the indexing software to choose the correct pattern. Therefore, points along grain boundaries often end up as unindexed. The overlapping patterns are, however, not the reason for the dark spots. The low IQ-values in the dark spots are a result of the low band contrast. The patterns within the dark spots are clearly underexposed in their lower parts. This makes it difficult to adjust the brightness and contrast, and the patterns appear blurry. From figure 4.18 it seems to be a correlation between the appearance of dark spots and the formation of austenite islands. Further investigation questions this statement. Dark spots may appear without austenite and austenite may form without dark spots. Therefore the nature of these dark spots are unknown to the author.

The phase transformations during heating and cooling lead in some cases to a change in the microstructure, whereas in other cases the austenite shows a memory-effect and transforms back to the initial orientation. The former is observed in the first crop of sample 2 (figure 4.24) and partly in the second crop of sample 1 (figure 4.20). In the first case the austenite nucleates on a high angle grain boundary and consumes a small grain with a high missorientation to the surrounding structure (The limitations of using the simplified inverse pole figure to express the crystallographic orientation of a grain are here demonstrated. Despite a mismatch higher than 50° the IPF shows a close color correlation.). After the quenching the austenite has transformed and adapted the orientation of the surrounding structure. In the second case the austenite emerge from the intersection point of three high angle grain boundaries. It seems like the austenite island grows at the expense of all the surrounding grains except the one with an orientation represented by the color orange. However, during quenching most of the austenite transforms and adapts the orange orientation. The first crop of sample 1 (figure 4.18) and the second crop of sample 2 (figure 4.26) are both examples of austenite that show a memory-effect and transforms back to the initial crystallographic orientation.

Figure 4.21 compares the diffraction patterns from the same area before heating, at elevated temperature and after cooling. It is evident that the pattern quality improves at

high temperatures and after cooling. This may be explained by evaporation of surface contaminations. It is a well known fact that during scans the focused electron beam renders the sample surface with a contamination layer. During heating this contamination layer may evaporate. This is confirmed by the fact that even after quenching in vacuum the pattern quality is much better than before heating. The diffraction patterns may also have been improved by sample structure relaxation during heating. The discovery of increased pattern quality on heated steel samples allowed a shorter acquisition time, leading to a shorter scan time during the in situ experiments. This allowed scanning of a bigger area at elevated temperature without aggravating the drifting effect of thermal expansion.

Chapter 6

Conclusions

In this master thesis combined in situ heating and quenching have successfully been applied in conjunction with EBSD measurements inside the SEM. The goal was to use this combined technique to study the progressive microstructural development throughout a weld simulation test, such as the emergence of austenite during heating and the following formation of M-A phases after quenching.

The experiments have proven that gas quenching with high purity helium is a suitable technique for obtaining high cooling rates inside the SEM. The gas quenching can be carried out without risking damage to sensitive detectors and pumps.

It was found to be difficult to recreate the characteristic microstructure in the thermal weld simulated API X70 samples due to slow heating rate and the excessive high temperature holding time.

The contamination layer that occurs during gas quenching affects the indexing and gives unreliable results. Chemical analysis identifies the contamination layer as an oxide. The EBSD-analysis suggests a lattice structure close to FCC.

Accurate temperature measurements was found to be extremely difficult to obtain in high vacuum. As a result many of the in situ samples did not reach a peak temperature within the desired temperature interval.

The different BCC and FCC phases have been identified and characterized at the defined temperatures. Islands of austenite were observed when the steel was heated to approximately 800°C inside the two-phase ferrite (α) and austenite (α) region of the phase diagram. Examinations show that the orientation relationship between the fresh austenite and the surrounding martensite fulfills the K-S criteria, and suggests that the austenite is correctly indexed.

The austenite islands nucleated on both high angle and low angle grain boundaries. Neither retained austenite nor high strain martensite was observed in the API X70 steels after quenching, probably due to the holding time or the insufficient cooling rates.

Divergent transformation behavior of the austenite islands was observed during quenching. Some showed a memory-effect and ended up with the same BCC orientation as before the heating, whereas the others adopted the orientation of the neighboring grains.

Chapter 7

Further Work

To get a better understanding of the microstructure changes in the HAZ during welding of the X70 steel the following work should be performed:

- Measurements of sample temperature during in situ H/Q experiments needs to be improved. This can be done by replacing the thermocouples with infrared detectors inside the SEM.
- Solve the contamination problem by replacing the Teflon and plastic tubes with steel tubes. Also replacement of the gas valve needs to be considered.
- Investigate if the maximum heating rate of the heating system can produce more continuous MA-islands on the former austenite grain boundaries of API X70 steel.
- A more thorough examination of the preferred orientation relationship between the austenite formed during heating and the initial BCC structure.

Bibliography

[1] D.L. Gautier, K.J. Bird, R.R. Charpentier, A. Grantz, D.W. Hauseknecht, T.R. Klett, T.E. Moore, J.K. Pitman, C.J. Schenk, J.H. Schuenemeyer, K. Sorensen, M.E. Tennyson, Z.C. Valin, and J.C. Wandrey. Assessment of undiscovered oil and gas in the arctic. *Science*, 324:1175–1179, 2009.

[2] J.H. Chen, Y. Kikuta, T. Araki, M. Yoneda, and Y. Matsuda. Micro-fracture behaviour induced by ma constituent (island martensite) in simulated welding heat affected zone of ht80 high strength low alloyed steel. *Acta Metallurgica*, 32(10):1779–1788, 1984.

[3] O.M. Akselsen, Ø. Grong, and J.K. Solberg. Structure-property relationships in intercritical heat affected zone of low-carbon microalloyed steels. *Materials science and technology*, 3(8):649–655, 1987.

[4] O.M. Akselsen, J.K. Solberg, and Ø. Grong. Effects of martensite-austenite (M-A) islands on intercritical heat affected zone toughness of low carbon microalloyed steels. *Scand. J. Met.*, 17:194–200, 1988.

[5] C.L. Davis and J.E. King. Cleavage initiation in the intercritically reheated coarse-grained heat-affected zone: Part I. fractographic evidence. *Metallurgical and Materials Transactions A*, 25(3):563–573, 1994.

[6] C.L. Davis and J.E. King. Cleavage initiation in the intercritically reheated coarse-grained heat affected zone: Part II. failure criteria and statistical effects. *Metallurgical and Materials Transactions A*, 27(10):3019–3029, 1996.

[7] K.E. Thelning and C.M. Black. *Steel and its heat treatment.* Butterworths, 1984.

[8] J.K. Solberg. Teknologiske metaller og legeringer. Norwegian University of Science and Technology, December 2008.

[9] M.C. Zhao, Y.Y. Shan, F.R. Xiao, and K. Yang. Acicular ferrite formation during hot plate rolling for pipeline steels. *Materials science and technology*, 19(3):355–359, 2003.

[10] M.C. Zhao, K. Yang, and Y. Shan. The effects of thermo-mechanical control process on microstructures and mechanical properties of a commercial pipeline steel. *Materials Science and Engineering A*, 335(1-2):14–20, 2002.

[11] H. Bhadeshia and R. Honeycombe. *Steels: Microstructure and properties.* Elsevier, 3rd edition, 2006.

[12] K.W. Andrews. Empirical formulae for calculation of some transformation temperatures. *Iron and Steel Institute Journal*, 203(Part 7):721–727, 1965.

[13] J. Wang and A. Atrens. Microstructure and grain boundary microanalysis of x70 pipeline steel. *Journal of materials science*, 38(2):323–330, 2003.

[14] Y. Wang, T. Han, and W. M. Zhao. Influence of the second thermal cycle on coarse-grained zone toughness of x 70 steel. *Acta Metallurgica Sinica(English Letters)(China)*, 12(5):831–835, 1999.

[15] M. M'Hamdi M. I. Onsøien and A. Mo. A cct diagram for an offshore pipeline steel of x70 type. *Welding Journal*, 88(1), 2009.

[16] M. Karlsen, J. Hjelen, Ø. Grong, G. Rørvik, R. Chiron, U. Schubert, and E. Nilsen. Sem/ebsd based in situ studies of deformation induced phase transformations in supermartensitic stainless steels. *Materials Science and Technology*, 24(1):64–72, 2008.

[17] R.A. Schwarzer, D.P. Field, B.L. Adams, M. Kumar, and A.J. Schwartz. Present state of electron backscatter diffraction and prospective developments. *Electron Backscatter Diffraction in Materials Science*, pages 1–20, 2009.

[18] Struers. *Active Oxide Polishing Active Oxide Polishing Suspensions*. Struers A/S, Pederstrupvej 84, DK-2750 Ballerup, Denmark, January 2005.

[19] K.W. Hansen. Sample preparation and ebsd-characterization of api x70 steel; testing of vacuum quenching methods. Depth study, Norwegian University of Science and Technology, December 2011.

[20] J. Hjelen. Electron backscatter diffraction - ebsd in sem. Powerpoint presentation in the subject TMT14, NTNU, December 2011.

[21] M.M. Nowell and S.I. Wright. Orientation effects on indexing of electron backscatter diffraction patterns. *Ultramicroscopy*, 103(1):41–58, 2005.

[22] J. Hjelen. Scanning electron-mikroskopi. Metallurgisk Institutt, NTH, Trondheim, 1989.

[23] Y. Chen, J. Hjelen, SS Gireesh, and HJ Roven. Optimization of ebsd parameters for ultra-fast characterization. *Journal of Microscopy*, 2011.

[24] K. Lassen. Automatic high-precision measurements of the location and width of kikuchi bands in electron backscatter diffraction patterns. *Journal of Microscopy*, 190(3):375–391, 1998.

[25] EDAX TSL. *OIM Data Collection 6.0 user manual*, 2009.

[26] D.P. Field. Recent advances in the application of orientation imaging. *Ultramicroscopy*, 67(1):1–9, 1997.

[27] EDAX TSL. *OIM Analysis 6.0 user manual*, 2009.

[28] A.-J. Enstad. EBSD-karakterisering av et HSLA-stål under in situ varmebehandling. Master thesis, Norwegian University of Science and Technology, June 2011.

[29] J.H. Pedersen. EBSD-karakteriasering i sem av lavlegerte stål for arktiske applikasjoner. Master's thesis, Norwegian University of Science and Technology, June 2011.

[30] T.G. Sætran. Prøvepreparering og ebsd-karakterisering av f70 mikroegert stål; bråkjøling i vakuum. Depth study, Norwegian University of Science and Technology, December 2011.

[31] Vac Aero International Inc. Daniel H. Herring. Gas quenching. Available from: `http://www.vacaero.com/Vacuum-Heat-Treating-with-Dan-Herring/Vacuum-Heat-Treating-with-Dan-Herring/gas-quenching.html` [cited 11. December 2011].

[32] G. Aylward & T. Findlay. *SI Chemical Data*. John Wiley & Sons Australia, Ltd, 5th edition, 2002.

[33] Fishione Instruments, Inc. *Model 1020 – Plasma Cleaner*, 1997.

Appendix A

ISOPE-paper 2012-TPC-1048

Phase Transformation Study of Arctic Steels by EBSD during In Situ Heating and Gas Quenching

K. W. Hansen[1], T. G. Sætran[1], M. Karlsen[1,2], T. A. Nilsen[1], W. Dall[3] and J. Hjelen[1]
[1] Norwegian University of Science and Technology. [2] Statoil ASA. [3] SINTEF.
Trondheim, NORWAY

ABSTRACT

A gas quenching device was successfully developed and fitted into a field emission scanning electron microscope (FESEM) together with a purposely build hot stage. In situ heating and quenching were combined with electron backscatter diffraction (EBSD) measurements in order to study the development in the microstructure of arctic steel during a simulated second weld cycle. EBSD measurements were conducted on a one cycle weld simulated arctic steel sample before heating, at 800°C and after gas quenching. During quenching, islands of austenite (FCC) observed at elevated temperatures transformed into a BCC structure, assumed to be martensite. It was also found an increase in diffraction pattern quality during heating and after quenching, probably due to sample lattice stress relief or evaporation of the contamination layer.

KEY WORDS: Arctic steel; in situ heating; in situ quenching; EBSD; phase transformation.

INTRODUCTION

Due to the world's increasing energy demand the oil & gas companies are expanding their area of interest into new and unexplored regions. The findings of oil and gas deposits in the arctic region have created an interest of developing production sites in these extremely weather exposed areas. United States Geological Survey (USGS) estimates that approximately 30% of the remaining gas reserves and 13% of the remaining oil reserves may be located north of the polar circle (Gautier et al., 2009). The construction design in these areas has to be robust in order to ensure a long lifetime without needing excessive maintenance during production.

The rough climate in the arctic regions sets new requirements to the materials. Arctic steels, like the API X70 steel explored in this paper, are developed to withstand very low temperatures, with a ductile/brittle transition temperature below -60°C. However, during welding, brittle phases like martensite-austenite (M-A) islands may form in the heat affected zone (HAZ) (Chen et al., 1984; Akselsen et al., 1987 and 1988; Davis and King, 1994 and 1996), resulting in a lower strength and toughness, especially at low temperatures. Increased knowledge of how these phases form, and their influence on the arctic steels during low temperature exposure, is of great importance.

The objective of this paper is to understand the changes in the steel microstructure during welding. This will be done by combining in situ heat treatment and quenching experiments inside a field emission scanning electron microscope (FESEM) with the use of electron backscattered diffraction (EBSD) in order to simulate a second weld cycle operation. By combining the EBSD measurements with the in situ experiments, characteristics of the M-A phases forming can be studied.

Earlier experiments performed by A-J. Enstad et al. (2011) showed in situ heat treatment of arctic steel inside the SEM to a temperature of 790°C, enough to reach the two-phase ferrite (α) and austenite (γ) region. However, the sample cooling rate was too low to simulate the cooling rate during real time welding. Therefore, the authors have developed a specially designed cooling device that can be applied in conjunction with the heating stage. This cooling device can quench the steel sample with a cooling rate of up to 60°C/sec, representing that of a real time welding procedure, by gas quenching. To the authors knowledge it is the first time combined in situ heating and quenching is performed inside the SEM.

The principles of the EBSD technique is to record electron diffraction patterns (EBSP) from a sample surface tilted 70° inside a scanning electron microscope (SEM). For a fully automated EBSD system the electron beam scans the sample surface and for each step a new diffraction pattern is collected on a phosphor screen and captured by a digital camera. The diffraction patterns contain information about both the lattice structure (distinguish between BCC and FCC) and the crystallographic orientation of the point from which they originate. The conventional EBSD system is an online system where the diffraction patterns are indexed directly during EBSP acquisition. The EBSD technique involves both the acquisition of patterns by the camera and the indexing of the patterns by computer software. The recent development of camera technology, however, has made pattern indexing to be the bottleneck in EBSD analysis. Increased EBSD acquisition speed has been obtained using EBSD offline systems, where patterns are streamed directly to the hard drive for later off-line indexing (Schwarzer and Hjelen, 2010). High scan speed is essential during in situ experiments. It shortens

the time of measurements and thus alleviates the difficulties with long-term stability of the SEM during in situ investigations (Schwarzer et al. 2009).

EXPERIMENTAL

In Situ Heating and Quenching

The investigation presented in this paper involves in situ heating of API X70 steel and subsequent rapid cooling inside the SEM.

In earlier studies performed by the authors (K. W. Hansen, 2011; T. G. Sætran, 2011) different vacuum cooling methods were tested. By putting a cold medium (-140°C) in contact with a hot steel sample (400°C) inside a vacuum chamber, the idea of contact cooling was tested. The results of 2°C/sec showed that heat transfer was extremely difficult to achieve in vacuum conditions, which led to a focus on gas quenching in the following pursuit of rapid cooling methods in vacuum.

Prior to the in situ experiments the potential of gas quenching was tested inside an external vacuum chamber, pictured in Fig. 1. High purity argon and helium gas was used to vent the chamber through a nozzle directly towards a steel sample surface.

Fig. 1. The external vacuum chamber used to design and test the potential of gas quenching.

The heating was done with a specially developed furnace (Chiron et al., 1996) that has been used in previous heating experiments of HSLA steel (Enstad, 2011). The cooling unit used in this experiment was designed and developed with respect to the existing furnace/hot stage. Rapid cooling was achieved by spraying helium gas at room temperature directly on the surface of the hot sample. The cooling system consisted of a rig that was mounted to the stage inside the SEM, a tube that was aimed towards the sample and a vacuum-tight gas connection for the SEM. These are seen in Fig. 2~3. All components were made from stainless steel. A Teflon® tube was used inside the SEM to connect the tube on the rig with the gas connection. To avoid damage on the turbo pump the SEM was modified for alternative venting by the cooling gas through the gas nozzle. To the authors knowledge it is the first time combined in situ heating and quenching is performed inside the SEM.

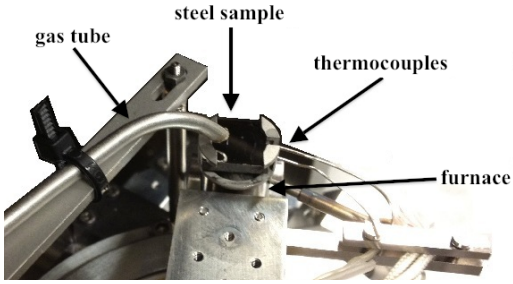

Fig. 2. The hot stage including the cooling rig for gas quenching.

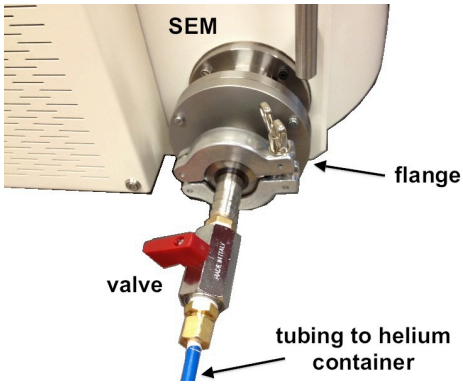

Fig. 3. The vacuum-tight gas connection to the SEM.

Material

API X70, the material studied in the presented work, is a HSLA steel developed for low temperature applications with a chemical compositions of 0.05C-0.10Si-1.74Mn-0.009P-0.001S-0.21Cu-0.06Cr-0.24Ni-0.05Mo-0.001V-0.035Al-0.027Nb-0.003N (wt%). Prior to the experiments the samples were subjected to a single cycle weld thermal simulation with a maximum temperature of 1350°C and a cooling time between 800°C and 500°C, $\Delta t_{8/5}$, of 5 seconds, equivalent to a mean cooling rate of 60°C/sec. This first cycle weld simulation was performed on a Smithweld TCS model 1405.

The X70 specimens for EBSD observation were prepared by chemical-mechanical polishing (Struers OP-S). All specimens went through a cleansing step in an ultrasonic bath of acetone and ethanol for 30 minutes and 5 minutes, respectively, before being purified in a Fishione 1020 Plasma Cleaner for 5 minutes.

SEM/EBSD parameters and testing conditions

The SEM used during the experiments was a Zeiss 55 Ultra FESEM with the Nordif UF-1000 EBSD detector for ultra fast pattern acquisition and later offline EBSD indexing. The EBSD investigation was done with an acceleration voltage of 20kV, a 70° tilt angle, an

aperture size of 300 µm in high current mode, giving about 50 nA current, and a working distance of 21 mm.

The EBSD mapping was done on an area of 100x100 μm^2 at room temperature before the samples were heated and on an area of 40x40 μm^2 once the samples reached the maximum temperature. The step size was 200 nm on all scans. The acquisition time for the EBSD maps was then 2 minutes and 13 seconds when the samples were at the maximum temperature. The heating rate was $1^oC/s$. To minimize the drifting effect of thermal expansion the EBSD mapping was carried out after the sample had reached a steady temperature of approximately 800^oC for 10 minutes. After the EBSD scan the sample was quenched, followed by a new 100x100 μm^2 scan. The cooling rate could somewhat be controlled by the pressure of the helium gas during cooling. All samples were cooled at a rate between 40 and 60°C/sec. The inlet pressure was 0.3 bar, similar to the maximum inlet pressure during standard venting, and the nozzle diameter was 2.0 mm, positioned a few millimetres from the sample surface.

EDAX/TSL OIM Data Collection 5.32 was used to index the NORDIF pattern files. EDAX/TSL OIM Analysis 6.1 EBSD software was applied for post processing of the diffraction data. The software offers several data cleaning methods, but no cleaning was used in the present study to avoid manipulation of the raw data. However, in order to give a representative distribution of α- and γ-phase, pixels with a CI-value bellow 0.05 was removed from the phase maps in Fig. 6~7.

RESULTS

Development of Cooling Unit

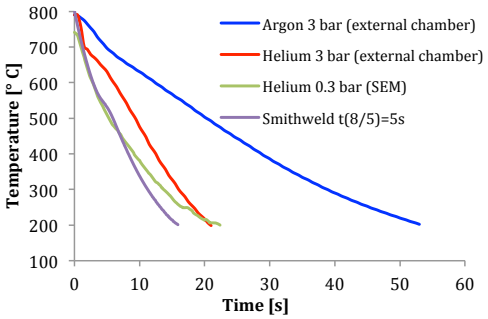

Fig. 4. Cooling curves recorded during gas quenching inside an external vacuum chamber and inside the SEM, in addition to a reference cooling curve from a weld simulation test.

The ventilation system of the Zeiss 55 Ultra FESEM was modified in order to vent the SEM with a noble gas through a nozzle directly on to the specimen surface. Fig. 4 shows the cooling curves obtained both in the external vacuum chamber (Fig. 1) and inside the SEM, in addition to a reference cooling curve recorded during the first weld cycle simulation test on the Smithweld TCS model 1405. The cooling rate recorded in the external vacuum chamber is lower than what was recorded inside the SEM in spite of having a higher helium gas pressure. This is due to the dissimilar testing conditions, including the sample size, the furnace size and the nozzle-to-sample distance.

Due to general thermal transition problems in vacuum the heat transfer between the thermocouple and the sample was poor and gave an incorrect temperature measurement. In order to measure the correct sample temperature in the experiments it was considered to spot weld a thermocouple to each steel sample. However, the idea was rejected due to the danger of overheating the sample and thus affecting the microstructure. Therefore the error between the measured and real temperature had to be found. An additional thermocouple was spot welded to the surface of a reference sample, ensuring proper contact. The deviation between the measured temperature and the real temperature was found to be approximately 50°C with a sample temperature of 800°C. A measured temperature of 750°C corresponded to a correct temperature of 800°C, which had to be accounted for in the in situ experiments.

In situ EBSD scans

Fig. 5 shows the EBSD orientation maps of the same selected area before heating, at 800°C and after quenching. The different colours in the maps represent different crystal orientations and grains with the same colour have the same crystal orientation with respect to the specimen surface. Before heating the microstructure is clearly influenced by the first cycle weld simulation and consists of coarse-grained martensite and bainite.

Two selected cropped areas are given in Figs. 6~7. These images show EBSD orientation maps, phase maps and image quality maps of the two areas before heating, at 800°C and after rapid cooling. The martensite and the bainite both have BCC structures and appear red in the phase map. The austenite (FCC) is colour coded green.

Confidence index (CI) is the most important quality parameter in the TSL software. The CI-value is a number between 0 and 1 and represents the probability of the selected pattern solution to be correct compared to the second best solution (EDAX TSL, 2009). Pixels with a confidence index (CI-value) bellow 0.05 are improperly indexed. They are removed and appear white in the phase maps.

The IQ-maps (Image Quality) show the pattern quality and is dependent on factors like the strain in the diffraction volume, the presence of impurities, contamination and the phase of the material. A dark area represents low IQ-values and thus poor quality patterns. Table 1 shows the maximum and minimum IQ-values before heating, at 800°C and after quenching in crop 1 and 2, respectively.

Table 1: Maximum and minimum IQ-values.

	Before heating		**At 800°C**		**After cooling**	
	min	max	min	max	min	max
Crop 1	129	294	42	296	67	266
Crop 2	91	240	32	300	61	274

The orientation relationship in the FCC-BCC transformation can be expressed in terms of close-packed planes and directions in the two phases. The Kurdjumov-Sachs (K-S) relationship describes the four close-packed $\{111\}_\gamma$-planes and the six BCC-variants that can form from each austenite plane, giving 24 preferred orientations of martensite from the parent austenite grain.

Fig. 9a shows the 24 theoretical BCC-variants of a cube oriented austenite crystal plotted in a standard {100} pole projection figure (M. Karlsen et al., 2007). In Fig. 9b the scan at 800°C in Fig. 5 is rotated to the same cube orientation to be able to directly compare the BCC-variants observed. The austenite that forms at 800°C clearly have an orientation relationship with the surrounding martensite that corresponds to the K-S relationship.

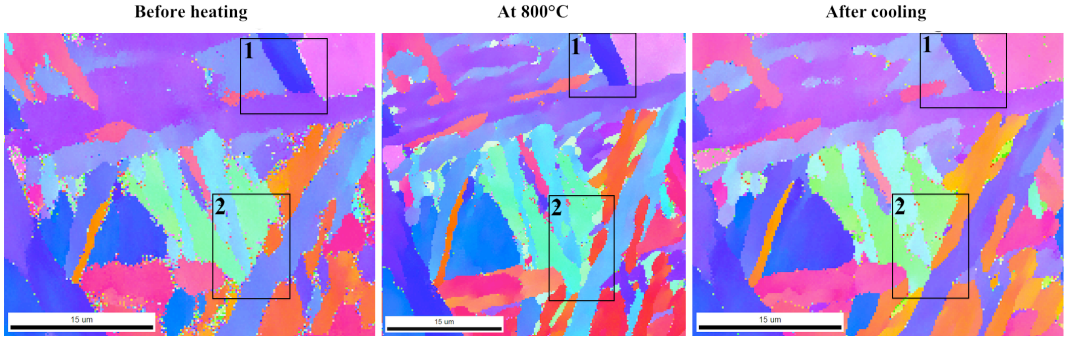

Fig. 5. EBSD orientation maps before heating, at 800°C and after cooling. Crop 1 and 2 are further analysed in Fig. 6 and Fig. 7, respectively.

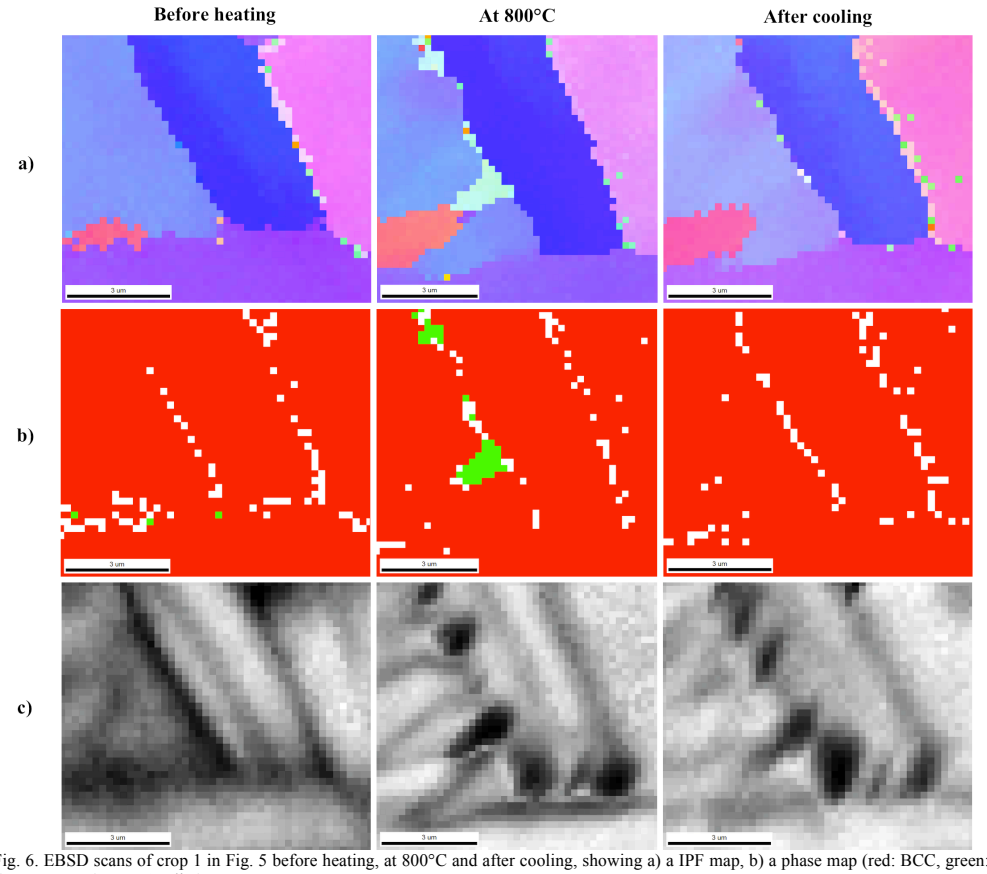

Fig. 6. EBSD scans of crop 1 in Fig. 5 before heating, at 800°C and after cooling, showing a) a IPF map, b) a phase map (red: BCC, green: FCC) and c) an IQ map (Image Quality).

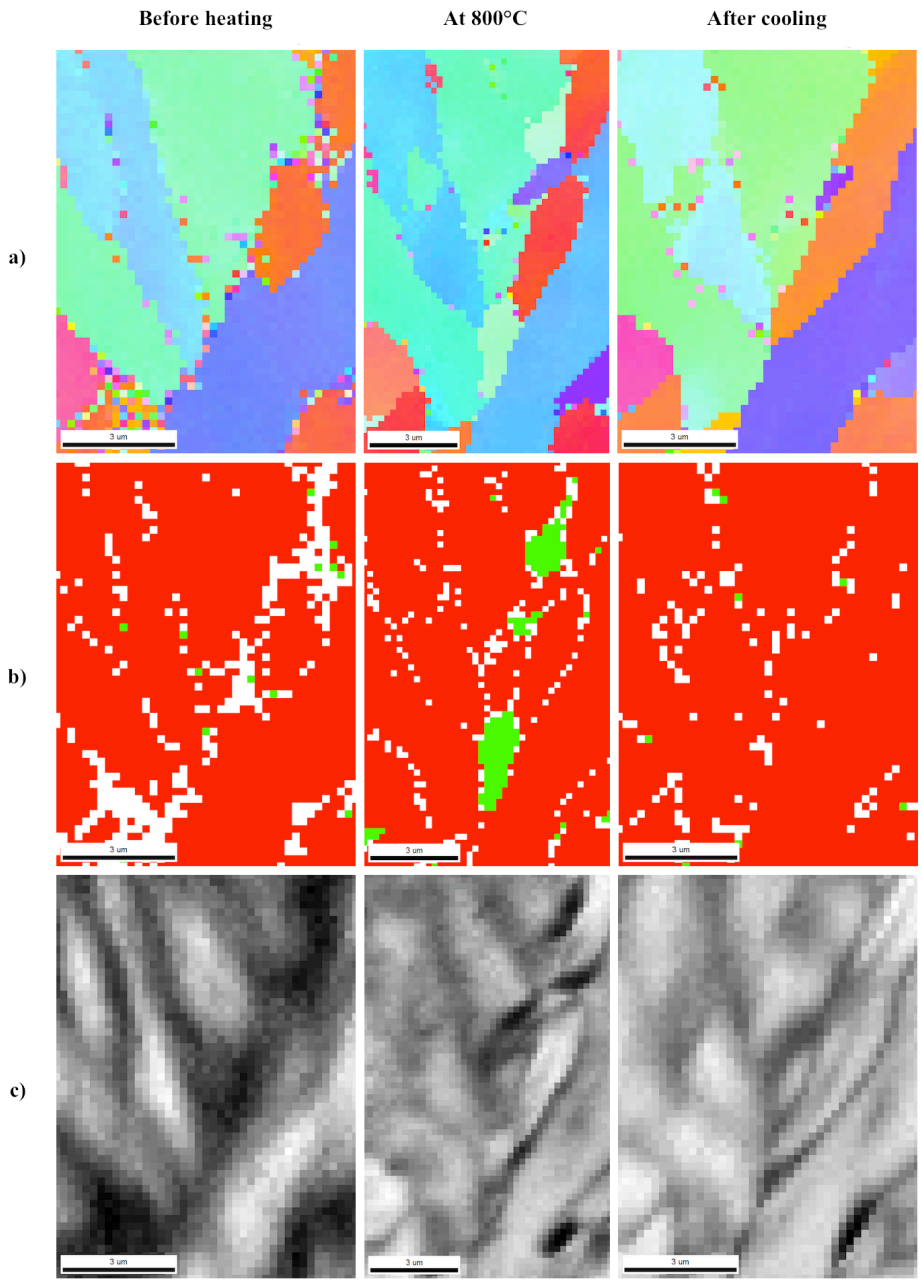

Fig. 7. EBSD scans of crop 2 in Fig. 5 before heating, at 800°C and after cooling, showing a) a IPF map, b) a phase map (red: BCC, green: FCC) and c) an IQ map (Image Quality).

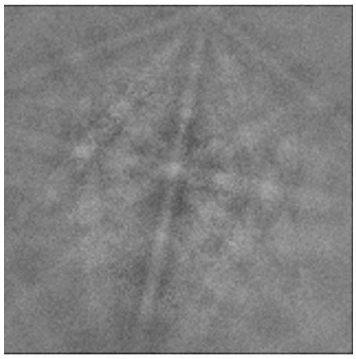

a) Before heating

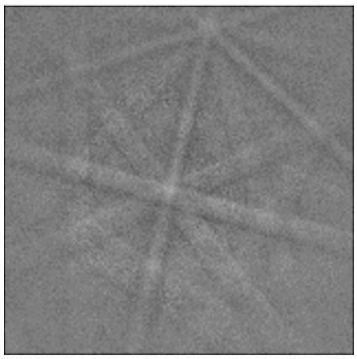

b) At 800°C

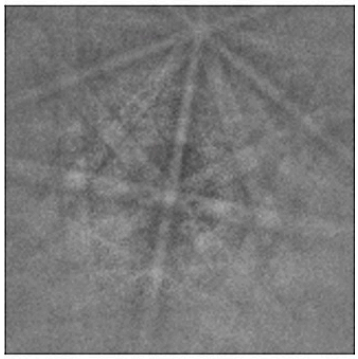

c) After cooling

Fig. 8. The diffraction patterns for the same surface area a) before heating, b) at 800°C and c) after cooling.

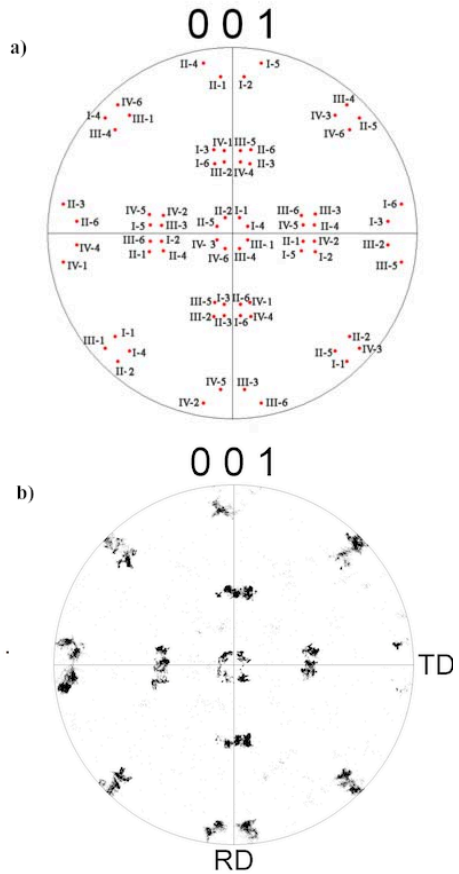

Fig. 9. Standard {100} pole projections of a) the 24 possible K-S martensite variants originating from a single (001)[100] austenite orientation (M. Karlsen et al., 2007) and b) a rotated data set of variants observed in Fig. 5 at 800°C.

DISCUSSION

In the present paper combined in-situ heating and quenching have successfully been applied in conjunction with EBSD measurements inside the SEM.

By using this combined technique it is possible to study the progressive microstructural development throughout a weld simulation test, such as the emergence of austenite during heating and the following formation of M-A phases after quenching.

The tests performed in the external vacuum chamber prior to the in situ experiments showed a great difference in the cooling ability of argon and helium. Helium has a 10 times higher heat capacity and an 8 times higher heat conductivity compared to argon, which can explain this significant improvement. A cooling curve similar to that of a real weld

simulation test can be achieved by jetting helium through a nozzle directly onto a steel sample surface. The curves in Fig. 3 prove that gas quenching is a suitable technique for obtaining small scale rapid cooling experiments inside a SEM.

Vacuum presented several challenges regarding heat transfer during these experiments. From the early experiments with a cold finger we learned that heat transfer only by conduction and radiation was insufficient to obtain the higher cooling rates. Measuring and controlling the sample temperature represented a likewise issue. To ensure a steady state temperature during heating the sample and keeping the temperature within the two-face ($\alpha+\gamma$) region of the phase diagram, the experiments were dependent on a sufficient thermocouple contact with the sample.

From the IQ-maps in Fig. 6~7 it is evident that the pattern quality improves at high temperatures and after cooling. This may be explained by evaporation of surface contaminations. It is well known fact that during scans the focused electron beam renders the sample surface with a contamination layer. During heating this contamination layer may evaporate. This is confirmed by the fact that even after quenching in vacuum the pattern quality is much better than before heating. The diffraction patterns may also have been improved by sample structure relaxation during heating. Fig. 8 is an example of how the diffraction patterns improve after heating.

The majority of improperly indexed points (white pixels) in the phase maps of Fig. 6~7 are located next to or at the grain boundaries. This is likely due to the overlapping of two or more diffraction patterns in these regions. As a consequence the computer software faces trouble distinguishing between the patterns and thus give a correspondingly low CI-value.

The combination of in situ heating and in situ quenching described in this paper can be used to study the changes in microstructure during the second welding cycle simulation of arctic steel. Fig. 6 shows a cropped area where an austenite island emerges upon heating and transforms into BCC structure during quenching. Despite the high cooling rate it was not observed any residual austenite in the final scan. One explanation may be surface evaporation of carbon during the holding time at 800°C, as previously discovered by A.-J. Enstad et. al. (2011).

IPF maps show that the austenite emerges from the high angle grain boundaries having a different crystallographic orientation than the surrounding grains. IPF maps also show that the austenite islands emerging in crop 2 (Fig. 7) have the same crystallographic orientation as the austenite island in crop 1, which indicates that the characterized areas appear inside the same former austenite grain. The austenite orientation fulfils the K-S criteria indicating that the austenite is correctly indexed.

Crop 2 in Fig. 7 holds an area that changes crystallographic orientation heat treatment. The area with a crystal coloured blue transforms into austenite. During quenching this austenite transforms and adapts the orientation of the neighbouring grain coloured orange.

The IQ-map in Fig. 6c and 7c reveal dark areas along the grain boundaries before heating. At 800°C fresh dark spots have formed near triple points. The spots are maintained also after quenching. Table 1 shows a tendency of significantly lower IQ-minima at 800°C and after quenching compared to the scan acquired before heating. In general the IQ-value is a relative value and should only be compared within the same scan. However, the high differences in IQ-minima and the differences in spread of IQ make it easy to assume a lower pattern quality within the dark spots. This may also lead to the interpretation that the dark spots have greater lattice strain (e.g. higher dislocation density). The nature of the formation of these dark spots during heating is unknown to the authors.

CONCLUSIONS

The following basic conclusions may be drawn from the present examination:

- To observe progressive microstructural development in the API X70 steel, combined in situ heating and quenching have successfully been applied in conjunction with EBSD measurements inside the SEM.
- Several cooling experiments inside a vacuum test chamber revealed that gas quenching would be the best technique for rapid sample cooling inside the SEM.
- The increased diffraction pattern quality observed during heating is probably caused by the evaporation of contaminations. The high pattern quality is maintained after quenching. Pattern quality improvement may also be due to sample lattice stress relief during heating.
- The different BCC and FCC phases have been readily identified and characterised at the defined temperatures. Islands of austenite were observed when the steel was heated to approximately 800°C inside the two-phase ferrite (α) and austenite (γ) region of the phase diagram. Examinations show that the orientation relationship between the fresh austenite and the surrounding martensite fulfils the K-S criteria, and suggests that the austenite is correctly indexed. Quenching of the steel led to a transformation of austenite islands from a FCC structure to a BCC structure, which is assumed to be martensite. Probably due to evaporation of carbon from the sample surface throughout the holding time at 800°C, no residual austenite was observed after quenching.
- Divergent transformation behaviour of the austenite islands was observed during quenching. One ended up with the same BCC orientation as before the heating, whereas the other adopted the orientation of the neighbouring grain.

ACKNOWLEDGEMENTS

The authors acknowledge the Norwegian University of Science and Technology (NTNU) and SINTEF for providing access to the equipment and materials used in the present investigation. The authors wish to thank department engineer Harald Holm for support in the field of electronics.

REFERENCES

Akselsen, OM, Grong, Ø, Solberg, JK (1987). "Structure-Property Relationships in Intercritical Heat Affected Zone of Low Carbon Microalloyed Steels", *Mater. Sci. Technol.,* Vol. 3, pp 649-655.

Akselsen, OM, Solberg, JK, Grong, Ø (1988). "Effects of Martensite-Austenite (M-A) Islands on Intercritical Heat-Affected Zone Toughness of Low Carbon Microalloyed Steels", *Scand. J. Met.,* Vol. 17, pp 194-200.

Chen JH, Kikuta, Y, Araki, T, Yoneda, M, and Matsuda, Y (1984). "Micro-fracture Behaviour Induced by M-A Constituent (Island Martensite) in Simulated Welding Heat Affected Zone of HT80 High Strength Low Alloy Steel", *Acta Metall.,* Vol. 32, pp 1779-1788.

Chiron, R, Fryet, J, and Lesegno, P (1996). "Device for SEM and EBSP In Situ Tensile Tests up to 800°C, in Local Strain and Temperature Measurements in Non-Uniform Fields at Elevated Temperatures", *Woodhead Publishing Limited, Cambridge UK,* pp 149-158.

Davis, CL, and King, JE (1994). "Cleavage Initiation in the Intercritically Reheated Coarse-Grained Heat Affected Zone: Part I. Fractographic Evidence", *Metall. Mater. Trans.,* Vol. 25A, pp 563-573.

Davis, CL, and King, JE (1996). "Cleavage Initiation in the Intercritically Reheated Coarse-Grained Heat Affected Zone: Part II. Failure Criteria and Statistical Effects", *Metall. Mater. Trans*., Vol. 27A, pp 3019-3029.

EDAX TSL (2009), *"OIM Data Collection 6.0 user manual"*.

Enstad, AJ, Karlsen, M, Astad, SP, Hjelen, J, Akselsen, OM, and Østby, E (2011). "EBSD Characterization of Arctic Steel During In Situ Heating", *ISOPE 2011*, pp 28-32.

Gautier, DL, Bird, KJ, Charpentier, RR, Grantz, A, Houseknecht, DW, Klett, TR, Moore, TE, Pitman, JK, Schenk, CJ, Schuenemeyer, JH, Sorensen, K, Tennyson, ME, Valin, ZC, and Wandrey, JC (2009). "Assessment of Undiscovered Oil and Gas in the Arctic", *Science*, 324(5931):1175-1179.

Hansen, KW (2011). "Sample Preparation and EBSD-characterization of API X70 Steel; Testing of Vacuum Quenching Methods". Specialization project, Norwegian University of Science and Technology.

Karlsen, M, Hjelen, J, Grong, Ø, Rørvik, G, Opdahl, C, Chiron and Shubert, U (2007). "Deformation-Induced Phase Transformations in Supermartensitic Stainless Steels", *Stainless Steel World Conf. & Expo.,* Maastricht, The Netherlands, Nov. 6-8, 2007, paper no. 7017.

Schwarzer, RA, Field, DP, Adams, BL, Kumar, M, and Schwartz, AJ (2009). "Present State of Electron Backscatter Diffraction and Prospective Developments", *Electron Backscatter Diffraction in Material Science*, pp 1-20.

Schwarzer, RA, and Hjelen, J (2010). "High-Speed Orientation Microscopy with Offline Solving Sequences of EBSD patterns", *Solid State Phenomena,* Vol. 160, pp 295-300.

Sætran, TG (2011). "Prøvepreparering og EBSD-karakterisering av F70 mikrolegert stål; bråkjøling i vakuum". Specialization project, Norwegian University of Science and Technology.

Appendix B

In Situ Quenching Manual

The following is the assembly manual for the quenching device made to be used in conjunction with the *in situ* hot stage. Use gloves during the whole installation. If you are inexperienced in working with this equipment or feel uncomfortable with assembling the quenching device, you should ask an experienced user for help. In SEMlab the contact person for this device is Tor A. Nilsen.

Required tools:

- 1 x 32 mm wrench for connecting the hose to the regulator on the gas bottle.
- 2 x monkey wrench.
- 1 x Phillips flat-head screwdriver for connecting the flange for the gas tight connection to the flange on the microscope.
- 1 x 3 mm Allan key for connecting the flange for the microscope to the microscope.

Figure 1: Required tools for installation of the quenching device.

Bill of materials

Most of the parts listed below are already connected together. If the Teflon tubes are not already connected to the regulators, valves, connections, etc. make sure that Teflon tape is used in order to ensure vacuum tight sealings.

Table 1: List of parts for the in situ quenching device.

Item	Quantity	Notes
Helium gas container	1	High purity helium 6.0
Gas regulator for helium container	1	Fully opened
Teflon tubes	3	
AGA gas regulator	1	Set to 0,3 bar
Gas valve	1	
Gas tight connection	1	
Flange	1	Connect to flange adapter
Flange adapter	1	Connect to SEM
Quenching tube (SS)	1	To be mounted on quenching rig
Quenching rig pins	2	
Quenching rig beam	1	
Port cover to SEM	1	Replaced with EDS detector
Ventilation switch	1	Disconnects the normal ventilation system
Metal lens ring	1	Replaced with Backscatter detector

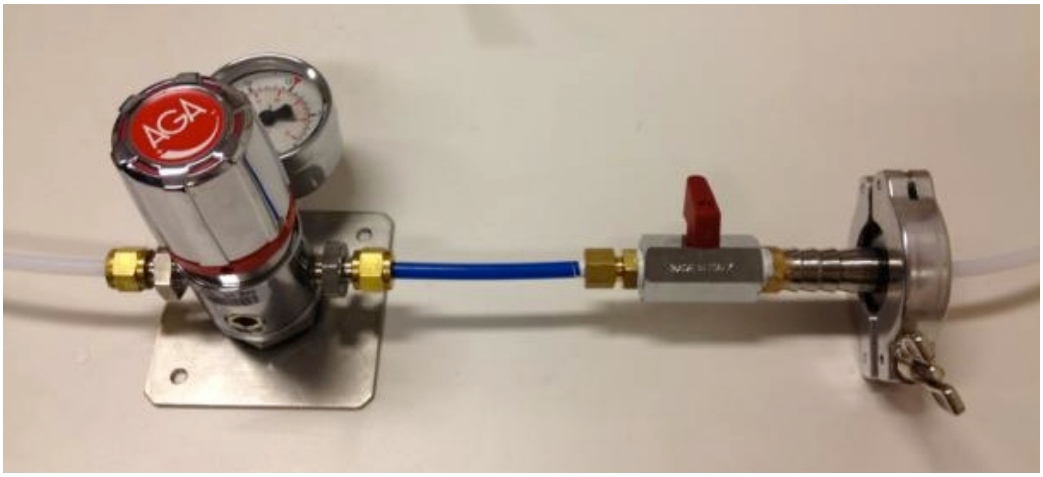

Figure 2: The AGA gas regulator in connection with the gas valve and the gas tight connection.

Figure 3: Flange

Figure 4: Flange adapter

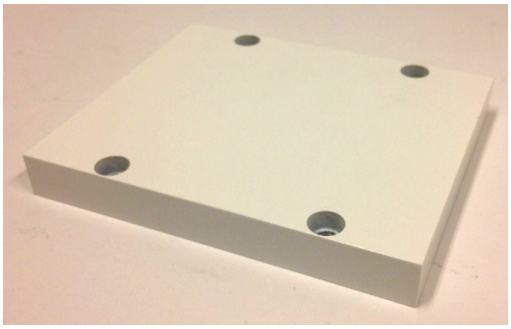

Figure 5: Port cover for EDS detector

Figure 6: Metal lens ring

Figure 7: Ventilation switch for disabling of the normal SEM ventilation system.

Figure 8: The stainless steel quenching tube fitted onto the quenching rig.

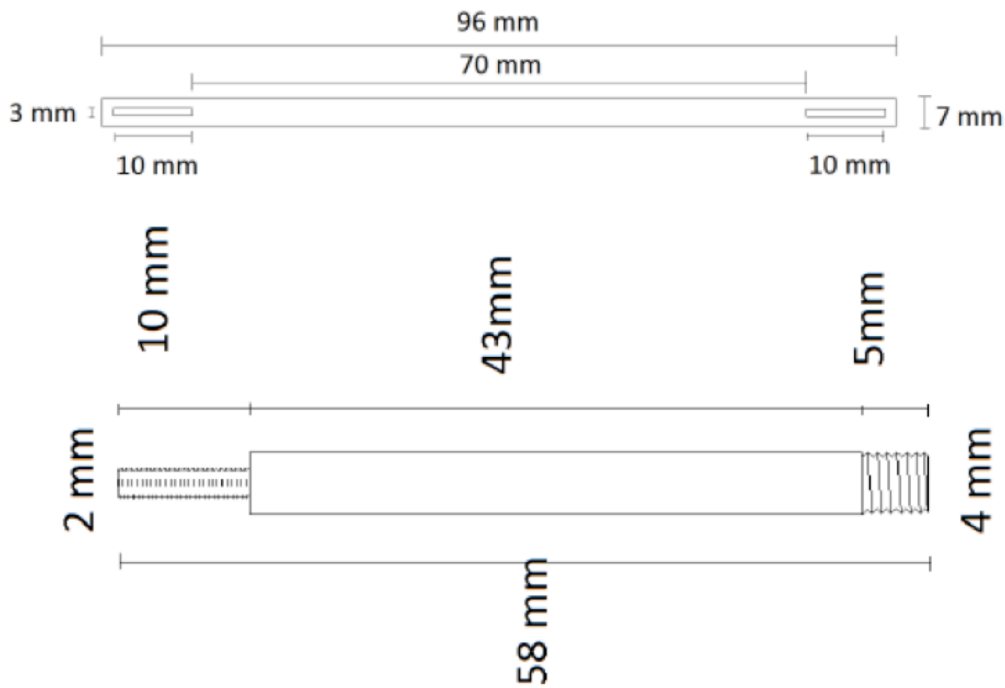

Figure 9: Working sketch of the quenching rig, showing beam and pin.

Assembling of the in situ quenching device

Helium container

First make sure that the helium container is secured with straps to avoid the container from tipping over. Then ensure that the gas regulator on the helium container is correctly installed. To attach the regulator a 32 mm wrench must be used. Then attach the gas tube for the quenching system to the regulator. This is done with a monkey wrench. Use Teflon tape to make sure there is no leak. The helium container and the regulator are shown in Figure 10.

Figure 10: The helium container and the regulator.

Dismounting of the EDS-detector

To avoid any risk of damaging the EDS-detector during in situ heating and quenching the detector should be removed. First turn off the power to the EDS-detector. Wait for *20 minutes* before removing the signal cable on the back of the EDS-detector (Figure 9). If not the electronics can be damaged.

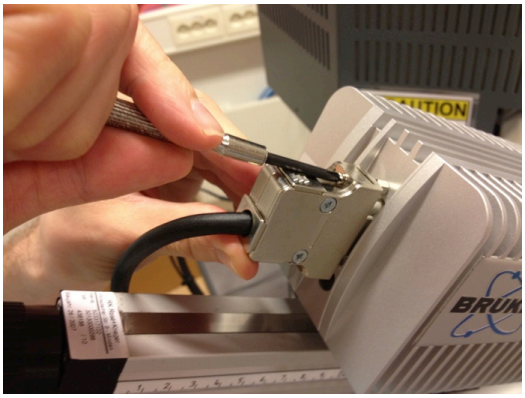

Figure 11:Removal of the EDS signal calbe.

Figure 12: The detector is screwed out.

The detector is then screwed out to outer position (Figure 12). Carefully replace the detector with the SEM port cover (Figure 13). *Take special care and avoid the detector from hitting the walls of the chamber when it is pulled out! This is a two-person job*. Ask Tor A. Nilsen for help if you are an inexperienced user.

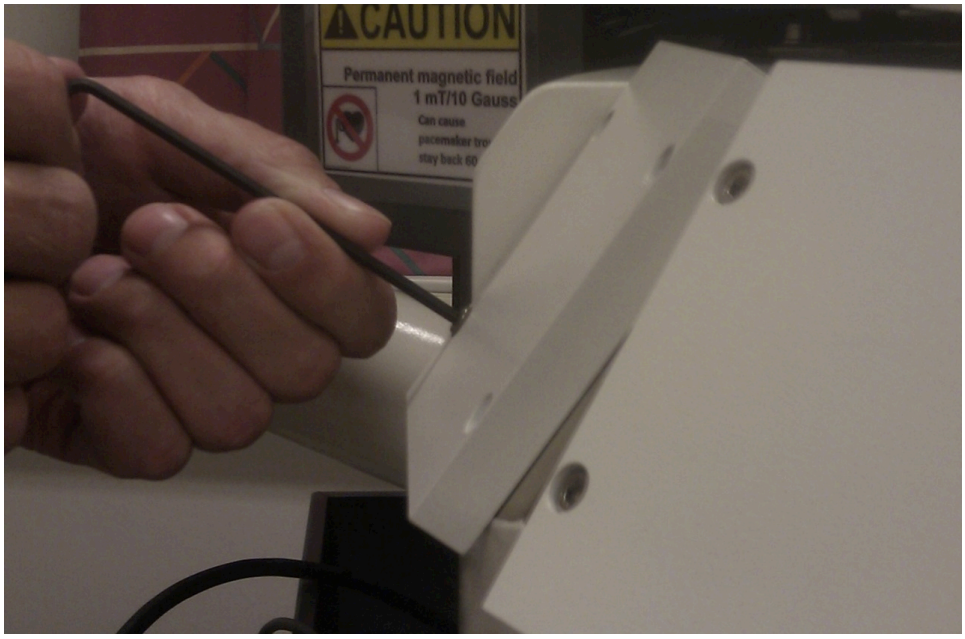

Figure 13: Replacing the EDS-detector with the SEM port cover.

Mounting the gas inlet to the SEM

The lower port on the SEM door is used for the gas inlet. Replace the port cover with the flange adapter. Mount the small flange onto the flange adapter, before feeding the tube into the SEM (Figure 14). The gas tight connection is then tightened (Figure 15).

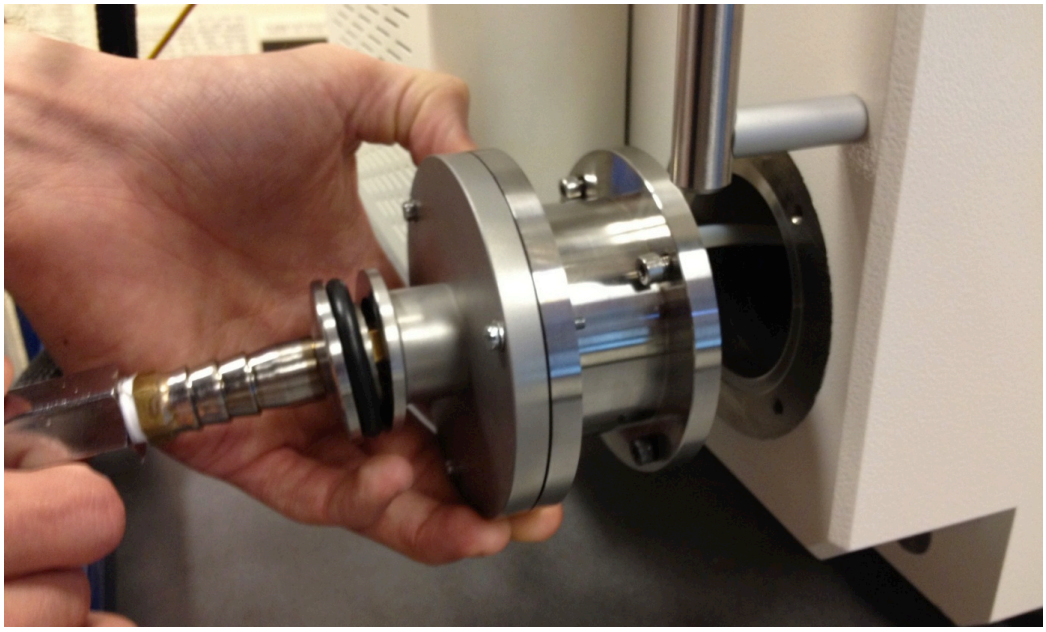

Figure 14: The flange adapter, followed by the small flange. The gas valve can be spotted on the left.

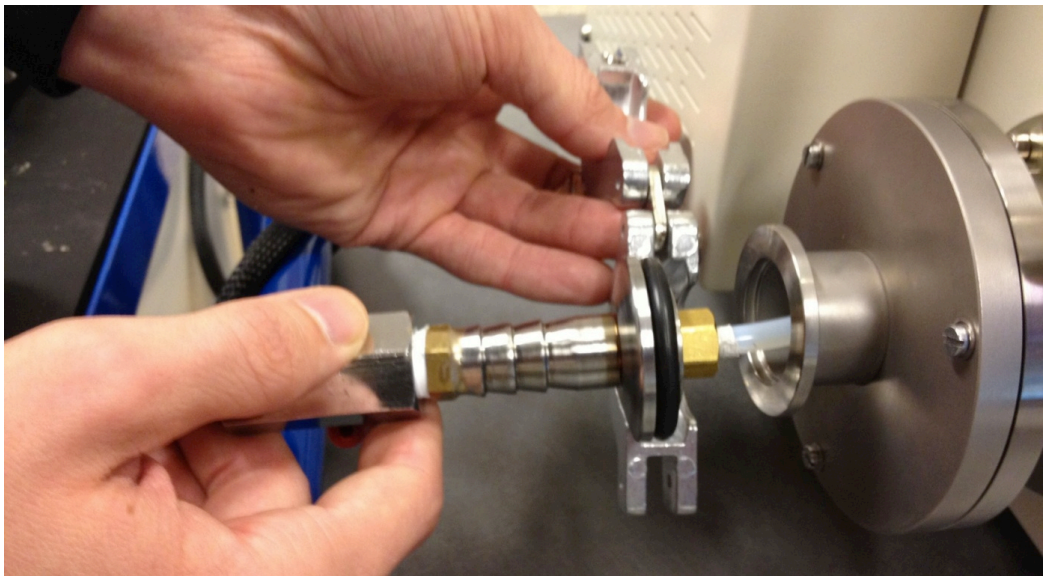

Figure 15: The gas tight connection.

At this point all the modifications on the outside of the SEM are made. Inside the SEM the Backscatter detector has to be removed from beneath the electron lens. The metal lens ring in Figure 6 is put in its place. Contact Tor A. Nilsen if you are an inexperienced user.

Mounting of the quenching rig inside the SEM

The mounting of the quenching can be done in two ways. The stainless steel gas tube can be fitted onto the quenching rig, using plastic strips, either before or after the rig is installed in the SEM. The easiest procedure is to fit the tube prior to the installation and then later adjust the gas outlet to the heating stage, as shown in Figure 16 and Figure 17. The in situ hot stage is now mounted onto the SEM stage and rotated. The stainless steel tube is adjusted so that the spacing between the gas outlet and the sample surface is minimized (Figure 18). Ad or remove the fittings on the quenching stage in order to achieve the desired spacing.

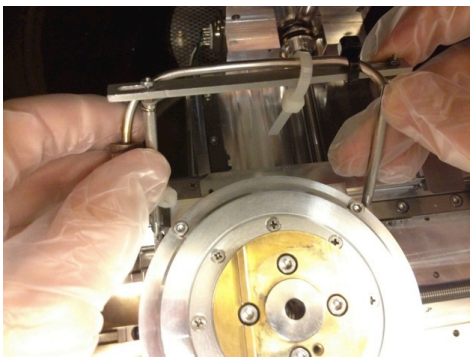

Figure 16: The stainless steel gas tube and quenching rig is installed inside the SEM

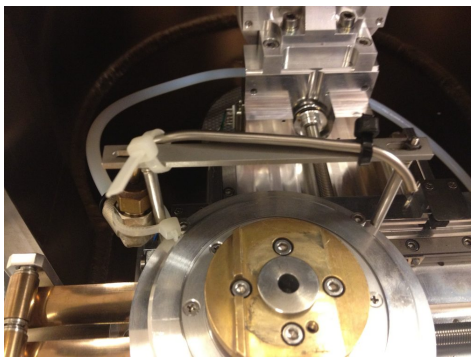

Figure 17: The quenching rig mounted on the SEM stage.

Figure 18: After the quenching rig has been installed inside the SEM the in situ hot stage may be mounted to the SEM stage. The stainless steel tube is adjusted and the distance between the gas outlet and the sample is minimized.

Use of the quenching device

After the hot stage has been mounted two positions have to be noted. A position in this chase refers to the rotation angle of the stage. The first position is where the EBSD scans will be performed once the stage is tilted to 70 ^{o} and set to the correct height. This is seen in Figure 19. The second position is the position where the sample is quenched. This is found by rotating the sample in direction of the gas outlet, typically a rotation of 30 ^{o} from the initial position. This is shown in Figure 20.

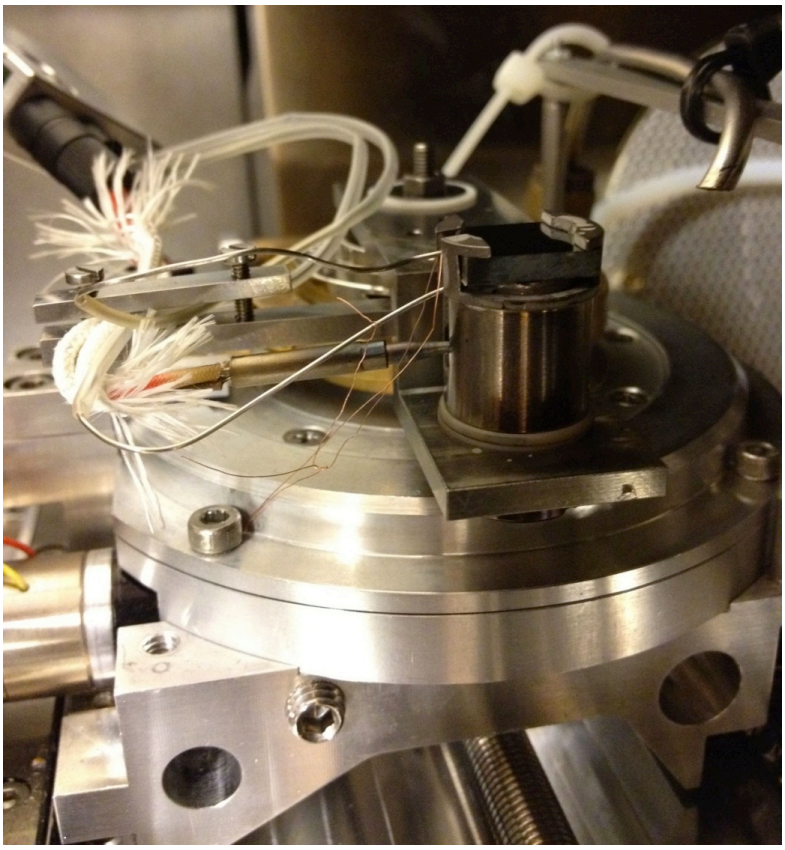

Figure 19: The figure shows the position where the EBSD scans can be performed.

At this point it will become clear if the spacing between the gas outlet and the titanium casing is big enough for the hot stage to pass during rotation. If a gap is not present it will not be possible to rotate the hot stage and quench the sample during an experiment. In this case the rig may have to be removed from the stage and more fittings must be placed on the pins to elevate the stainless steel gas tube. By doing this the gap between the sample surface and gas outlet increased.

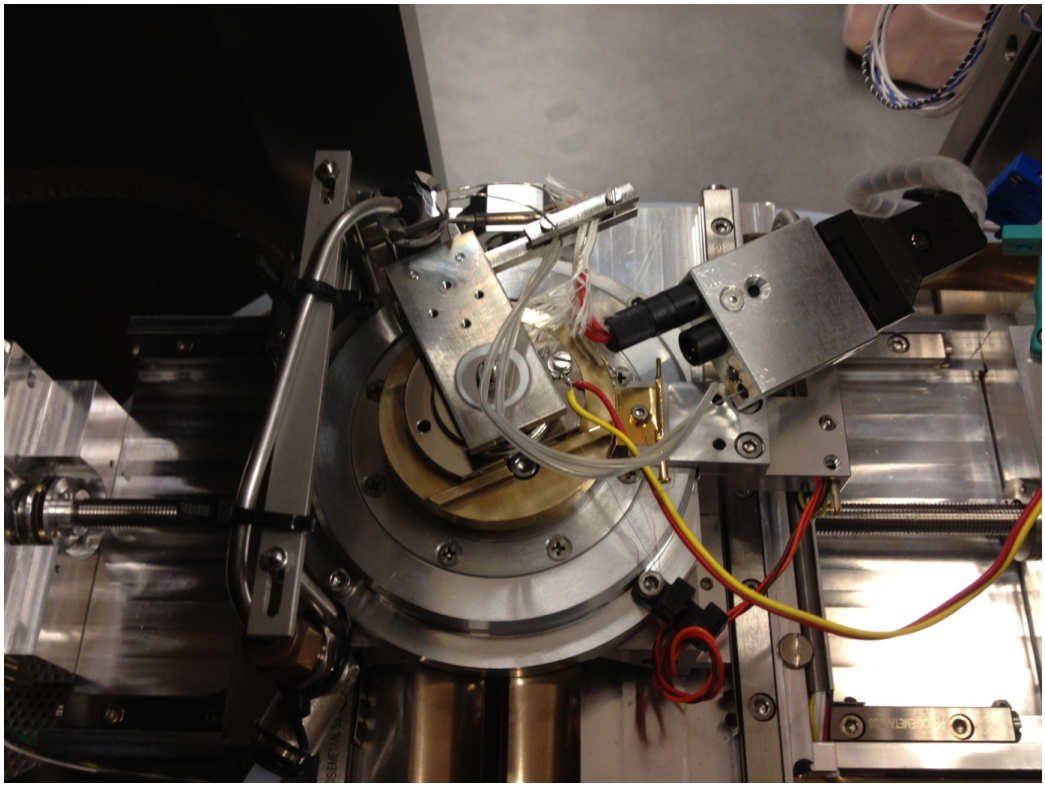

Figure 20: The position used during quenching.

Rotate the hot stage back to the initial position in order to do the EBSD scan. Tilt the SEM stage to 70 ^{o} before closing the sample chamber. Choose a Y- and X-value about 103 mm and 63 mm, respectively. This is approximately the position in sample chamber where the middle of the sample is directly beneath the lens.

The quenching system should be flushed with helium immediately after vacuum pumping has started. This is done in order to get rid of any air or other pollutions that may be inside the gas tubes. After a minute the valve should be closed so that high vacuum may be established.

Quenching:

The following routine should be followed during sample quenching:

- The vacuum switch must be in outer position.
- Withdraw the EBSD detector to its outer position and close the NORDIF software.
- Turn off the high voltage.
- Rotate the sample to the quenching position.
- Press the "Exchange" button on the SEM keyboard.
- Wait for the column to be lowered (the flushing sound faints out).
- Turn off the furnace and open the gas valve. Stop flushing when the sample temperature (T2) reaches 80 ^{o}C.

Error with measurements; cause and solutions:

Sometimes the temperature measurements are obviously incorrect. This can come from the following reasons:

- Lack of contact between the interfaces and connections from inside the SEM and out to the power supply. T1 and T2 will show "980 ^{o}C" and "-Inf", respectively. Ensure that all the connections are connected.
- A wire in the cable has fractured. This can happen in the sockets of the various cables. Some of these are very fragile and as the stage gets moved about in the sample chamber, some of the wires can get torn off (Figure 21). In the case of a fracture in the T1 or T2 thermocouple, the software will show a measurement of "980 ^{o}C" and "-Inf", respectively. The solution is to solder the wire back on. Contact Harald Holm or Tor A. Nilsen for assistance regarding soldering.

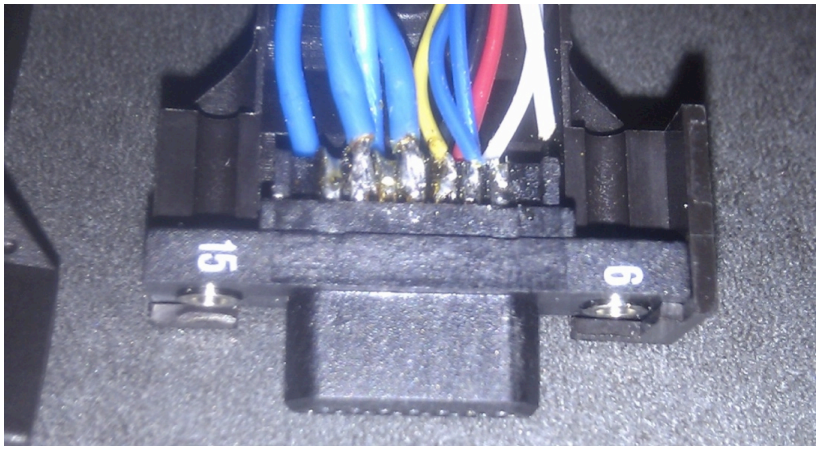

Figure 21: The blue and the white wire on the right have fractured inside a tiny fragile socket.

- A short circuit may be caused if the soldered wires come in contact with other wires or the exposed metal sockets. The effect is unknown due to absence of such events.

Appendix C

More Temperature Measurements

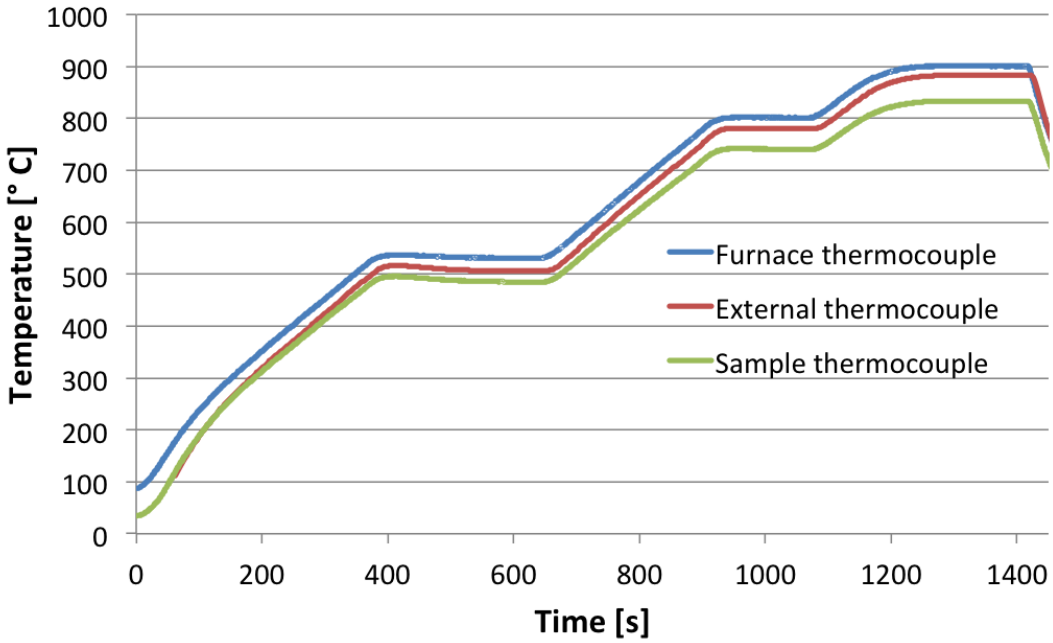

Figure C.1: A first batch sample.

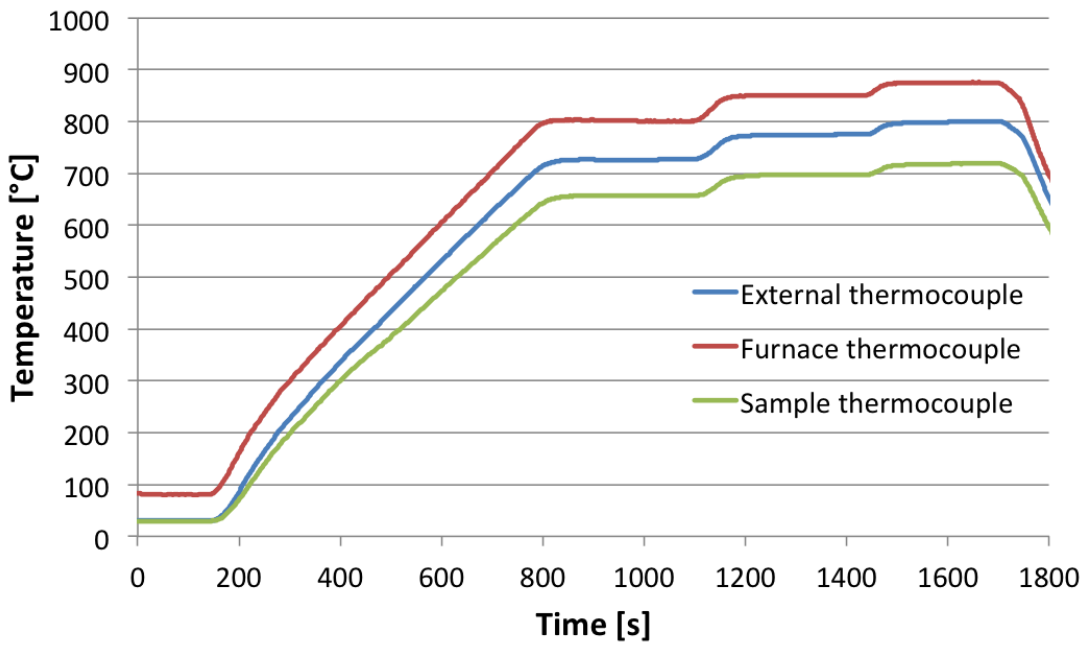

Figure C.2: A first batch sample.

Appendix D

More in situ H/Q experiments

Table D.1: Fraction of points assumed to be incorrect indexed (CI<0.05) and fraction austenite in the scans presented in figure D.1

Sample	*Fraction CI<0.05*	*Fraction austenite*
Before heating	0.039	0.003
Heated sample	0.072	0.026
After quenching	0.306	0.027

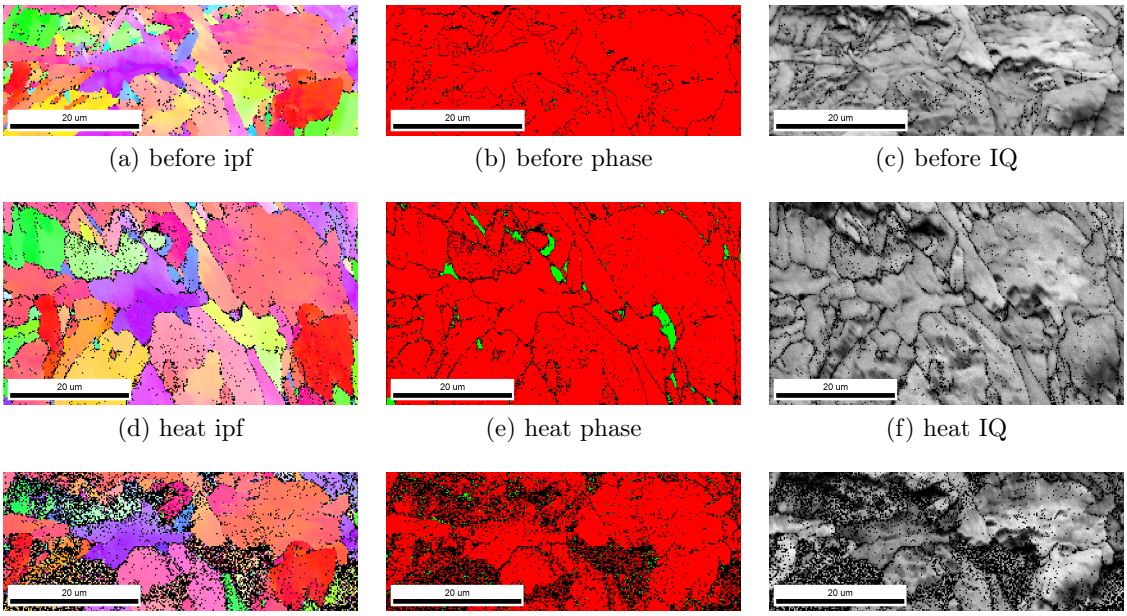

(a) before ipf (b) before phase (c) before IQ

(d) heat ipf (e) heat phase (f) heat IQ

(g) after ipf (h) after phase (i) after IQ

Figure D.1: 26.03 in situ x70 1: T1=840°C, T2=816°C, $\Delta t_{6/4}$=6.8s.

Table D.2: Fraction of points assumed to be incorrect indexed (CI<0.05) and fraction austenite in the scans presented in figure D.2

Sample	*Fraction CI<0.05*	*Fraction austenite*
Before heating	0.029	0.004
Heated sample	0.025	0.013
After quenching	0.579	0.496

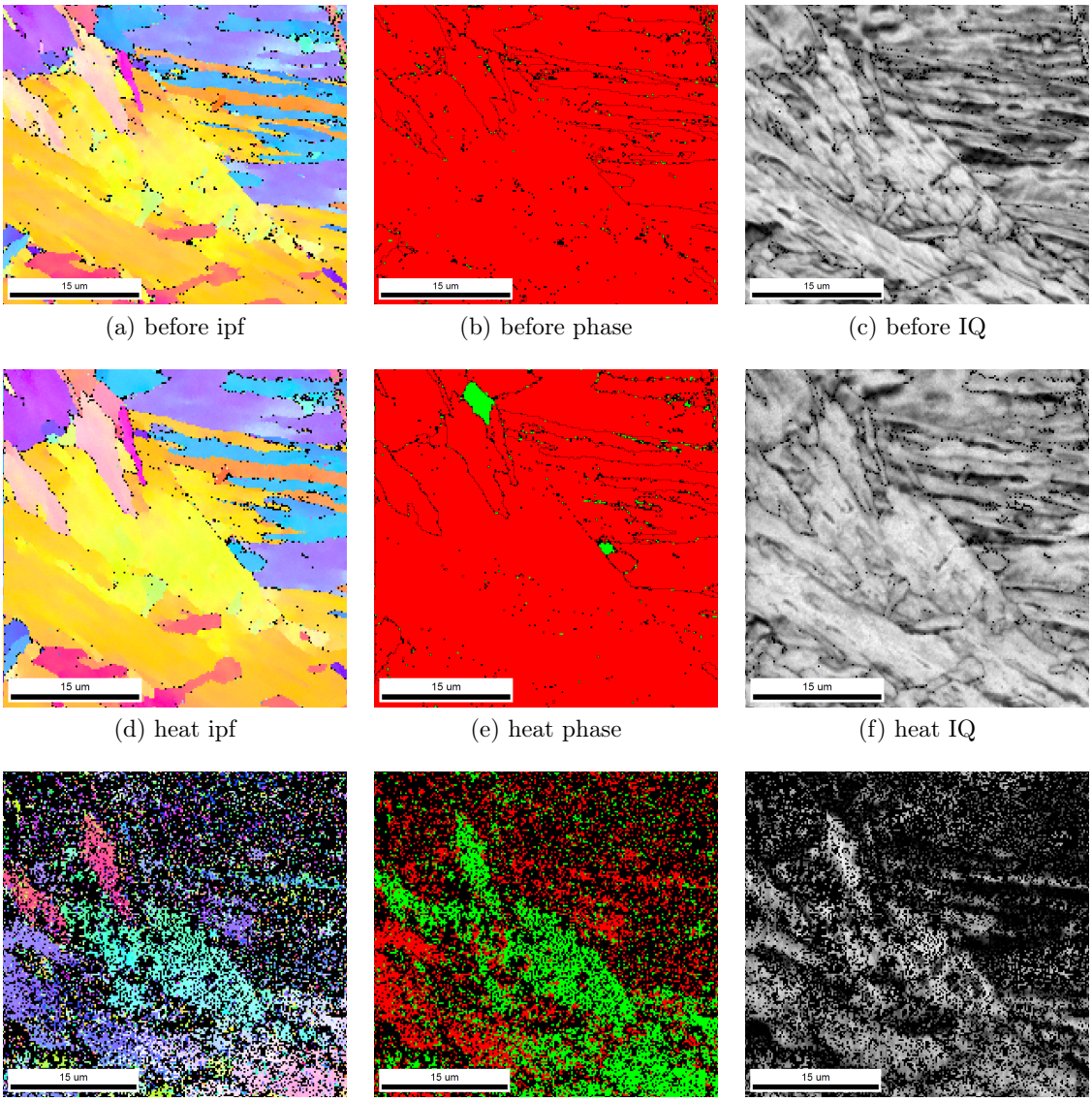

(a) before ipf (b) before phase (c) before IQ

(d) heat ipf (e) heat phase (f) heat IQ

(g) after ipf (h) after phase (i) after IQ

Figure D.2: 25.03 in situ x70 1: T1=840°C, T2=800°C, $\Delta t_{6/4}$=6.5s.

Table D.3: Fraction of points assumed to be incorrect indexed (CI<0.05) and fraction austenite in the scans presented in figure D.3.

Sample	*Fraction CI<0.05*	*Fraction austenite*
Before heating	0.022	0.004
Heated sample	0.035	0.008
After quenching	0.011	0.003

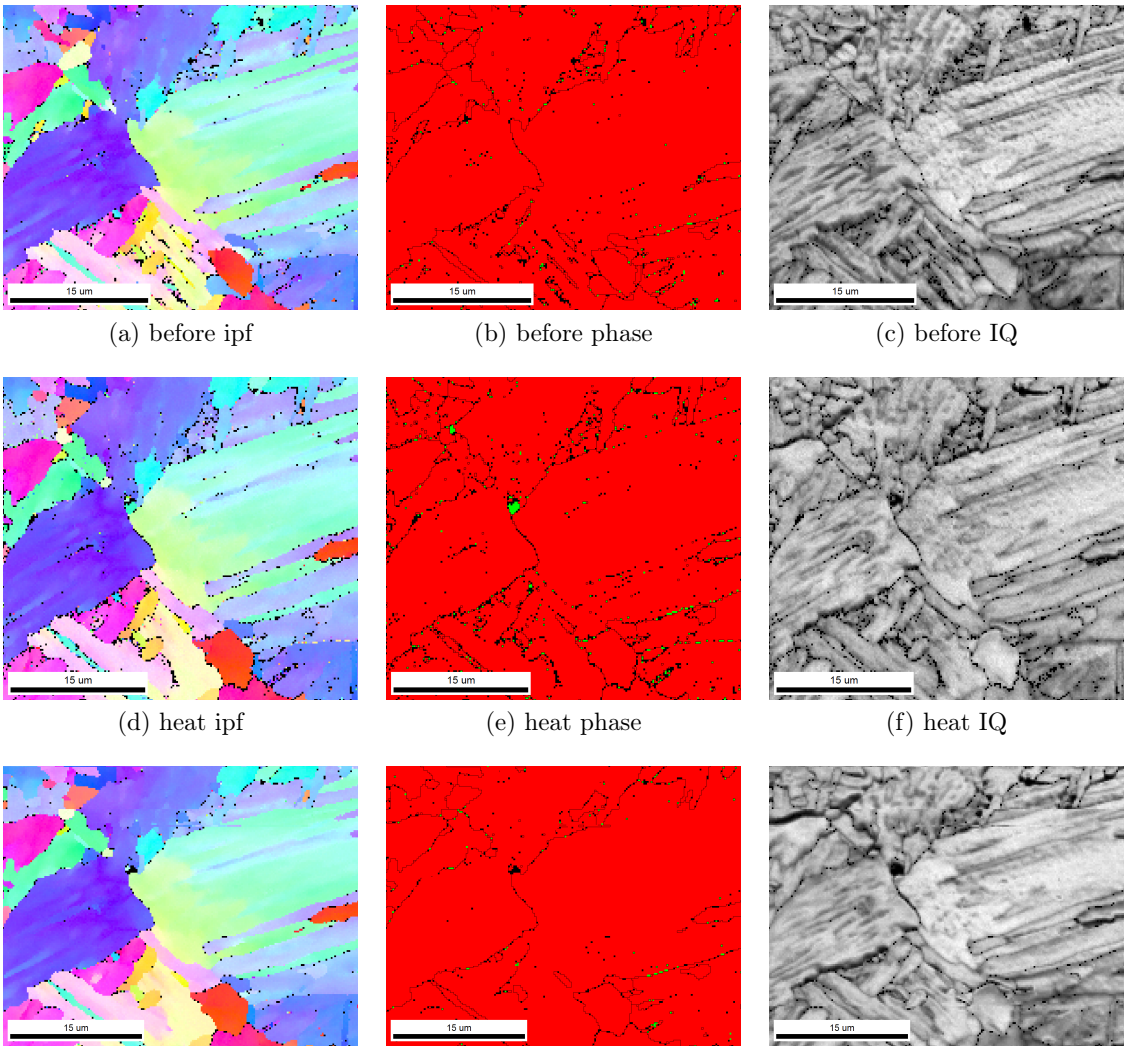

(a) before ipf (b) before phase (c) before IQ

(d) heat ipf (e) heat phase (f) heat IQ

(g) after ipf (h) after phase (i) after IQ

Figure D.3: 18.05 in situ x70 1: T1=840°C, T2=784°C, $\Delta t_{6/4}$=5.9s.

Table D.4: Fraction of points assumed to be incorrect indexed (CI<0.05) and fraction austenite in the scans presented in figure D.4

Sample	*Fraction CI<0.05*	*Fraction austenite*
Before heating	0.032	0.004
Heated sample	0.034	0.009
After quenching	0.007	0.002

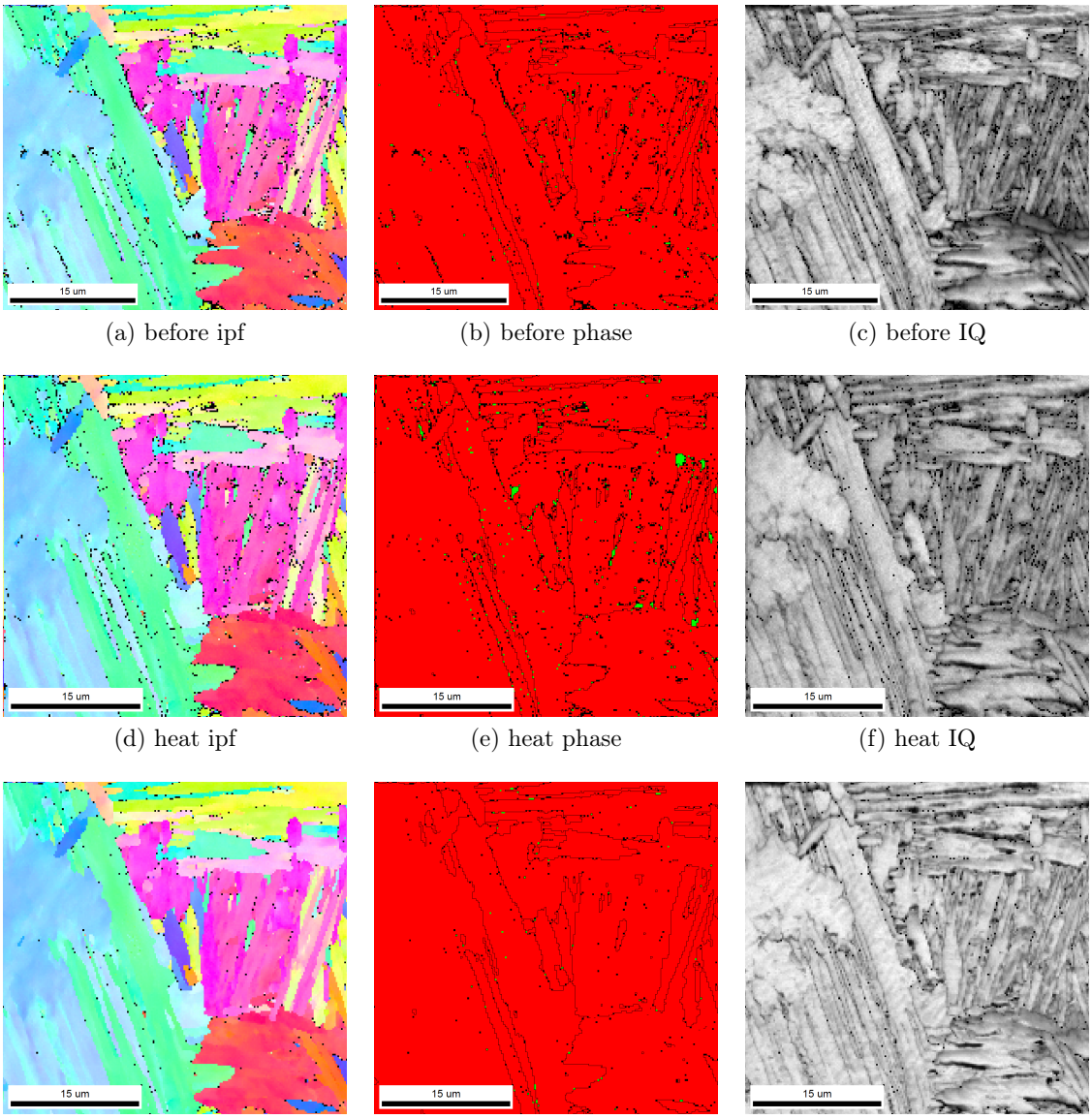

(a) before ipf (b) before phase (c) before IQ

(d) heat ipf (e) heat phase (f) heat IQ

(g) after ipf (h) after phase (i) after IQ

Figure D.4: 18.05 in situ x70 2: T1=850°C, T2=740°C, $\Delta t_{6/4}$=5.4s.

Table D.5: Fraction of points assumed to be incorrect indexed (CI<0.05) and fraction austenite in the scans presented in figure D.5

Sample	*Fraction CI<0.05*	*Fraction austenite*
Before heating	0.016	0.005
Heated sample	0.028	0.006
After quenching	0.011	0.002

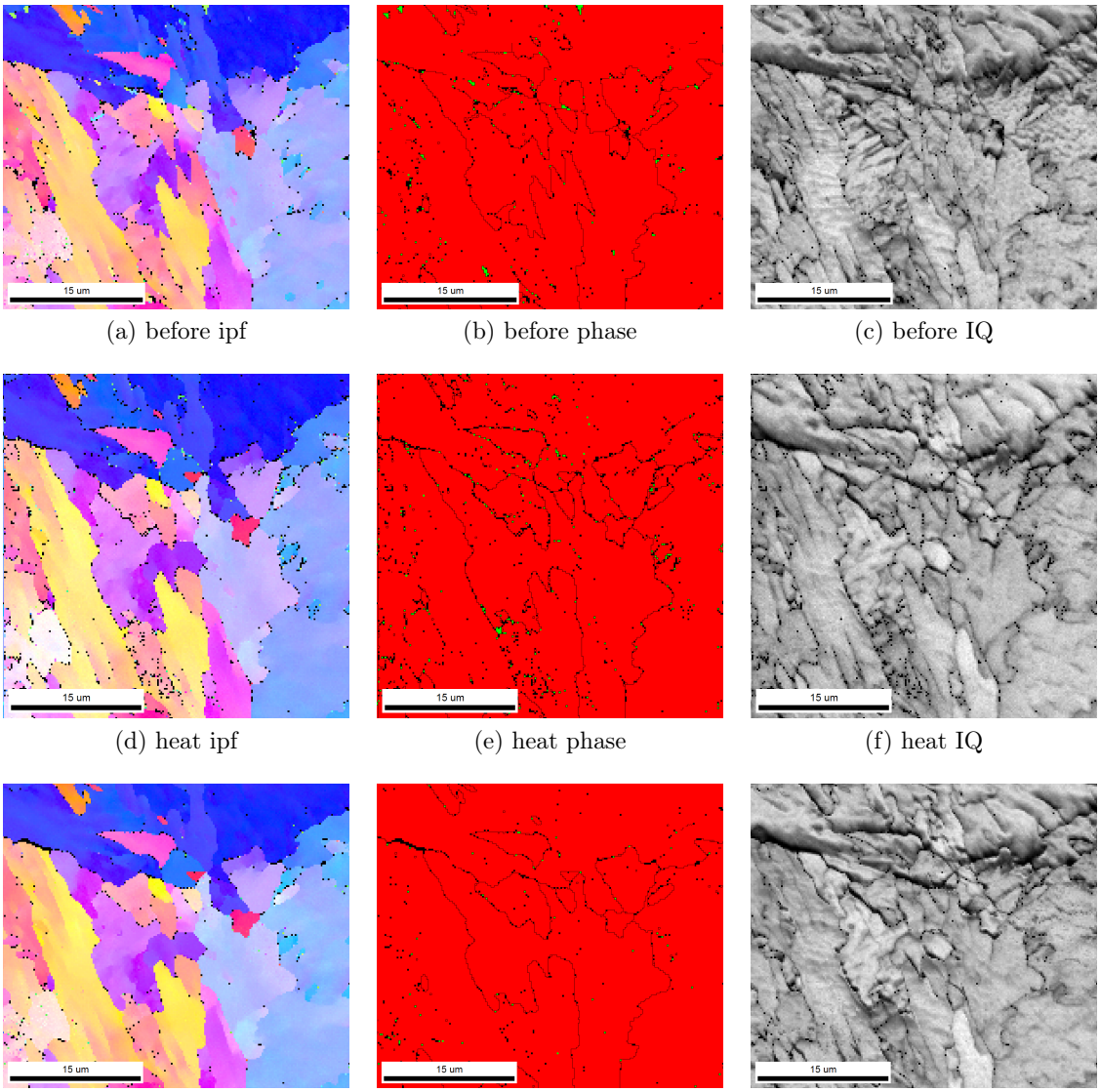

(a) before ipf (b) before phase (c) before IQ

(d) heat ipf (e) heat phase (f) heat IQ

(g) after ipf (h) after phase (i) after IQ

Figure D.5: 18.05 in situ x70 3: T1=855°C, T2=800°C, $\Delta t_{6/4}$=5.4s.

Table D.6: Fraction of points assumed to be incorrect indexed (CI<0.05) and fraction austenite in the scans presented in figure D.6

Sample	*Fraction CI<0.05*	*Fraction austenite*
Before heating	0.032	0.003
Heated sample	0.046	0.009
After quenching	0.499	0.438

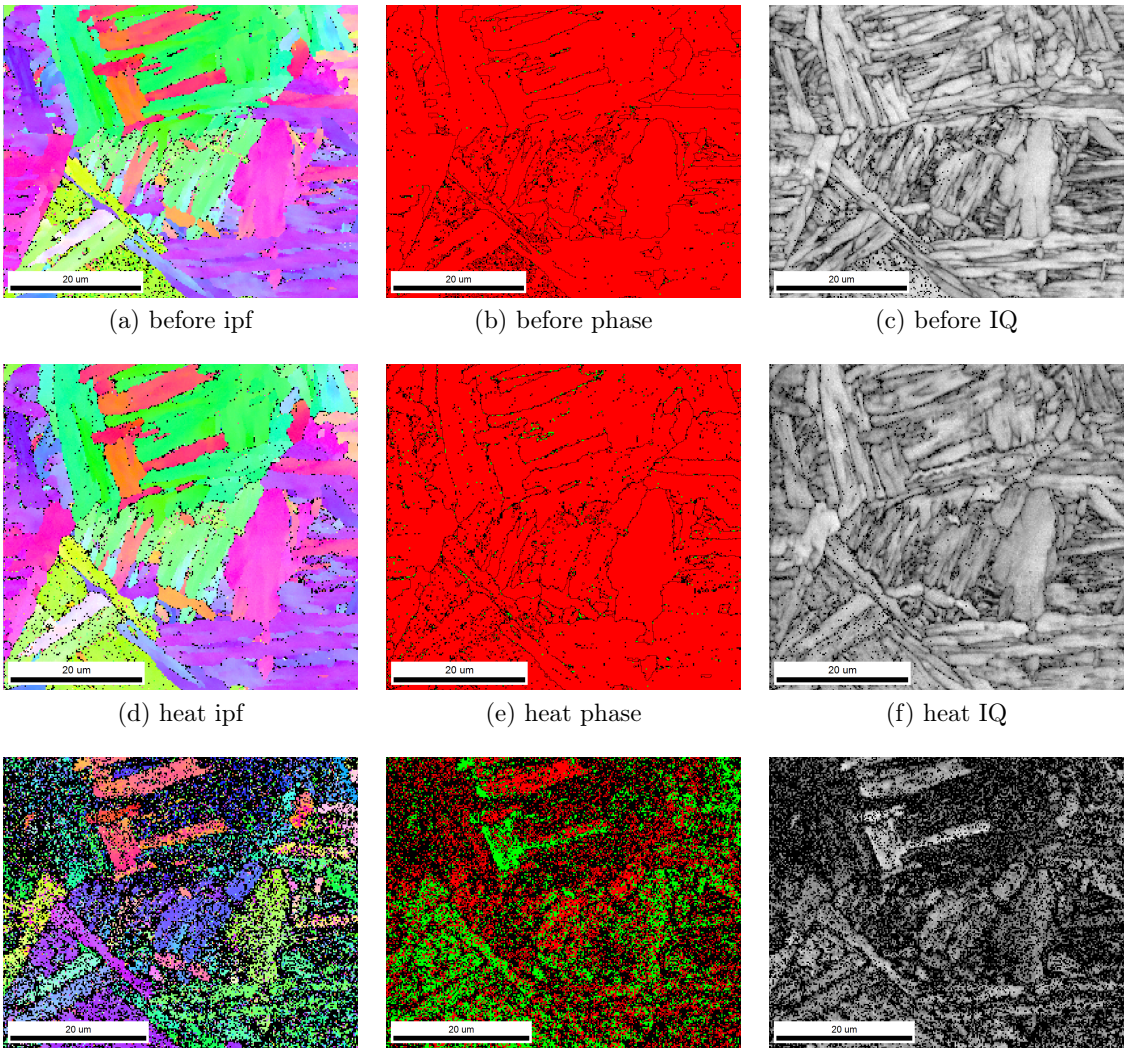

(a) before ipf (b) before phase (c) before IQ

(d) heat ipf (e) heat phase (f) heat IQ

(g) after ipf (h) after phase (i) after IQ

Figure D.6: 23.05 in situ x70 1: T1=890°C, T2=803°C, $\Delta t_{6/4}$=5.7s.